UNIVERSITY OF CALIFORNIA, SAN DIEGO

Development of a Large Format Direct Detection Device for Three Dimensional Transmission Electron Microscopy

A dissertation submitted in partial satisfaction of the
requirements for the degree
Doctor of Philosophy

in

Chemistry

by

Anna-Clare Milazzo

Committee in charge:

Professor Xuong Nguyen-Huu, Chair
Professor Mark Ellisman
Professor Gourisankar Ghosh
Professor Elizabeth Komives
Professor Andrew Kummel

2009

The dissertation of Anna-Clare Milazzo is approved, and it is acceptable in quality and form for publication on microfilm and electronically:

_____

_____

_____

_____

_____
Chair

University of California, San Diego

2009

DEDICATION

To Viera Ivanovna Korenczuk Pablant, Ph. D.,
peace and friendship be with you.

TABLE OF CONTENTS

LIST OF FIGURES

ACKNOWLEDGEMENTS

I would like to first and foremost thank Professor Nguyen-Huu Xuong, my thesis advisor, whose guidance and support led to the completion of this work. It is a great honor to be his student.

The support and advice of Professors Elizabeth Komives and Susan Taylor were crucial to the completion of this thesis work. I cannot thank them enough for their help and encouragement.

Professor Mark Ellisman gave an enormous amount of helpful advice on this work as well as providing both NCMIR microscopes and personnel for this project.

Dr. Jason Lanman has been the ideal collaborator. The biological imaging studies have been successful due to his work on specimen preparation and aid in acquiring the tomography and 2D imaging data sets.

Dr. Grigore Moldovan has been tremendously helpful with deepening my understanding of solid state detectors and of the MTF, NPS and DQE characterization data analysis.

Fred Duttweiler, Ron Quillin, Philippe LeBlanc, Dr. James Bouwer, and Dr. Liang Jin have been part of the core team working on the development of the DDD prototypes. The large format DDD camera system would not have been built without their creativity, advice, design and technical assistance.

Masako Teruda processed the tilt series into tomograms. Her work ethic, cheerfulness and skill at producing fine tomographic reconstructions is unsurpassed. I would like to thank Mason Mackey and John Crum from the NCMIR who provided training and technical support for the electron microscopes. I would like to thank Tomas Molina for all the insightful discussions about the DDD.

The cryo-EM data of flock house virus used to compare to the DDD results were collected by Dr. Reza Khayat at The Scripps Research Institute. His generosity in sharing the reconstruction data is greatly appreciated.

My friends and family have continuously offered support through this journey. David Collins and Marguerite Cass have been the truest of friends. I am infinitely grateful to Novimir Pablant.

Chapter 3, in part, has been submitted for publication of the material may appear in Physical Review Letters, 2009. Milazzo, Anna-Clare; Moldovan, Grigore; Lanman, Jason; Jin, Liang; Bouwer, James C.; Klienfelder, Stuart; Peltier, Steven T.; Ellisman, Mark H.; Kirkland, Angus I.; Xuong, Nguyen-Huu. American Physical Society Journals, 2009. The dissertation author was the primary investigator and author of this paper.

VITA

2000	B. A. in Physics *honors* and Mathematics, University of Chicago
2005-2006	Graduate Teaching Assistant, University of California, San Diego
2006-2009	Graduate Research Assistant, University of California, San Diego
2005	M. S. in Physics, University of California, San Diego
2009	Ph. D. in Chemistry, University of California, San Diego

PUBLICATIONS

L. Jin, **A.C. Milazzo**, S. Kleinfelder, S. Li, P. Leblanc, F. Duttweiler, J.C. Bouwer, S.T. Peltier, M.H. Ellisman, and N.H. Xuong. Applications of direct detection device in transmission electron microscopy. *Journal of Structural Biology*, 161(3):352–358, 2008.

L. Jin, **A.C. Milazzo**, S. Kleinfelder, S. Li, P. Leblanc, F. Duttweiler, J.C. Bouwer, S.T. Peltier, M. Ellisman, and N.H. Xuong. The intermediate size direct detection detector for electron microscopy. In *Proceedings of SPIE*, volume 6501, page 65010A. SPIE, 2007.

N.H. Xuong, L. Jin, S. Kleinfelder, S. Li, P. Leblanc, F. Duttweiler, J.C. Bouwer, S.T. Peltier, **A.C. Milazzo**, and M. Ellisman. Future Directions for Camera Systems in Electron Microscopy. *Cellular Electron Microscopy*, page 721, 2007.

A.C. Milazzo, P. Leblanc, F. Duttweiler, L. Jin, J.C. Bouwer, S. Peltier, M. Ellisman, F. Bieser, H.S. Matis, H. Wieman, et al. Active pixel sensor array as a detector for electron microscopy. *Ultramicroscopy*, 104(2):152–159, 2005.

N.H. Xuong, **A.C. Milazzo**, P. LeBlanc, F. Duttweiler, J. Bouwer, S. Peltier, M. Ellisman, P. Denes, F. Bieser, H.S. Matis, et al. First use of a high- sensitivity active pixel sensor array as a detector for electron microscopy. In *Proceedings of SPIE*, volume 5301, page 242. SPIE, 2004.

A.C. Milazzo, S.E. Thonnard, C. Lam., Analysis of the SSULI (Special Sensor Ultraviolet Limb Imager) Stacked-Grid Mechanical Collimator, In *Proceedings of SPIE*, volume 3443, 1998.

ABSTRACT OF THE DISSERTATION

Development of a Large Format Direct Detection Device for Three Dimensional Transmission Electron Microscopy

by

Anna-Clare Milazzo
Doctor of Philosophy in Chemistry

University of California San Diego, 2009

Professor Xuong Nguyen-Huu, Chair

New imaging systems are crucial in improving transmission electron microscopy (TEM) for the investigation of the structure and function of biological systems from the molecular to the cellular scale. Presented in this dissertation is the characterization of a direct detection device (DDD) camera. Also presented is an exploration of some of the TEM imaging applications of this camera. The DDD is a monolithic active pixel sensor that directly records the energy deposited by an incident electron. The camera that will be discussed is, to date, the largest prototype developed by the Xuong group at UCSD, with a 1024×1024 pixel array format. Unique features of the DDD are presented that allow for a variety of measurements and image processing not possible with the standard CCD camera systems typically used for TEM. A characterization of this detector has been performed, including the measurement of the modulation transfer function, the normalized noise power spectrum, and the detective quantum efficiency. The results of these measurements show that it is capable of high resolution, wide field imaging. Tomography and 2D imaging experiments using epoxy embedded thin sections of Drosophila cells infected with flock house virus as the test specimen were performed with a 120keV TEM. The results of tomography and 2D imaging experiments with the large format DDD provide compelling evidence that this system offers a powerful new tool for gathering meaningful information about biological

specimen.

Chapter 1

Introduction

New imaging systems are crucial in improving transmission electron microscopy (TEM) for the investigation of the structure and function of biological systems from the molecular to the cellular scale. Presented in this dissertation is the characterization of a direct detection device camera (DDD) and an exploration of some of its applications. The chip that will be discussed is, to date, the largest prototype created by the UCSD Xuong group, with a 1024×1024 pixel array format (large format DDD). A rigorous characterization of this detector has been performed, and shows that it is an excellent system for wide field TEM imaging. While many EM approaches will benefit from the implementation of the DDD, we anticipate the most significant impact will be in the field of EM tomography. Thus we have focused efforts in exploring this area. The results of the tomography and 2D imaging experiments with the large format DDD provide compelling evidence that this system is useful for gathering meaningful information about biological specimen. Unique features of the DDD are presented that have allowed for a variety of measurements and image processing not possible with the standard camera systems used for TEM.

The focus of Chapter 1 is to introduce the motivation for the development of the large format DDD. This includes an overview of TEM imaging and electron tomography. The types of camera systems currently in use in TEM are described as well as the new generation of direct detection devices. Chapter 2 covers a technical description of the large format DDD camera system and the integration

with 120keV and 200keV transmission electron microscopes. Chapter 3 presents a thorough characterization of this detector which quantitatively demonstrates the advantages of this system. In Chapter 4, the results of two dimensional imaging and tomography experiments demonstrate the practicality of using the large format DDD to image biological samples.

1.1 Description of transmission electron microscopy and tomography

1.1.1 TEM imaging introduction

In order to understand the need for a new imaging system, it is necessary to explain the basics of transmission electron microscopy. Thus, a brief description of conventional transmission electron microscopy is provided. A transmission electron microscope is a device that measures the transmission of electrons through a specimen. Figure 1.1 is a simplified schematic of a transmission electron microscope that shows only one of the three standard magnetic lenses. The top of the diagram shows the beam source, often a tungsten or LaB_6 filament, that accelerates electrons to a specific energy in a coherent parallel beam. The electrons pass through a specimen held at the object plane and are scattered by several mechanisms. The scattering, which may be elastic or inelastic, will cause either a loss of energy or a change in the direction of the electron path. The sample is kept relatively thin, typically less than 0.25μm, to minimize multiple scattering. The objective lens is an applied magnetic field that gathers the resulting electrons that have passed through the specimen. The electrons form a diffraction pattern in the back focal plane of the lens and an image of the specimen at the image plane. The diffraction pattern or image is then magnified to the desired amount by the intermediate lens system for viewing on a phosphorescent screen or imaging device [9, 61].

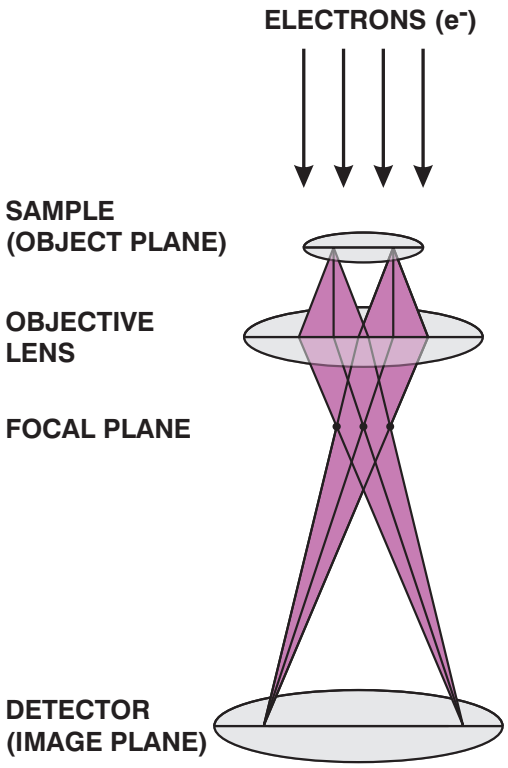

Figure 1.1: This figure shows an overview of the microscope optics in a transmission electron microscope. Electrons are emitted from a source under vacuum and are transmitted through a specimen in the object plane. They pass through a magnetic objective lens that gathers the resulting electrons that have passed through the specimen and forms a diffraction pattern in the back focal plane of the lens, and an image of the specimen in the image plane. Finally an intermediate lens (not shown) magnifies the image from the imaging plane onto a recording medium.

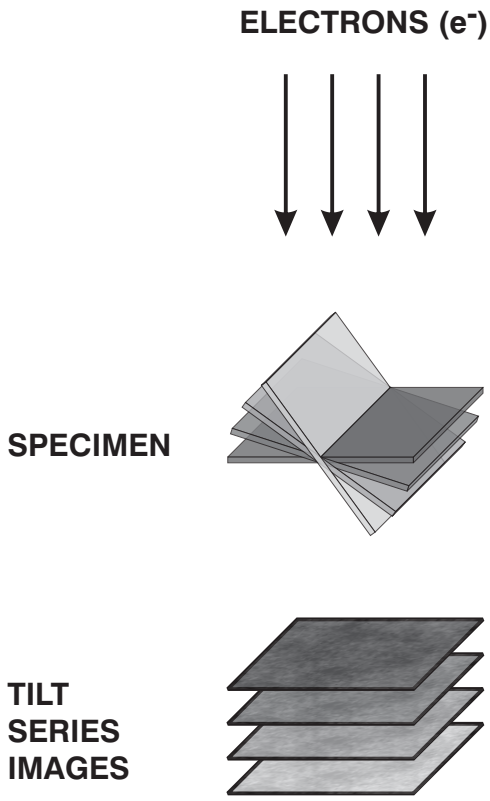

Figure 1.2: Diagram shows the basic principle of tomography. An electron beam passes through a specimen that is rotated about an axis as it is imaged. Each tilt image is the projection of the specimen from a particular angle. The projections are then recombined in software to yield a reconstruction of the original 3D specimen.

1.1.2 Introduction to tomography

In order to place many of the experimental results in context, a description of tomography and its limitations is presented. Electron tomography is a technique where a specimen is rotated about an axis parallel to the imaging plane, and images are collected at a variety of angles. These images, referred to as projections, are then analyzed to obtain an estimate of the three dimensional structure of the specimen. Figure 1.2 shows how the set of projections, also known as a tilt series, is imaged. Generally the samples and specimen stage limit the maximum projection angles to between 60° and 70°, although some high tilt specimen holders have a tilt capability exceeding 70°. In addition, projections taken at high tilt angle are often not usable due to problems with alignment, focus, and signal strength. [28].

Once a tilt series is acquired, a necessary step is an alignment of all the images. Small shifts in the image are common as the specimen is rotated because of a slight difference between the axis of rotation through the specimen and the eucentric height of the specimen. One of the most common and robust methods used to aid alignment is the deposition of colloidal gold on the surface of the specimen. Alignment is performed by tracking the locations of this gold through a tilt series [47]. Although gold works well, much interest remains in developing new image processing algorithms that would produce accurate alignment without gold or other fiducial markers [10, 12].

Once the tilt series images are aligned, these projections are further processed to generate a tomogram. The projection theorem states that the 2D Fourier transform of a projection is a slice of the 3D Fourier transform of the object imaged [70]. Therefore, if the projections of an object are sampled at enough different angles, then theoretically the full 3D Fourier transform of the object can be obtained. The Crowther criterion [17] (Equation 1.1) provides an estimate for the achievable resolution where d is defined as the size of the object in the direction of the electron beam and N is the number of equally spaced projections. However, the Crowther criterion is of limited use, since the actual features discernable in a tomogram are more likely to be constrained by noise and structural preservation [44].

$$\text{resolution} = \frac{\pi \mathrm{d}}{\mathrm{N}} \tag{1.1}$$

Many different strategies have been used to create high quality tomograms from tilt series. A commonly used technique, the back projection method, is adapted from x-ray tomography and was based upon the assumption that the measured energetic particles follow straight paths. However, this is not the case in electron tomography since, unlike x-rays, electrons follow curved paths due to the magnetic fields in the microscope. New algorithms are being developed to take this into account and improve the quality of the tomograms. TxBR, the software used for the analysis of the tilt series acquired with the DDD, is one such software package [59, 28, 44].

Missing information in Fourier space

The information in the projections determine how faithful a 3D reconstruction will be to the original object. In practice, the sample is not tilted to $\pm 90°$, but a smaller set of angles, usually $\pm 60°$, is acquired. This leaves an unsampled region in Fourier space, often called the "missing wedge" since it is wedge shaped for a single axis tilt series. This missing information often results in the objects in the reconstruction having an elongated appearance along the vertical axis in single tilt tomograms. Depending on the tilt range, the "missing wedge" can account for 33% or 22% information loss in Fourier space for a single axis tilt series using $\pm 60°$ and $\pm 70°$ tilt angles, respectively. Rotating the specimen 90° and acquiring a second tilt series reduces the "missing wedge" to a "missing pyramid", decreasing the information lost to 16% or 7% in Fourier space for $\pm 60°$ and $\pm 70°$ tilt angles [44]. Theoretically, the information lost can be reduced by collecting more tilt axes. Multiple axis tomography is covered in more detail in Chapter 4. The missing information is covered here to highlight the limitations with electron tomography and how this effect on objects in the tomogram needs to be considered when interpreting and analyzing the tomogram.

To end this brief introduction to tomography, it should be made clear that quantitative measures of information content in tomograms is a very active area of

research. Statements about resolution have limited usefulness and the discussion of results of this thesis will focus more on what relevant biological information can be gathered from the tomograms acquired with the large format DDD.

1.2 Imaging systems in transmission electron microscopy

1.2.1 Current imaging systems in TEM

Photographic emulsion film

Film is still considered the optimal means for recording high resolution images. Photographic emulsion film used for TEM is composed of silver granules suspended in a gelatin layer 10-30μm thick on a plastic holder. There are, however, significant problems with using film. These include noise from non homogeneity in the recording medium, non linearity in response, and extensive physical manipulation that includes film cartridge loading, post-exposure development and digitization [29, 75]. Furthermore, film is not well suited to certain types of TEM imaging such as tomography where immediate feedback on image quality and location is necessary for successful data acquisition [44].

Imaging plates

While not currently in widespread use, imaging plates are another type of recording device for TEM. Initially developed for x-ray radiography, imaging plates offer highly linear response, large dynamic range, and digital readout. The mechanism behind this detector is a phosphor layer that stores the energy of charged particles such as x-rays or electrons. A laser is then required to cause the imaging plate to release the stored energy as light [75]. However, a limited signal to noise ratio [76] and resolution [32] are the primary reasons these detectors have lost favor to the slow scan CCD camera.

CCD (Charge Coupled Device) camera systems

The first charge coupled device (CCD) was invented in 1970 [8] and the direct digital readout scintillator coupled CCD is now a standard detector option commonly used instead of film in TEM imaging. Research in the field of astronomy was the driving force behind the development of large format CCDs. The requirement of high-resolution images when photographic film was impractical or impossible to use led to the development of large format CCD's with pixel array sizes greater than 1k×1k. Results from the first experimental digital imaging system using CCDs for TEM were published in 1982 [60]. Since then, many other systems have been reported [2, 14, 19, 23, 24]. Complete digital imaging systems for TEM are now produced by several companies, including: Advanced Microscopy Techniques (Rowley, MA), Gatan (Pleasanton, CA), JEOL (Peabody, MA), Photometrics (Tuscon, AZ), and Tietz-Video and Image Processing (Herbststrasse, Gauting, Germany). These systems have become invaluable for applications such as microscope automation, automated electron tomography, electron holography, protein crystallography, and telemicroscopy.

CCD detectors for electron microscopy are available with formats up to 8k×8k pixels [7], although few, if any, commercial detectors deliver the full resolution of the device [24]. For electron microscopy applications a phosphorescent scintillation screen is needed to convert the electron image to a photonic image within a spectral range where the detector quantum efficiency is maximized. Unfortunately, with each electron event, the photonic bloom created within the scintillation screen is typically greater than the pixel pitch of the device. At 300keV, the full-width at half- maximum (FWHM) of the spot is around 30μm; however, the full width at 1% maximum is 200μm [26]. With a CCD pixel size of 15μm×15μm, the large spot size will effectively reduce a 2048×2048 (or 4096×4096) pixel CCD to only 1024×1024 (or 2048×2048). To mitigate this problem, tapered fiber optics and/or demagnification lens optics can be used to demagnify the scintillator image to match the CCD device, thereby restoring the modulation transfer function (MTF). However, both optical relay scenarios introduce some problems. With tapered fiber optics, large spatial distortions and non-uniformities are introduced

that are difficult to correct. With demagnification lens-optics, the poor efficiency of the coupling dramatically reduces the number of photons reaching the CCD, which in turn reduces the signal-to-noise ratio of the system and necessitates the use of costly +70% efficiency (back-thinned; back-side illuminated) CCD devices [25].

1.2.2 Development of new direct detector camera systems

To further push advances in structural and cell biology, it is necessary to combine fast, digital image acquisition with a system that produces images with the high quality obtainable with film. Direct electron detectors are expected to fulfill this role in microscopy. There are three main types of direct detection sensors being developed for imaging in TEM. The features of monolithic active pixel sensors, hybrid pixel detectors, and double sided strip detectors are described in this section. These are solid state detectors that use silicon to detect charged particles. Compared with CCD cameras, these detectors have fast readout and high sensitivity, the are radiation tolerant and, most importantly, do not require the use of a scintillator.

The DDD is an example of a monolithic active pixel sensor (MAPS) that has the readout electronics and sensor integrated into one monolithic design [27]. Section 2.1.1 covers in greater detail the design and charged particle detection of the DDD, a MAPS type detector. Recently work from Lawrence Berkeley National Laboratory has been published with prototype MAPS sensors of 10μm and 20μm pixel size and 24×48 pixel detection area. This prototype has an imaging area that is too small to perform imaging beyond basic characterization measurements [4]. A different prototype has been developed at Brookhaven National Laboratory. This prototype, the MIMOSA-V chip, has 17μm pixel pitch, a 1 megapixel format, and a 20μm epitaxial layer making it large enough for TEM imaging experiments [21]. The published results from testing these other MAPS prototypes show that these sensors have generally similar characteristics to the DDD.

Hybrid pixel detectors (HPD) have readout electronics separate from the pixel sensor that are connected through bump bonding [27]. The main drawback

to these detectors is that the pixel size must remain large because of the difficulty of bump bonding. For example, the Medipix2 detector has pixels with an area of $55\mu m^2$ with dimensions of 512×512 pixels. Despite the large pixel size and smaller field of view, biological imaging studies at 120keV are being carried out with this detector [50]. HPDs do produce an imaging system capable of low noise and high resolution due to the ease of using an electron counting method instead of charge integration [21].

In the early stages of development are double-sided strip detectors that use electron counting instead of charge integration as the method for imaging [55, 56]. Not enough results have been published with these detectors to make a comparison to the other direct electron detectors.

In summary, the large format DDD has a unique combination of features compared to other direct detection imaging prototypes. The large format DDD has a small pixel size of 5μm, a 1024×1024 pixel array, a very thin electron sensitive region to reduce charge spread and the MAPS design. The biological imaging studies presented in Chapter 4 were possible due to these features.

1.3 Development of the large format DDD

1.3.1 Historical background of work with earlier prototypes of DDD

Standard CMOS chips do not work well for charged particle detection. However, the addition of a thin sensitive epitaxial layer of silicon radically changes the sensing properties of the chip. This development in CMOS technology paved the way for the creation of the DDD [36, 22, 53, 71].

The Xuong group tested three DDD prototypes previous to the development of the large format (1024×1024 pixel array) DDD and has published results from two of them [54, 33, 34, 73, 74]. A good deal of success was achieved with testing the medium format (512×512 pixel array) DDD for TEM imaging [34]. However due to the limited imaging area, investigations using biological specimen were ex-

tremely difficult. The large format DDD was created for the purpose of performing investigations of biological macromolecules with its much wider imaging area. An additional goal for this prototype was the implementation of full automation with the device for tomography and montage imaging. Automation will eventually result in the ability to perform high resolution imaging with the large format DDD by any researcher at the NCMIR (the National Center for Microscopy and Imaging Research), a P41 technology development center supported by the National Center for Research Resources of the National Institutes of Health.

1.3.2 Unique features of the large format DDD

Higher sensitivity, smaller pixel size, and faster readout are the most important features of the large format DDD. How these features contribute to an improved imaging system is described in detail here. These features are mentioned several times throughout the discussion of the experiments with this system and this section attempts to relate these features to their role in making the large format DDD a useful camera system for TEM.

The combination of the small pixel size, of 5μm, and the higher sensitivity of the DDD allow for imaging at much lower magnifications than required with CCD cameras. CCD cameras typically have pixels sizes at least 3 times as large and are 3 times less sensitive. Lower magnification is desired when performing TEM, especially for high resolution work, because microscopes are often unstable at high magnifications. Furthermore, higher magnification requires a higher beam flux and thus higher dose to the specimen.

The higher sensitivity of the DDD at any magnification results in less radiation to the specimen because fewer electrons need to be collected. This feature also enables successful imaging with a lower level of stain than normally required to see features of interest. Less stain theoretically should result in a general reduction in staining artifacts, though this assertion needs to be tested more extensively through future experiments with the DDD. The higher sensitivity of the DDD is expected to improve the quality of images from other biological samples with low contrast, such as antibody labeled or photo-converted specimen. For cryo-EM and

cryo-tomography, higher sensitivity allows for details in a specimen to be visible closer to true focus, which would improve the 3D resolution achievable with these techniques.

The large format, 1024×1024 pixel array, of this sensor allows for much wider field imaging than possible with earlier prototypes. Even wider fields of view can be obtained by creating large montage images with the large format DDD. In fact, the small pixel size provides a distinct advantage for montage image acquisition. With the small pixel size of 5μm, a 1024×1024 pixel array yields an imaging area of 5mm×5mm. This imaging area is a small enough area that the magnetic lenses (image shift coils) in the TEM can be used for creating precise montaged images without the need for moving the specimen. Acquisition of large montaged images with CCD cameras that have a typical imaging area of 30mm×30mm requires the use of an external specimen translation stage where precision is much more difficult to achieve.

The speed of the data readout for the large format DDD, up to 10 frames/second, is very fast compared to the CCD cameras used in TEM. The typical imaging mode for the DDD acquires multiple frames and performs a summation of them to create a final image. This type of readout is advantageous in a number of ways. Due to electrostatic charging, the specimen can drift during image acquisition, often on the order of a few angstroms per second. For high resolution imaging, this drift can severely degrade the images if long integration times are used. Drift correction has been shown to be possible with the fast readout of the DDD [34]. In addition, as discussed in further detail in Chapter 4, it is possible to perform other types of post processing with the data that are not possible with current TEM imaging systems. One such post processing technique can be used to create optimal data collection schemes to maximize information from a tilt series while minimizing dose to the specimen.

This brief introduction covered of some of the most notable features of the large format DDD. These unique features offer the potential to modify the current data collection approaches, allowing researchers to address questions that were previously impossible to approach.

Chapter 2

Technical description of the large format DDD imaging system

The large format DDD imaging system contains many components that interact in precise ways to render a well functioning camera. This chapter includes a complete depiction of the DDD sensor and support hardware. In addition, the overall DDD system operation, including software control, is discussed. Finally, a brief description is given of the two transmission electron microscopes used in the experiments presented in this thesis.

2.1 DDD chip design and operation

This section describes the basic design, properties, and operation of the large format DDD used for the experiments in this thesis. The large format DDD was designed by the Advanced Digital Imaging Laboratory at UC Irvine and represented a large part of the PhD thesis work done by Dr. Shengdong Li [43] under the advisement of Dr. Stuart Kleinfelder. The original sensor design was created for high energy particle physics. It was then adapted for the lower energies of transmission electron microscopy [71].

2.1.1 Large format DDD design

CMOS active pixel sensor design

The large format DDD has 1024×1024 pixels with a pixel pitch of 5μm resulting in an imaging area of approximately 5mm×5mm. This detector is a CMOS (Complementary Metal Oxide Semiconductor) monolithic active pixel sensor. The large format DDD prototype was fabricated using a TSMC (Taiwan Semiconductor Manufacturing Company) 2.5V 0.25μm process. The fabrication was carried out at MOSIS, a low-cost prototyping and small-volume production service for VLSI circuit development [66].

Figure 2.1 shows a cross section of a typical DDD pixel. The chip is divided into three vertical regions in the diagram. There is approximately 10μm of electronics on the top. Below the electronics is the lightly doped, 8μm thick, silicon epitaxial region. Approximately 300μm of a silicon substrate is below the sensitive epitaxial layer. A 2.5μm×2.5μm photodiode is at the center of the pixel to collect charge.

Figure 2.2 illustrates the pixel circuit diagram for the large format DDD chip. The pixel consists of the photodiode (the charge sensitive element), a reset transistor, a source follower buffer and a row select switch [43].

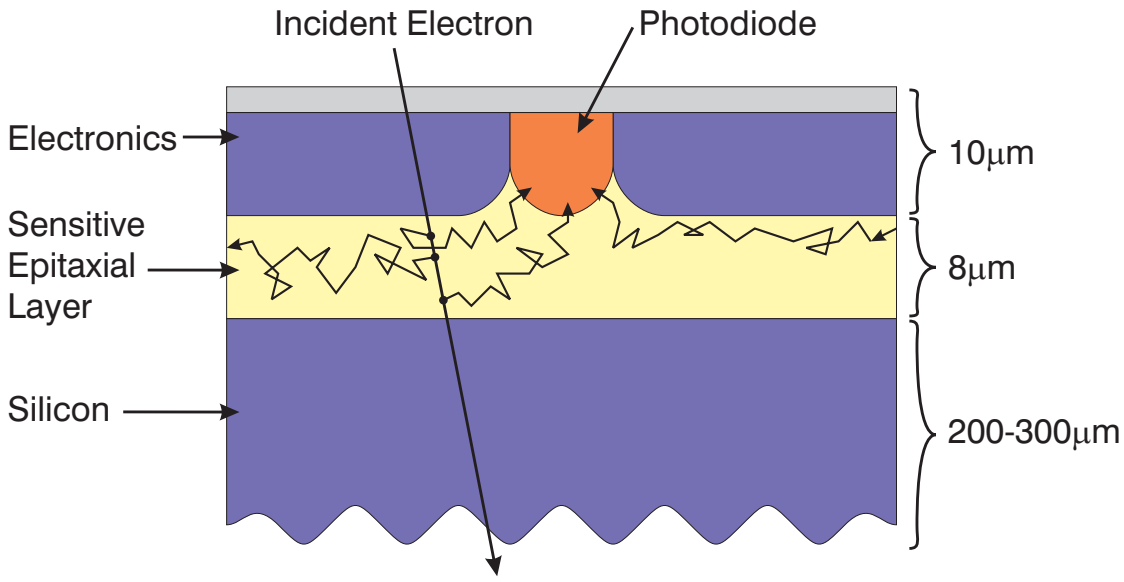

Figure 2.1: This diagram shows the cross section of a DDD pixel where the incident electron travels through the sensitive epitaxial layer and generates non primary electrons that diffuse to the photodiode in the center. Drawing is not to scale.

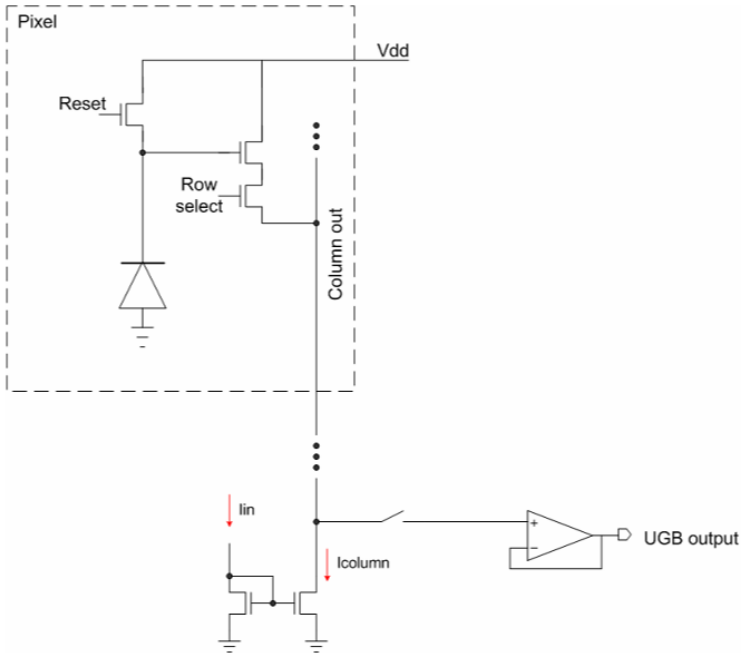

Figure 2.2: The pixel circuit diagram shows the photodiode, the reset transistor, a source follower buffer and a row select switch. Image courtesy of Dr. Stuart Kleinfelder, UC Irvine.

Electron detection with the DDD

A basic description of how electron detection occurs within the DDD is necessary to understand the images acquired with the DDD. Figure 2.1 shows the cross section of a pixel with an electron track going through the sensitive epitaxial region. As the electron passes through the sensitive epitaxial layer a succession of scattering interactions occur. The frequency of these interactions is determined from the total mean free path. These interactions can be both elastic or inelastic. This scattering process typically releases about 1000 electrons from the creation of hole-pairs. The angular deflections from elastic scattering are based on the Mott differential cross-sections [18]. To calculate the energy loss of the electrons, the inelastic electronic collision cross-sections provided by Bichsel are used [6]. Diffusion of the scattered electrons, rather than drift, is the main electron transport

mechanism [38]. The electrons are confined to the epitaxial region, and eventually diffuse to a photodiode. The thinness of the epitaxial layer reduces diffusion to adjacent pixels.

Readout design

In order to improve readout speed, the DDD pixel array is divided into 16 sectors, 64×1024 pixels each for parallel readout. The outputs are 16 unity gain buffers (UGBs), corresponding to each sector. Each UGB is then processed by an Analog to Digital Converter (ADC) on a separate electronics board.

To acquire one frame, the voltage in a pixel is read out twice before its value is reset. An integration time can be added, with a range between 0ms and 254ms. The minimum time for one read of the entire detector is 53ms, making the minimum time to acquire one frame 106ms.

The readout of the DDD, as described above, is fast compared to the CCD cameras typically used for TEM. Figure 2.3 shows how for a CCD camera signal is collected for a fixed integration time of up to several seconds and then is read out. Since the signal readout rate for a commercial TEM CCD camera is generally greater than 250ms, taking multiple fast exposures is not an option. In contrast, an image from the DDD is composed of the addition of many frames. Figure 2.3 shows an example where a final image from the DDD is composed of the sum of the five frames shown in the diagram. The benefits of the fast readout of the DDD cannot be overstated. Since there is often drift of the specimen during exposure, fast readout makes drift correction in images possible for the first time. This has been demonstrated with both the medium and large format DDD prototypes [34].

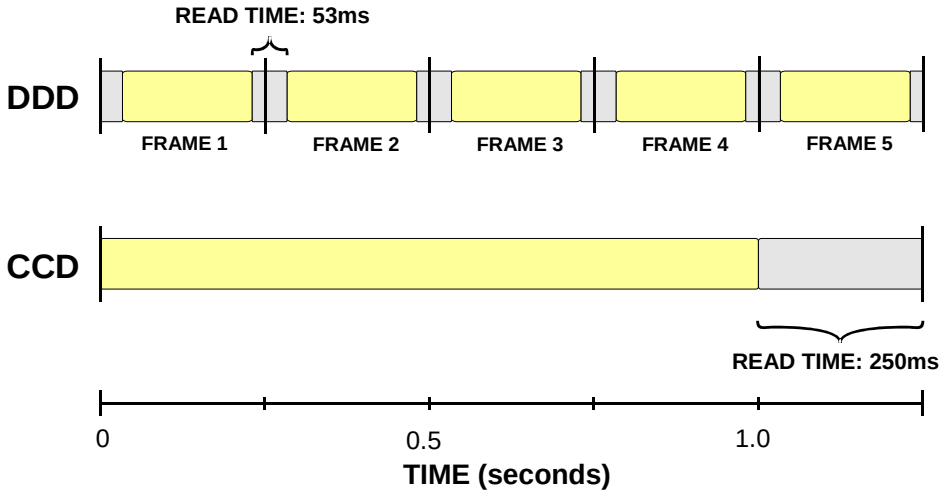

Figure 2.3: Diagram shows the difference between the way a CCD camera versus a DDD is read out. Timing is shown for a single pixel.

2.1.2 Large format DDD properties and operation

Description of noise

Here we describe the sources of noise affecting the DDD imaging system and the methods with which they are handled to produce low noise images. Because of the unique readout mode of the DDD, a much higher signal to noise can be archived compared to CCD cameras.

There are four main contributions to noise in the DDD. Three of these are intrinsic to both CCDs and DDDs and affect all pixels equally regardless of signal. The first is readout noise from the electronics. This noise is primarily from the Analog to Digital Converters (ADCs) and amplifiers, and is present only when the chip is being read out. The second contribution to the noise is the reset noise.

The signal from a pixel is measured relative to its reset level and the thermal noise associated with this reset level is referred to as the reset or kT/C noise [37]. The third source of noise is from dark current, a thermally dependent parameter. Dark noise is due to thermally generated electrons diffusing to the diode in the absence of photons or other incident particles bombarding the detector [30].

The last form of noise, that will be discussed in later sections, is Poisson noise. This is the statistical variation that occurs as a function of the number of particles that are being detected. This noise affects all particle detection systems, including CCD cameras and film, and is not uniquely inherent to the DDD camera. The error or standard deviation is$\sqrt{N}$ where N is the number of particles detected.

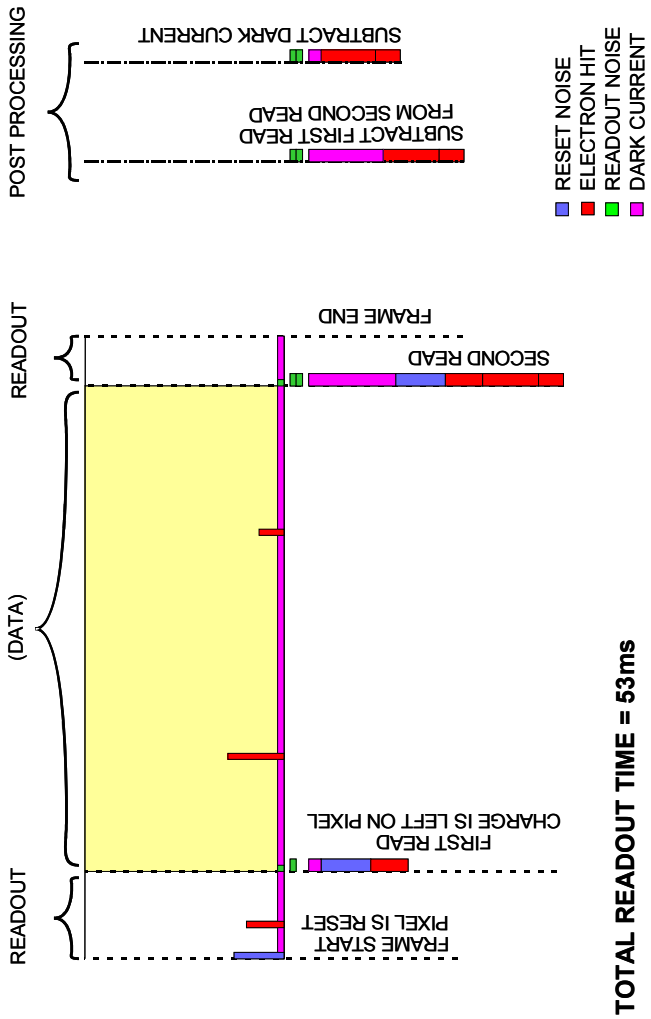

Figure 2.4: The various types of noise affecting the DDD and their temporal relationship during readout of a pixel. Post processing of dark current subtraction and correlated double sampling eliminate much of the noise from the final image.

The three dominant types of noise are shown in Figure 2.4, a diagram that represents one pixel during one frame of data acquisition. The readout noise from the electronics adds contributions twice, each time the pixel is read out. The dark noise is integrated during the time between the two sequential reads of the pixel. The reset noise occurs at the beginning when the pixel is reset. In order to effectively eliminate reset noise, correlated double sampling is applied. This consists of reading a pixel twice before resetting, storing both pixel values, and subtracting the two reads to get a final frame that has noise primarily due to dark current and readout noise. While this corrects for the reset noise, resulting in a quieter system, the correlated double sampling method limits the speed at which data may be acquired with the DDD. Furthermore, as Figure 2.4 shows, any signal generated by an incident particle in the time between the reset pulse and the first read is subtracted out of the final signal after correlated double sampling is applied.

In addition to adding noise, the dark current also adds an offset to every pixel, the level of which is dependent both on the integration time and the temperature. To remove this offset an average of many frames taken without incident particles is subtracted from the image frame. This process is described in more detail in Section 3.1.1.

Radiation tolerance

Radiation tolerance was of great importance in the design of the detector since it is one of the main hindrances to building a direct detection sensor for TEM. The earliest work in 1982 [60] exposed a CCD camera directly to electrons and resulted in rapid deterioration of the camera. An indirect scheme for CCD cameras with a scintillation screen was later adopted [24].

To use the phrase "radiation damage" when discussing radiation effects on the CMOS active pixel sensors is somewhat misleading since damage implies a state where the functionality of the chip is permanently compromised. Instead, the effects of ionizing radiation in silicon consist of trapped holes and interface states. When ionizing radiation, like electrons, strike a CMOS device, electron hole

pairs are created in the SiO_2 that either then recombine or diffuse apart. Some percentage of the electrons/holes may end up trapped as isolated charge. The effect on the performance of the detector is that dark current increases. Along with hole traps, ionizing radiation can also cause interface states to occur at the Si-SiO_2 junction. This interface state is generally a surface Si atom that has an incomplete bond in the direction of the oxide, but is bonded to three other Si atoms. A charged interface state will also lead to an increase in dark current. However, the trapped charge caused by ionizing radiation is not "damage" per se because annealing the chip will free the charge from the isolated hole traps. The interface states are more stable than isolated trapped charges and while annealing can still be used reduce these, a much longer time is required [13].

The large format DDD was made of a reasonably thin oxide to reduce the effects of ionizing radiation. This does not reduce the formation of electron hole pairs but instead the number of charges that remain trapped either at the Si-SiO_2 interface or within the oxide itself [13]. This process, combined with the ability to reverse the ionizing radiation effect by periodic annealing resulted in a camera that can withstand the radiation in a transmission electron microscope.

Figure 2.5 shows the results from radiation tolerance measurements with the medium format (512×512 pixel) DDD. The effects on the dark current are much more pronounced at the higher temperature of 33°C, but both curves show a similar exponential shape though not the same magnitude, in the dose response curves. From these studies it was shown that when cooled to -15°C the DDD can tolerate a dose of approximately 3×10^6 electrons/pixel before the dark current begins to exponentially increase. After the radiation effects became apparent, annealing the sensor at 100°C for 7 days reversed the effects of radiation to pre radiation levels with the medium format DDD prototype.

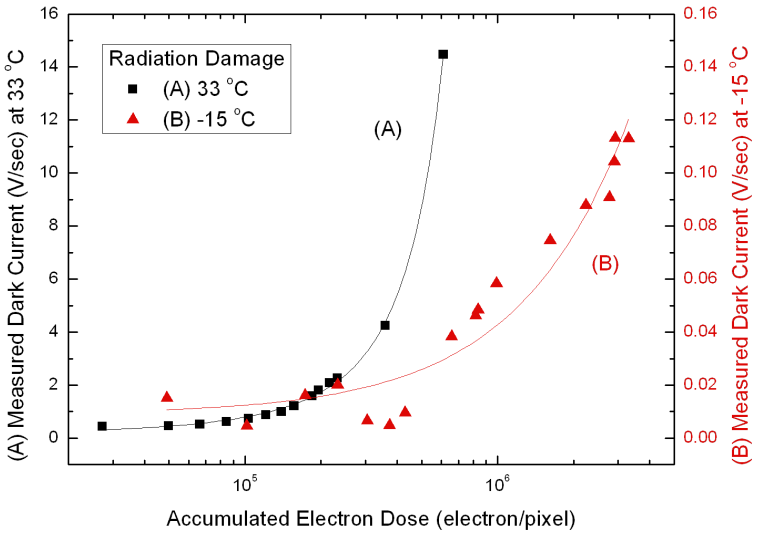

Figure 2.5: DDD radiation tolerance for medium format (512×512 pixel) chip. Axis on left shows the resulting scale for a non cooled chip while the axis on the right show shows the much lower dark current for the cooled chip as well as an increase in the time it takes for the radiation damage to become apparent. Figure courtesy of Dr. Liang Jin, UCSD [73]

2.2 DDD imaging system components

2.2.1 Support hardware

The support hardware for the DDD is described below. Particular attention is given to the novel custom hardware, such as the electron beam flux sensor.

Miscellaneous support hardware

An external hardware control box was created to allow for manual shutter control, monitoring of the thermistors and cooling system control. Also a hardware controller device was attached to the control box allowing a computer to control and monitor the values of the support hardware. Three thermistors were used to monitor the temperature of the system. These were attached to a peltier device, a metal cold finger and the back of the DDD chip. A mechanical shutter was devised to minimize unintentional radiation exposure to the sensor.

Cooling system

A cooling system is required to reduce dark current noise and minimize the effect of radiation damage to the DDD sensor. The experimental results from implementing cooling is described in Section 3.1.1. A two stage system was used which consisted of a water chiller and a peltier device. Foam blocks were placed underneath the chiller for all imaging experiments at 120keV to reduce vibrations to the camera system. The peltier device was attached to the outside of the front panel of the detector mounting assembly. A copper cold finger that ran the length of the DDD electronics board was in thermal contact with the peltier device. The cold finger was wrapped in aluminized mylar to prevent heat loss. The cold finger was attached to the bottom of the detector housing with thermal grease.

Electron beam flux sensor

A measurement of the electron beam dose to the sensor is important for the operation of the DDD system. The electron dose is necessary for calibrations and performance measurements, as well as for monitoring radiation damage. A sensor was designed specifically for the DDD system and shall be referred to as the Faraday plate in the rest of the thesis. Figure 2.6 shows the schematic for the Faraday plate. A electrometer grade op amp is attached to a circular aluminum plate that is placed adjacent to the sensor on the aluminum housing. An error of approximately 10% is expected due to the scattering of electrons from the plate.

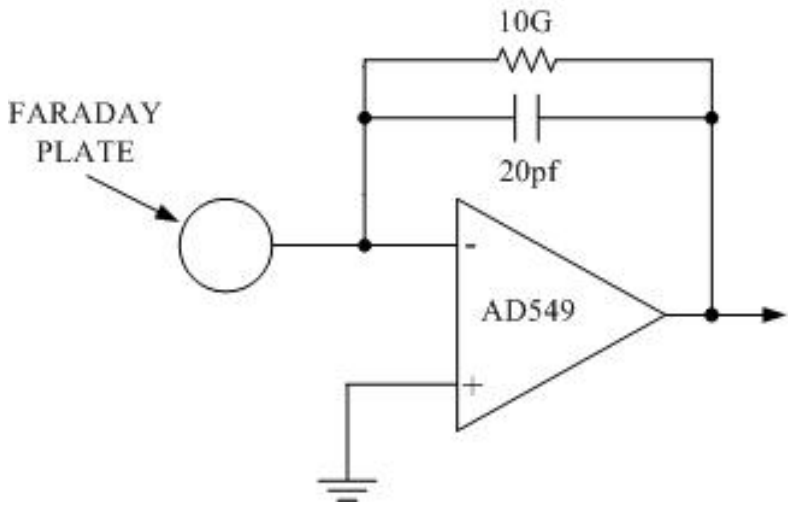

Figure 2.6: Faraday plate circuit

2.2.2 DDD computer control and software

Described in this section is the computer control of the DDD system.

Sensor control, data readout and storage

Custom firmware and readout electronics were manufactured by High Tech Electronics, Inc. The custom electronics served as the conduit between the computer, the data recording device and the sensor chip.

Due to the large amount of data generated from the large format DDD, data readout was a major problem that had to be solved inorder to acquire data continuously. A single frame from the large format DDD is 4 MB of information. Due to the high frame rate of the DDD, the system can generate 40 MB/sec of data. Recording data continuously at this rate is not possible without a specialized system. To accomplish reading out the data at this rate, we purchased a Streamstor data recording system by Conduant Corporation [16]. The Streamstor system consists of an acquisition board directly connected to eight 250 MB hard drives. It can be controlled using the DDD control electronics, and can output data to a PC. The Streamstor is able to record data at such a high rate by directly writing the data sequentially to the hard drives.

DDD Application Protocol Interface

The master software used to control all the other components of the system is called the DDD application protocol interface (API). The DDD API was written in C++ with a modular object oriented design to increase scalability and to quickly process raw image data. C++ was chosen over other languages for its speed in data processing [68]. The API also extensively uses the Standard Template Library [57] in order to minimize memory management issues and provide robust, readable code that could be straight forwardly modified by other developers.

The graphical user interface and set of image display tools built for the DDD is based upon ROOT, an object oriented data analysis framework [11]. ROOT was chosen because of the graphical user interface features and the extensive mathematical and scientific analysis packages. Furthermore, the ROOT graphical user interface framework uses signal/slots which is an advanced object oriented communication design that eliminates callback functions allowing for more efficient event handling.

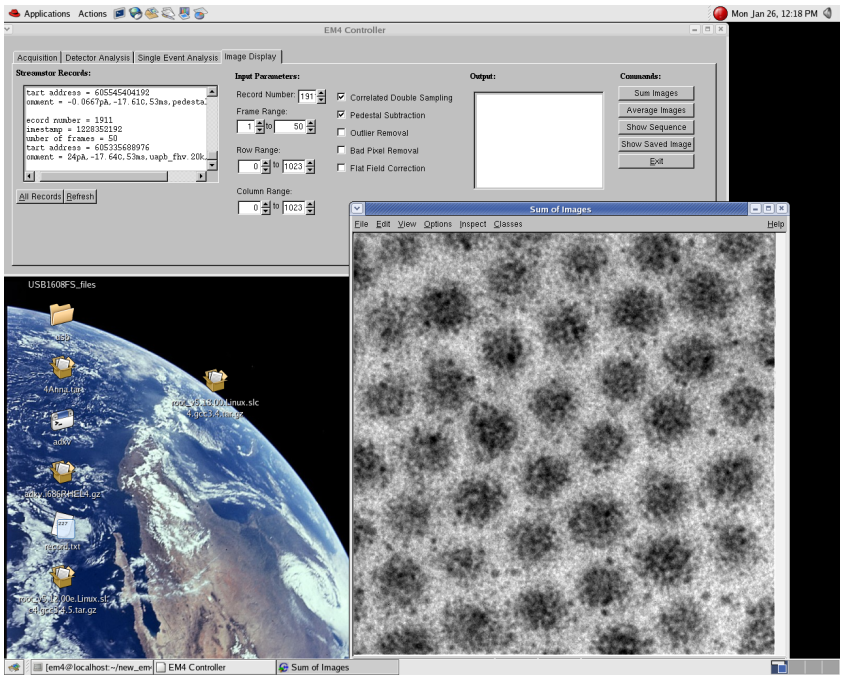

Figure 2.7: A screenshot of the graphical user interface that controls the DDD system and performs image processing and display

2.3 Experimental setup

2.3.1 DDD imaging system setup

DDD mounting schemes

Figure 2.8 shows the assembly used to mount the DDD on the JEOL TEM. This was a unique design that allowed the sensor and electronics to be mounted easily into the film drawer of any JEOL microscope. Developed for earlier DDD prototypes, this mounting system allowed the DDD to be quickly moved to other microscopes to test the performance with different incident electron energies.

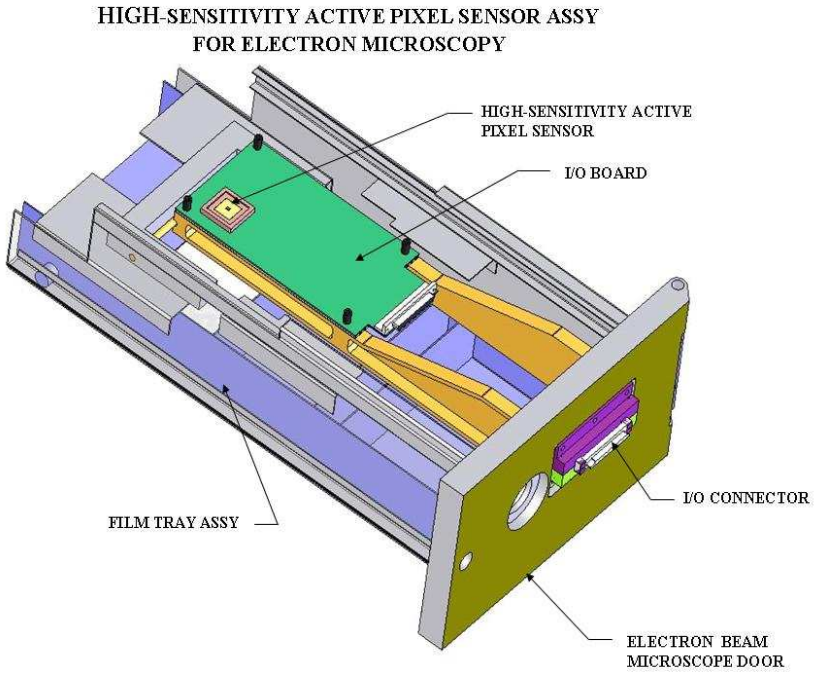

Figure 2.8: Film drawer mount for JEOL microscopes

Unlike the JEOL TEMs, the FEI brand TEMs do not have a film drawer. For the FEI TEM, a bottom mount was designed specifically for the large format DDD system. This mount allowed the DDD to be placed on axis with the microscope beam. Furthermore, ports on the side of the mount housing allowed for the

placement of other cameras adjacent to or below the DDD sensor.

Final setup

The final setup of the DDD, with bottom mount assembly on an FEI Spirit TEM, is shown in Figure 2.9. The cross section shows the detector in the aluminum housing with the adjacent Faraday plate. The cold finger runs the length of the detector and ends at the peltier cooling device at the front panel.

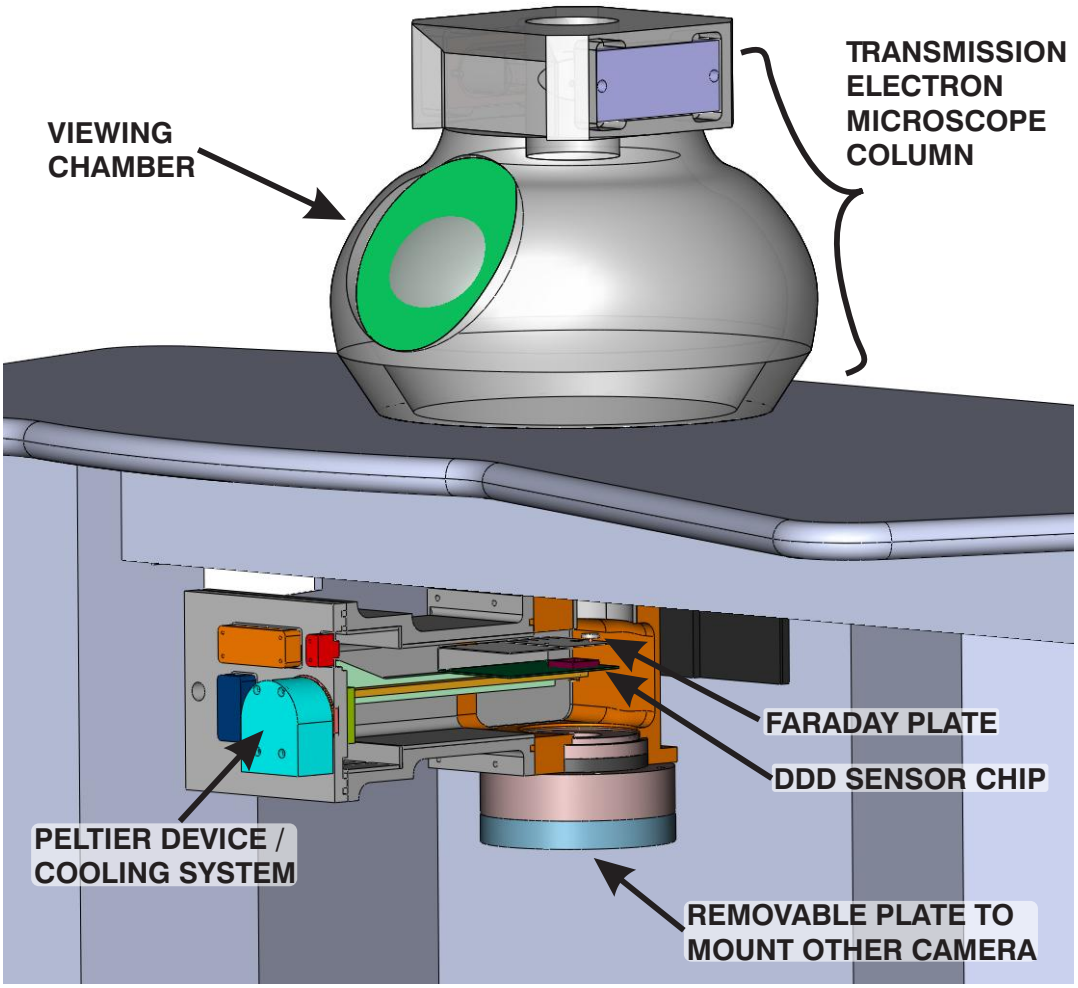

Figure 2.9: Diagram illustrating the large format DDD bottom mounted to a TEM, the experimental setup for all imaging experiments on an FEI Spirit. A cross sectional representation shows the Faraday plate adjacent to the sensor. A removable plate beneath the DDD allows for mounting other cameras.

2.3.2 Transmission electron microscopes

Two different transmission electron microscopes were used for the experiments described in this thesis. A general description of each model as well as the reasons for choosing these microscopes is discussed below.

Transmission Electron Microscope for 200keV experiments

A JEOL JEM2000EX 200keV TEM was used for the characterization experiments of the large format DDD. Since the earlier DDD prototypes were all tested on JEOL brand microscopes, the mounting system described in Section 2.3.1 was already designed and fabricated. This allowed initial testing of the large format DDD system to move forward quickly. With the film drawer mounting scheme, in which neither the CCD camera nor the DDD were retractable, the DDD sensor was placed off axis so that a CCD camera placed underneath would not be blocked. While this configuration worked well for characterizing the DDD, imaging biological specimen proved to be challenging. The sensor was approximately 10cm from the center of the viewing screen, making it difficult to locate specimen with respect to the sensor. In order to quickly acquire as much biological data with the large format system as possible, while continuing developing towards a production system for use at the NCMIR, it became necessary to switch to a newer, more easily automated TEM.

Transmission Electron Microscope for 120keV experiments

The DDD was moved from the JEOL JEM2000EX microscope to an FEI Spirit 120keV TEM for the imaging and tomography experiments. Although the spatial resolution of the DDD is worse at 120keV as compared to 200keV, this change was made for two reasons. First, the bottom mounting system allowed for the DDD to be placed directly on axis with the beam and focusing screen of the TEM. This allowed for much easier alignment of the specimen with the camera. Second, the JEOL 200keV TEM has limited automation capabilities and no stage control. This makes automation for tomography and for mosaic imaging infeasible.

Chapter 3

Detector characterization

In this chapter the results of a thorough characterization of the large format (1024×1024) DDD are reported. Both the operational characteristics and the performance capabilities have been measured. These results are necessary for the calibration and interpretation of images acquired with the DDD. In particular they allow the determination of bad pixels and of the pixel gain variation. Basic characterization has also allowed us to debug unforeseen hardware and firmware issues and to ensure a properly functioning imaging system prior to its use in a microscope. The characterization was performed in two steps. First, the basic operational characteristics were explored on a lab bench. Second, the DDD was mounted on transmission electron microscopes and the detector response to single electrons, the modulation transfer function, the noise power spectra and the detective quantum efficiency were measured. A full quantitative analysis of the imaging capabilities has been performed, which has led to insights into future design improvements.

Characterization of the large format (1024 x 1024 pixel) DDD was only performed using 120 and 200keV electrons. The design of the large format DDD is very similar to a prototype one quarter the size. Characterization of this smaller chip has been performed with incident electrons of up to 400keV. The results from the medium format (512 x 512 pixel) DDD are well matched with the large format results at 120 and 200keV [34], thus it can be assumed that the results at these higher energies are also valid for the large format DDD.

3.1 Basic characteristics

Before a thorough assessment of the imaging performance with the DDD could be performed, it was necessary to characterize the properties of the detector with simpler measurements. There were four major components to this characterization. The basic noise properties and performance in the dark with no incident particles are shown, including a quantitative measure of the effect of cooling the sensor, which lowers the dark current contribution to overall noise. An x-ray source was used to determine the ratio between the analog-to-digital converter (ADC) units of a pixel value to energy absorbed by the DDD from a particle interaction in the substrate. Also presented are two other measurements that are crucial for TEM imaging studies, the location of bad pixels and the unique gain value associated with each pixel. And finally, the DDD signal response for single and multiple electron bombardment is also presented. The results of these measurements dictated, in part, what optimal beam intensities and integration times would be used for imaging biological specimen.

3.1.1 DDD performance in dark conditions

Here the response of the detector in the dark without incident particles is shown, both while cooled and at room temperature. A more thorough description of the DDD readout and noise characteristics is described in the previous chapter.

Dark current measurement

The dark current of the system is defined as the signal accumulated on the chip in the dark after a correlated double sampling (CDS) correction has been applied to eliminate the reset noise. The dark current comes from the thermally generated free charge accumulating directly on the photodiode. A necessary post processing step for imaging with the DDD is to average a large number of frames in the dark and then subtract this average dark current from the image.

The noise associated with the dark current results from the difference between the dark current contribution to the current frame and the averaged dark

current image. This noise follows a Poisson distribution, so it is larger for larger dark currents. For this reason it is advantageous to reduce the amount of dark current through cooling.

Figure 3.1 shows the average pixel ADC values from 20 frames for different integration times with the DDD at room temperature and cooled to -16°C. The room temperature measurement was performed on a lab bench while the measurement with the cooled detector was taken with the DDD mounted on a microscope and held under vacuum. Correlated double sampling correction was applied to both data sets.

The dark current values at 53ms integration time are reduced from well over 100 ADC units to 7 ADC units . In addition to reducing the dark noise, cooling is particularly beneficial since at room temperature a significant amount of the dynamic range of the detector is dominated by dark current. Furthermore these results confirm a linear relationship between integration time and dark current indicating that it is unlikely there existed some other form of spurious signal in the system competing with the dark current .

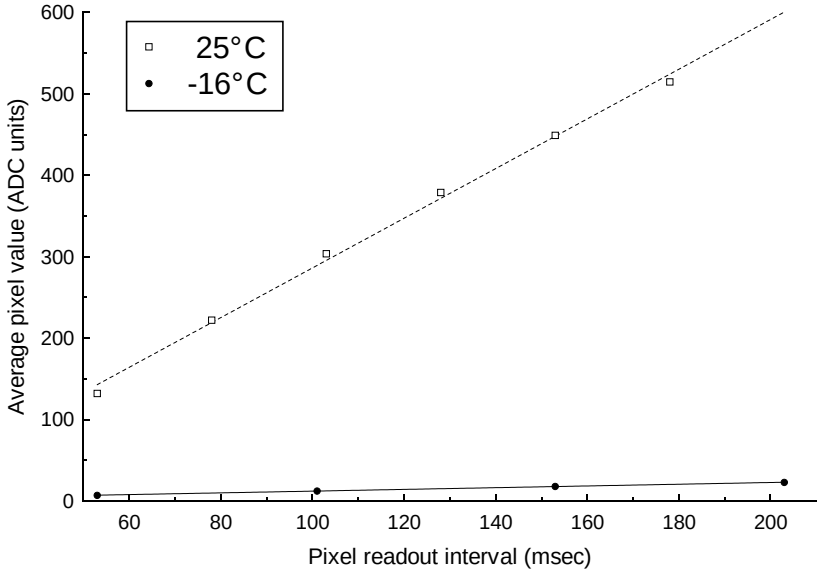

Figure 3.1: Dark current for different pixel readout times for both room temperature and -16°C. The current is reduced by about one order of a magnitude by holding the DDD at the lower temperature.

The following protocol for correction of dark current is used to correct all the experiments described in this thesis. First 200 to 300 frames are acquired in the dark, without incident particles. Then a dark current image is created by averaging all of the frames together. The dark current correction then consists of subtracting this dark current image from any frame being corrected.

Pixel values after dark current and CDS correction

The DDD was cooled to -20°C and 1000 frames were recorded with an exposure time of 53ms. For each frame current and correlated double sampling correction were then applied. Figure 3.2 shows the histogram created from all the pixel values in the 1000 frames. The results show a mean value of 0.5 ADC units with standard deviation of 3 ADC units. These values mean that a noise floor value of 30 ADC units can be safely used as a threshold value for the detection of an incident electron or x-ray.

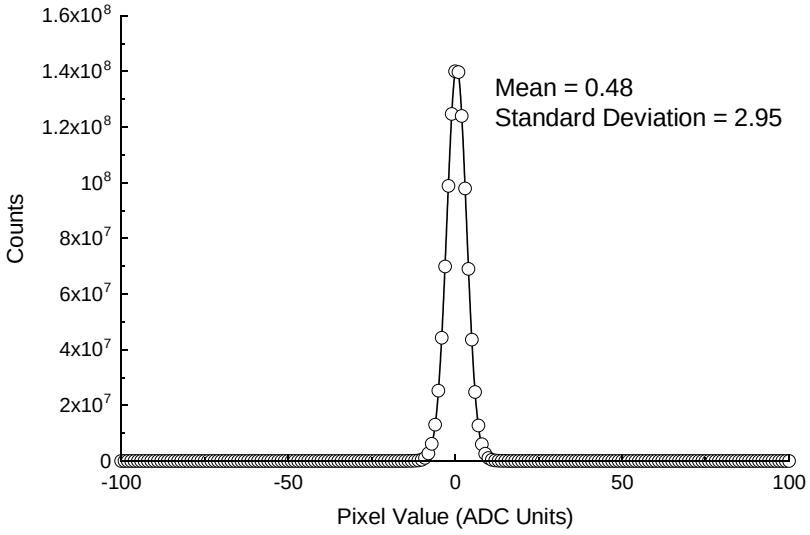

Figure 3.2: Plot shows histogram of pixel values from 1000 frames with no incident particles and applied dark current and CDS correction. The standard deviation is 2.95 ADC units showing that a noise floor value of 30 ADC units could be used as a threshold value for the detection of an incident electron or x-ray.

3.1.2 Energy calibration measurement with x-rays

In order to find the energy deposited in the detector from the pixel ADC values, a calibration with an x-ray source was used. Unlike electrons, an x-ray deposits all of its energy at the single site of interaction. Thus by knowing the energy of the x-rays emitted by radioactive sources we can calibrate the ADC values with energy deposition. For this measurement, an Fe^{55} source with x-rays of 5.9keV was chosen.

Methods

X-ray sources cannot be placed in the vacuum column of a microscope, where most of our other measurements were performed, due to safety considerations. Instead, the DDD was placed into a plastic bag that was flushed with dry nitrogen to minimize any chance of frost on the detector or electronics. It was then

inserted into a thermal chamber and cooled to -25°C. An Fe^{55} source was placed above the detector and 20,000 frames were recorded. An average dark current subtraction and correlated double sampling correction were applied to the data prior to analysis of x-ray events. An x-ray event is defined as a cluster of adjacent pixels with a readout of at least 40 ADC units for one of the pixels. This threshold was chosen because it was well above the noise of an average pixel. The center of the event was the pixel with the maximum value in this cluster.

Results

Figure 3.3 shows the average from 9000 events in 500 frames where the center of the events were lined up on top of each other and averaged together. Since there were approximately 18 x-ray events per frame, there was a low possibility of two or more x-rays hitting the same area and skewing the results to show more energy deposition.

0	0	0	0	0	0	0
0	0	0	0	0	0	0
0	0	3	8	3	0	0
0	0	8	75	8	0	0
0	0	2	8	3	0	0
0	0	0	0	0	0	0
0	0	0	0	0	0	0

Figure 3.3: The average of ≈9000 events Fe^{55} x-ray events detected by the DDD is shown. Most of the energy is deposited in a 3×3 pixel area.

From these ≈9000 events, we see that the energy is, on average, deposited in a 3 × 3 pixel area. Since this is based upon an average of a very large number of events, of which some would have had energy deposited in a larger area, a 5 × 5 pixel area was summed to find the energy deposited in each event. The resulting histogram of the sum of 5 × 5 pixel area of about 338400 events from 18800 frames is shown in Figure 3.4. Since the peak value of the histogram is 148.82 ADC units, we divide by the Fe^{55} x-ray energy of 5.9keV to get the calibration value of 25 ADC units per keV of energy deposited in the detector. The lack of perfect symmetry in the Gaussian distribution of the energies in the histogram is most likely due to readout noise. A histogram of a 7 × 7 array showed the same peak value, ensuring that the measurement area was adequate to detect the full x-ray energy.

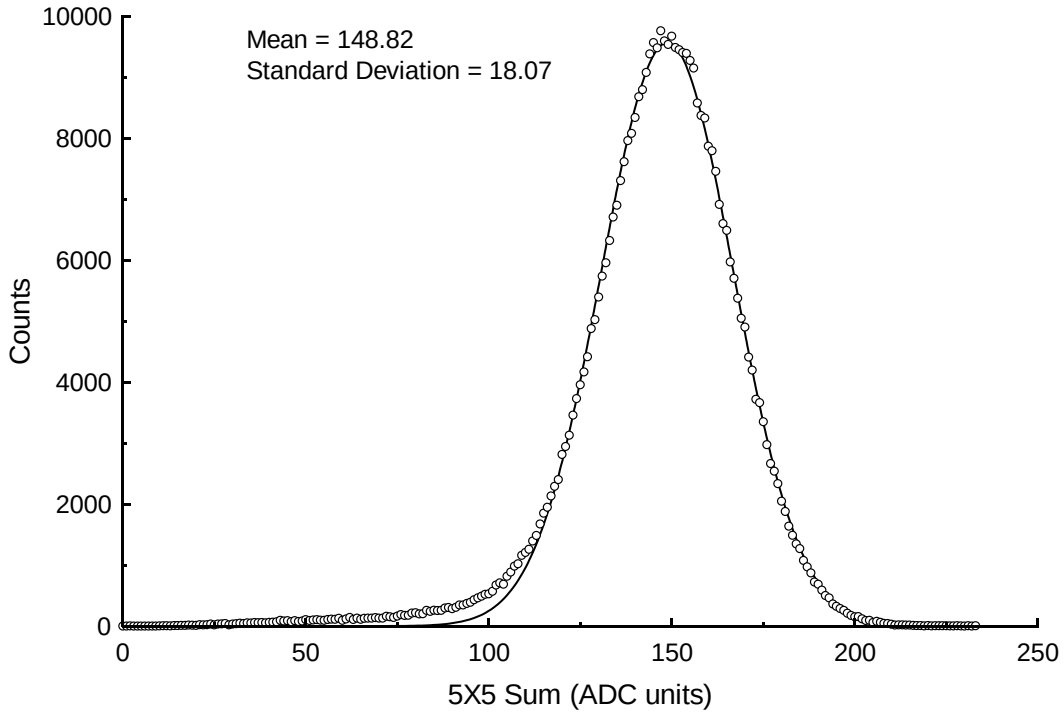

Figure 3.4: Fe^{55} histogram of energy deposited in the detector in a 5×5 pixel area. The peak value of 149 ADC units is divided by the Fe^{55} x-ray energy of 5.9keV to get the calibration value of 25 ADC units per keV of energy deposited in the detector.

3.1.3 DDD signal response to electron dose and incident electron energy

The response of the DDD to electrons as a function of dose and incident electron energy was measured to find the optimal dose conditions to acquire images with the DDD. The optimal dose will provide signals near the top of the range where DDD response is linear. This will provide the best signal to noise ratio, while maintaining the simplicity of a linear response.

Methods

This measurement was performed by flood illuminating the DDD at different electron doses while maintaining a total integration time of 153ms. The data were collected on a JEOL 2000EX electron microscope with 200keV electron energy and on a FEI Spirit with 120keV electron energy. The detector was cooled to approximately -15°C to reduce dark current and radiation damage to the detector. The beam intensity was measured by the Faraday plate adjacent to the detector. A set of 20 frames was recorded at each dose level. After averaging the results of 20 frames, a histogram was created of the frequency of the average ADC count value of each pixel. Each frame had a dark current and correlated double sampling correction applied.

Results

Figure 3.5 shows the mean ADC value from a histogram of all the pixel values at each dose. The Faraday beam intensity value was converted from pA/cm^2 to electrons/pixel/frame. This figure shows that the detector response is linear in the region of a dose of 0 to 4 electrons/pixel/frame for 120keV electrons. Above this dose, the DDD's response is nonlinear and would distort imaging results. The DDD has a higher dose linearity threshold for 200keV electrons because less signal is deposited in each pixel with a higher incident electron energy since there are fewer Coulomb interactions to deposit energy. A higher dose per frame is desired since there is some amount of reset noise introduced to each frame, making it desirable to reduce the number of frames that need to be summed. The fewer number of frames one sums together the better the signal to noise ratio for final image.

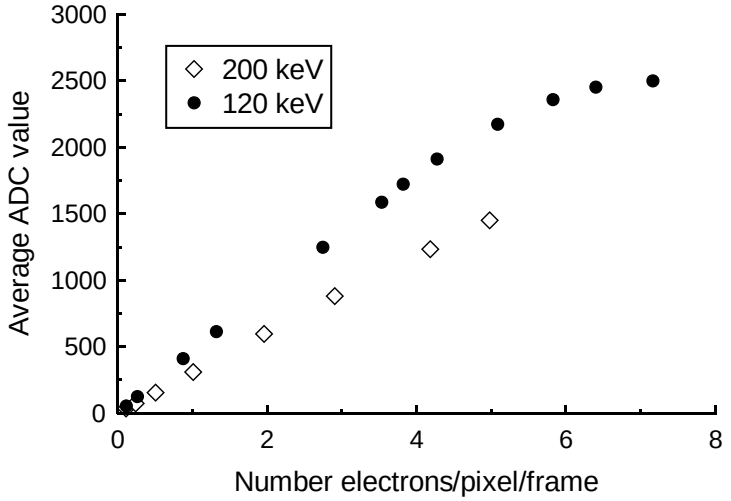

Figure 3.5: Plot shows the signal response as a function of electron dose. The linearity of the DDD response degrades above 3 or 4 electrons/pixel/frame, showing that the optimal imaging dose per frame should be lower than this amount.

From Figure 3.5, imaging at a dose of approximately 2 electrons/pixel/frame would ensure a linear detector response. Figure 3.6 shows that changing the total integration time from 153ms to 53ms does little to change the detector response to dose for 120keV electrons. From these results, it was decided that biological imaging would be carried out at a dose between 2 and 3 electrons/pixel/frame.

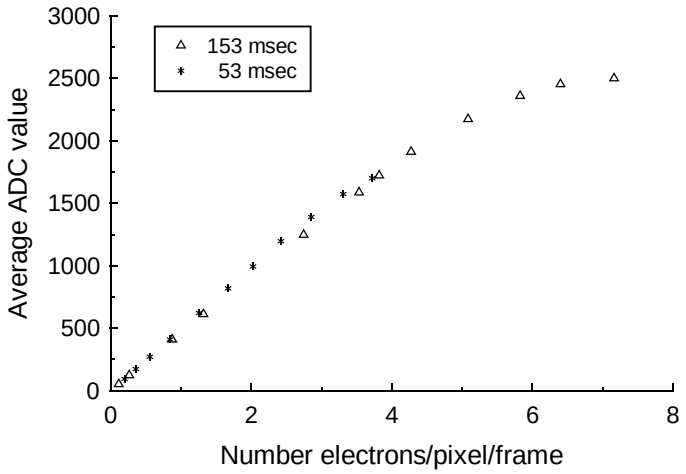

Figure 3.6: Plot of signal response with different integration times of 53 and 153ms. This measurement confirms that integration time does not affect signal linearity. 120keV electrons were used to acquire this data.

3.1.4 Bad pixels

From earlier prototypes, it was known that the DDD would likely have a small percentage of pixels that are unusable for imaging since their values fluctuate to very high and low values without the presence of any input signal. To find the bad pixels, generally 1000 to 2000 frames are recorded in the dark. The first 100 frames are averaged and then subtracted from subsequent frames to reduce the effect of the dark current. The most likely standard deviation value of a pixel for each ADC sector is then computed. A threshold ADC value is then found for each sector by multiplying the most likely standard deviation by 7, an empirically generated value. Once this process is finished, bad pixels are found in the same data set by comparison to the appropriate sector threshold. If the value of a pixel is greater than the threshold, the location is noted and written to a file. A correction

for bad pixels for an image acquired with the DDD is performed by taking the average of the pixel values immediately adjacent to the bad pixel and using that value as a replacement for the bad pixel.

Employing this algorithm, the average number of bad pixels is 1.6%. Although these pixels are uniformly distributed across the face of the detector, many more occur at the edges of the detector. The first and last few columns and rows tend to have a very high percentage of bad pixels or pixels with very high gain and the images are often cropped from 1024×1024 pixels to 1020×1020 pixels to mitigate this effect.

Figure 3.7 shows that the distribution of the bad pixels is uniform over columns and rows so that the failure of this correction from the existence of adjacent bad pixels is a rare occurrence. This uniform distribution also demonstrates that there are no large defective regions of the sensor which can occur during the manufacturing process.

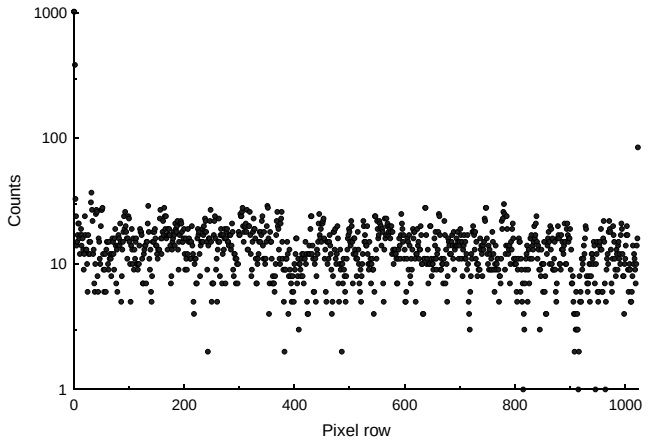

(a) Bad pixels in rows

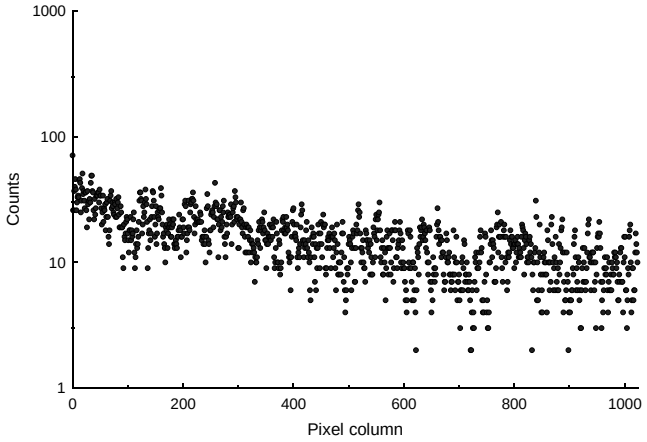

(b) Bad pixels in columns

Figure 3.7: Histograms of the distribution of bad pixels across rows (Figure 3.7(a)) and columns (Figure 3.7(b)) in sensor. The 1.6% bad pixels are uniformly distributed across the chip, except for the edges of the sensor that are expected to have a higher percentage of bad pixels.

3.1.5 Pixel gain determination

On the whole, the pixel response across the detector is fairly uniform. However, some small gain variation does occur where the pixel gain is defined as the unique signal response amplification that each pixel has to input charge. Contri-

butions to this gain variation are the CMOS manufacturing process, the source follower and unity gain buffer reading out the pixel voltage, the gain differences in each of the 16 analog to digital converters used to read out the detector and any physical barrier that attenuates the response such as adsorbed material on the detector face. Correcting for these gain differences is a standard practice in all digital imaging systems and was necessary to achieve the best images with the large format DDD.

Uniform electron beam measurement

A reasonable estimate of pixel gain values can be made by recording with uniform beam flux for a long enough time to collect a large number of electrons per pixel. Although the Landau distribution of energy deposited in the detector makes this a less than ideal method, the results proved to be adequate for correcting images. The method used to measure the pixel gain variation was to illuminate the DDD with a uniform beam of a flux of approximately 2 electrons/pixel/frame for 1000 frames. The average ADC value for each pixel was found by summing the ADC values and dividing by the total number of frames. An average value of the set of average pixel values was then calculated. The gain value then for each individual pixel was the average value of all the pixel values divided by individual average pixel value.

Figure 3.8 is a histogram of the gain values for each pixel. The results are only shown for gain values between 0.8 and 1.2. While full range of the gain values is from 0.252 to 414, these few outliers are not included in the histogram in order show the overall uniformity of the detector pixel gain values. The mean for this histogram is 1.003 with a standard deviation of 0.023 showing that the gain variation across the detector is minor, though still large enough to benefit from gain correction.

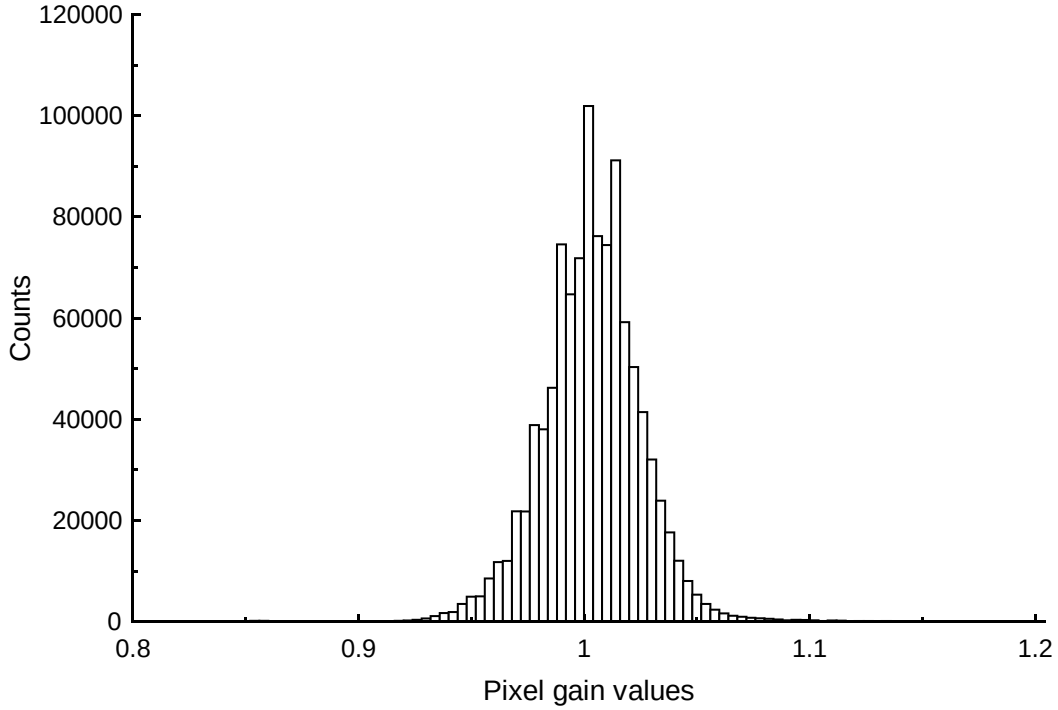

Figure 3.8: A histogram of the pixel gain values demonstrates the Gaussian, low pixel to pixel gain variation for the DDD. The mean is 1.003 with a standard deviation of 0.023. The full range of the gain values are from 0.252 to 414, but the range is condensed since these represent a tiny fraction of pixels.

Figure 3.9 shows a 2D image where each pixel value represents the gain of that pixel. The contrast has been enhanced by restricting the lower and upper bounds on the image values to 0.9 and 1.1 to make the different gain values of the ADC sectors apparent. The bands that are apparent are from the gain variation from the ADC readout electronics. Also apparent in this image is some slight non-uniformity across the detector face that is most likely due to either oxidation of the protective coating of the detector, or material adsorbed onto the detector surface.

While a uniform electron beam correction for individual pixel gain works well, it has the significant drawback that it requires a large dose of electron signal

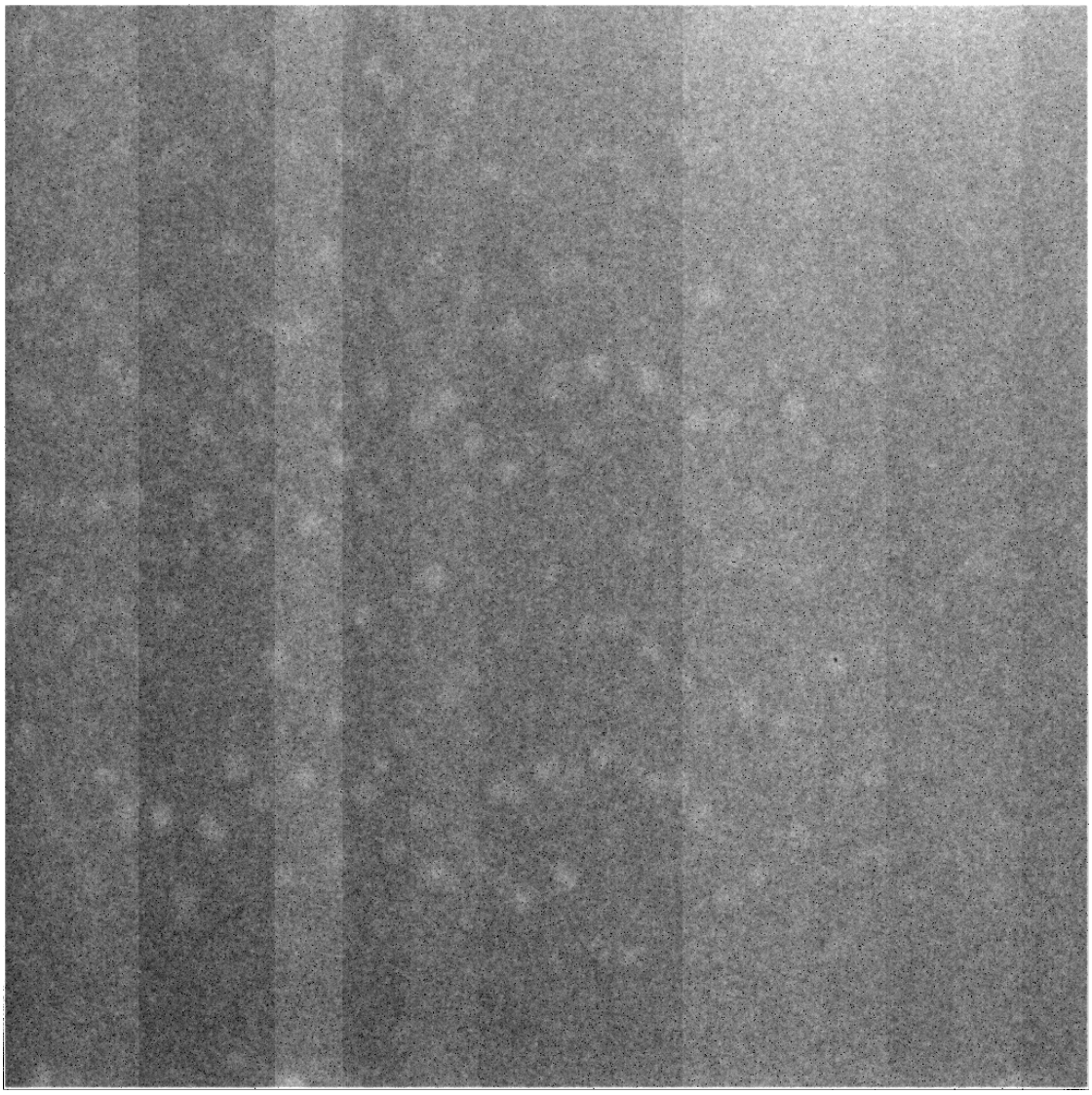

Figure 3.9: A 2D image is shown where each pixel value corresponds to the pixel gain calculated from a flood illumination measurement with the DDD. Due to the low variation in pixel gain, the contrast was enhanced by restricting the lower and upper bounds on the image to 0.9 and 1.1 respectively, thereby allowing us to see the 16 parallel readout sectors on the face of the chip as well as minor non-uniformity across the detector face due to oxidation of the protective coating or material adsorbed onto the detector surface.

causing radiation damage and shortening the immediate usability of the detector. Since the gain of the pixels changes over time, this measurement has to be repeated periodically. Ideally a photon source, such as a uniform beam of light, would be used for measuring the pixel gain variation instead of electrons. There are two reasons for this. The first is that the light would not cause radiation damage. The second is that all the energy of a photon would be deposited in the detector instead of a range of energies as is the case with electrons.

3.1.6 Single electron studies

An examination of the characteristics of single electrons striking the DDD gives a great deal of insight into the detector performance and was a critical measurement to perform before commencing TEM imaging studies. As described in Section 2.1.2, when a single electron strikes the DDD and passes through the sensitive epitaxial layer, on average about 1000 electrons are liberated through Coulomb interactions and diffuse toward the photodiode in the center of each pixel [43]. Therefore there are many pieces of information about the DDD to be learned from examining single electron hits. The single electron studies show how much the charge deposited in the detector typically spreads and a point spread function estimate can be obtained. This measurement also shows that unlike the x-ray measurements where an x-ray's energy is fully deposited in the sensor, the energy deposited in the DDD by an electron passing through the sensor has a Landau distribution. This is the expected distribution and confirms that the detector is functioning properly [39]. From previous studies with an earlier prototype [54], an unusual feature of the Landau distribution led to the discovery of back-scattered electrons depositing more energy in the detector than expected.

Methods

The single electron measurements were performed on a JEOL-JEM2000EX microscope for 200keV and on a FEI Spirit microscope for the 120keV incident electron energies. The detector was cooled to approximately -15°C. The incident electron beam dose was measured using a Faraday plate adjacent to the sensor.

The electron beam was decreased to less than 0.01 pA/cm^2 and a total integration time of 53ms was chosen. This very low flux was used to try to minimize the chance of more than one electron striking the same pixel region of the detector at a time. 2000 frames were acquired with this current, and 300 frames without a beam were used to correct for the dark current. The data were not corrected for pixel gain variation though bad pixels were eliminated. A noise floor threshold of 30 ADC units, determined from the noise measurement described above, was used to determine whether an electron event had occurred in a pixel.

The algorithms used to determine that an event occurred are described as follows. First the area to look for an event was constrained to be inside a sub area of the detector from row 20 to row 1003 and column 20 to column 1003, eliminating a 20 pixel border along all edges of the detector. This was done to take into account that the edge columns and rows are usually noisier than the rest of the detector, as well as the problem of events spreading charge in an area asymmetrically. The pixel values were then compared to the noise floor of 30 ADC. If a pixel had a value higher than 30 ADC, first a check is performed to see if the pixel is one of the known bad pixels as defined previously in this chapter. If it was not a bad pixel, then the neighboring pixels are checked in a predefined square area to see if any other pixels have values higher than the chosen pixel. If no pixels in the neighboring vicinity have higher values, this pixel is determined to be the center of the event.

For measuring the energy deposition distribution, the pixel values in a 9×9 matrix are summed and binned into a histogram. For obtaining a point spread function estimate for a single electron, an event is added to a 9×9 matrix where the highest value is placed in the center of the matrix. The average value is finally found by dividing by the number of events added to the matrix. A 9×9 matrix was used for the 200keV single electron analysis. Due to greater charge spread in the sensor and more back scattered events, a 15×15 matrix area was used for the 120keV analysis, although only a 9×9 area is shown in the results.

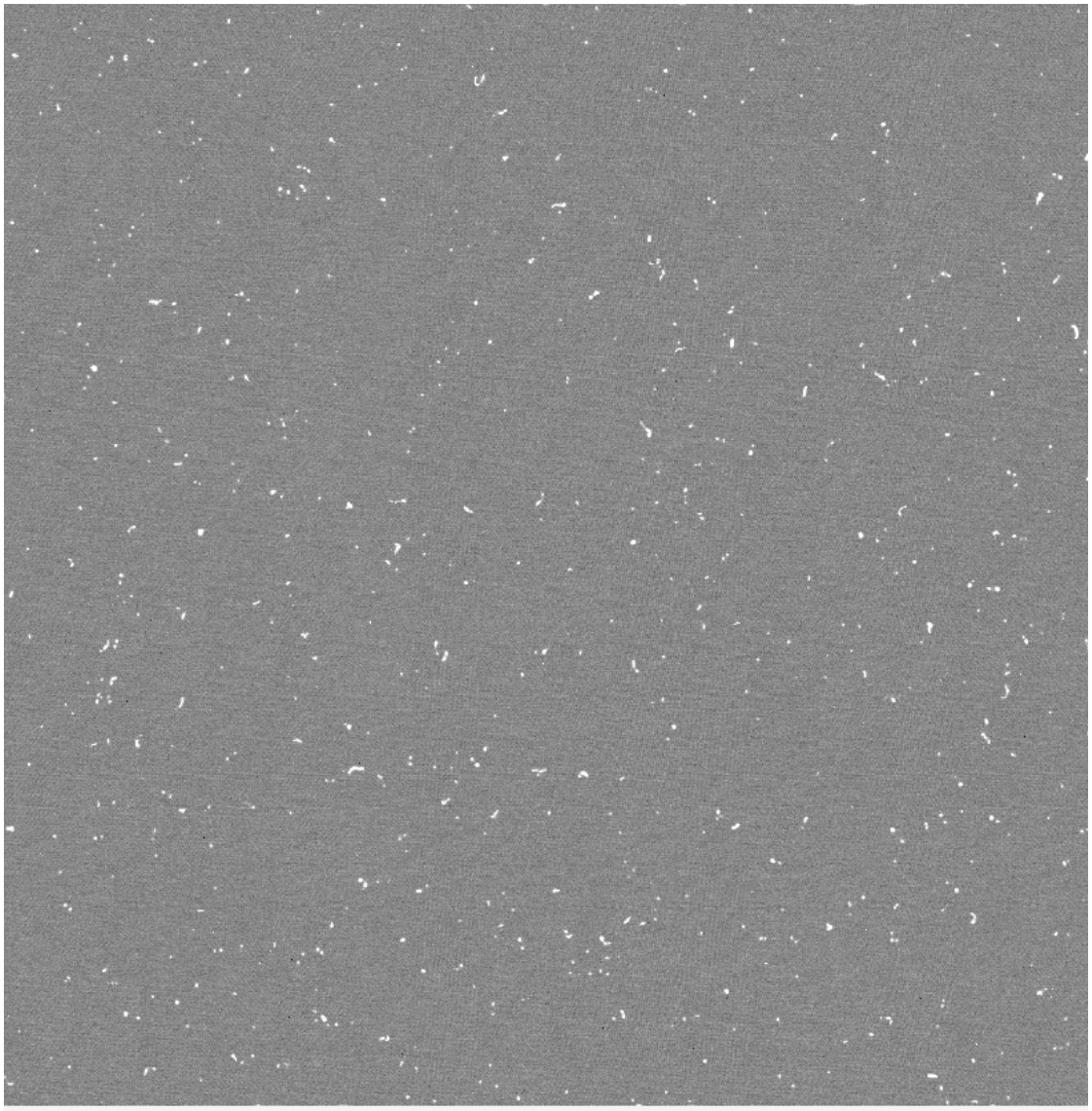

Figure 3.10: Low beam flux image showing single electron energy deposition. Asymmetry and scattering within the silicon are visible for some particles.

Results of typical electron event

Figure 3.10 shows a very low flux image from a single frame. The purpose of this figure is to demonstrate some interesting features of the single electron sensitivity of this detector. Many events have asymmetric energy distributions due to multiple scattering in the silicon and these interactions are easily visible in the image. Some degradation of resolution occurs from a wide variety of spatial interactions.

Results of energy deposition distribution

Figure 3.11(b) shows the histogram of the energy deposited in the sensor by incident electrons of 200keV where 105,905 events were detected in 2000 frames and with an average of 53 events per frame out of one million pixels. This low number of events per frame ensures a very low probability that more than one incident electron was involved in creating an event. Figure 3.11(a) shows the results with 120keV electrons where 262,002 events were detected in 2000 frames. This higher flux of events explains why the graph shows 15 events had energy deposition greater than 120keV, indicating that a small fraction of multiple electron events was included in the data.

As expected, the histograms in Figure 3.11 show a Landau distribution [39] below 10keV with a peak at 8.4keV and 6.4keV, for 120keV and 200keV incident electrons respectively. However, many events have unexpectedly higher absorbed energy values. The higher energy deposition was observed in an earlier prototype DDD [54] and explained through extensive simulation as the result of incident electrons that are back-scattered in the silicon substrate (250μm thick) and re-enter the sensitive epitaxial region a second time. These back-scattered electrons deposit more energy in the detector because they have a much lower velocity. The best way to reduce these back-scattered electrons would be to thin the 250μm silicon substrate down to 30μm. While this process has been explored, the data in this thesis come from a chip that is not thinned. However, the effect of the back scattering may be limited by utilizing a maximum dose per frame while imaging due to the limited dynamic range of the sensor.

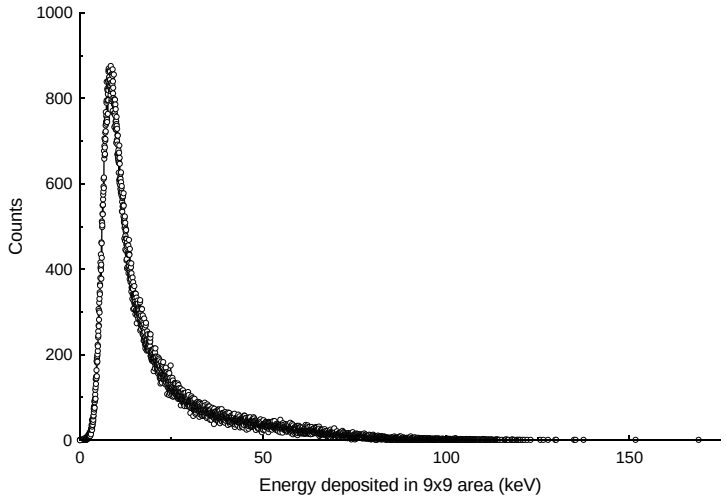

(a) 120 keV events

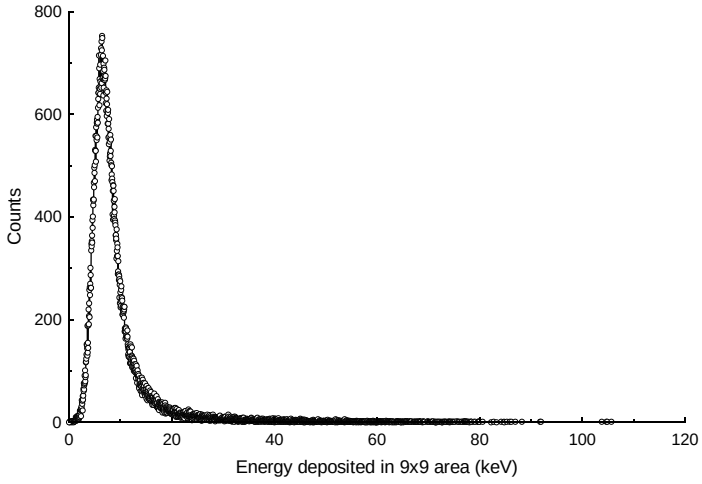

(b) 200 keV events

Figure 3.11: The histograms of energy deposited in the sensor by electrons show the expected Landau distribution. In order to collect all the charge from one incident electron, the values from a 9×9 array were summed to obtain the energy deposited.

Results of pixel resolution estimate and signal to noise estimate

Figure 3.12 shows the results of the averages of the single electron events for 120keV and 200keV incident electrons. The pixel value at each pixel position was added to the sum of all values of the pixel in equivalent positions in previous cases. At the end of a run, this sum was divided by the number of cases i.e. the number of detected electrons. The average distribution has significant values only inside a 5×5 array and 3×3 array centered on the maximum values for the 120keV and 200keV data respectively. The low background values outside the maximum areas are non zero because high energy back scattered events were not excluded from this analysis. The background goes to zero outside the centroid when they are.

Calculation of the signal to noise ratio estimate is given in Equation 3.1. The noise is defined as the standard deviation from Figure 3.2, while the signal is found by summing over a 7×7 array. This results in a signal to noise ratio estimate of 17:1 for 120keV electrons and 10:1 for 200keV electrons, when the highest backscattered events are removed from the analysis.

$$\text{signal to noise ratio} = \frac{\sum_{\text{n}\times\text{n pixel area}}}{\text{Noise}} \tag{3.1}$$

The average energy deposition data also allow us to make a spatial resolution estimate. Plotting the 2D line spread function from this centroid, we can fit a Gaussian to the resulting curve which results in full width at half maximums of 7.2μm and 6.8μm for 120keV and 200keV data.This FWHM is due mostly to the fact that the incident electrons are distributed all over the central pixel. If we suppose this distribution to be Gaussian with a FWHM of 5μm (the size of a pixel) then we can try to de-convolute the result. Using Equation 3.2, resolution estimates for a single electron are 5.2μm for 120keV single electrons and 4.7μm for 200keV single electrons.

$$\text{resolution estimate} = \sqrt{\text{FWHM}^2 - \text{pixel size}^2} \tag{3.2}$$

1	1	1	1	1	1	1	1	1
1	1	1	2	2	2	2	1	1
1	1	3	5	7	5	3	1	1
1	2	5	16	30	16	5	2	1
1	2	7	30	114	30	7	2	1
1	2	5	16	30	16	5	2	1
1	1	3	5	6	5	3	2	1
1	1	1	2	2	2	1	1	1
1	1	1	1	1	1	1	1	1

(a) 120 keV

3	-2	1	0	0	1	0	0	1
0	0	1	1	0	1	0	0	0
0	1	1	1	2	2	0	1	1
1	0	0	7	14	7	2	0	0
1	1	2	15	68	17	2	1	0
1	0	1	7	17	7	1	0	0
0	0	1	2	2	1	0	0	0
0	0	0	0	1	0	0	1	0
0	1	0	0	0	0	0	0	0

(b) 200 keV

Figure 3.12: The figures show the average energy deposited by ≈100,000 events for 200keV single electrons or ≈250,000 events for 120keV single electrons. Each element of the array represents a DDD pixel with an associated value. For each event the pixel with the largest value was placed at the center of the array. The non zero background is due to small percentage of high energy depositions caused by back scattered electrons that tunnel from the silicon substrate back into the sensitive epitaxial region of the detector. Signal to noise and resolution estimates can be calculated from these data for 120 and 200keV. Note that most charge is collected within a 5×5 area.

Limitations to the signal to noise ratio and pixel resolution estimate

It is important to note that while the single electron studies provide important information about the sensor, there are limitations to the data analysis. The first limitation is that a 30 ADC unit threshold was applied to determine whether an electron struck the detector to differentiate between noise and actual events. Due to the nature of the Landau energy deposition distributions, there are electrons that deposit energy with less than the 30 ADC cutoff. Therefore, this analysis tends to overestimate the signal to noise ratio slightly. In addition, the estimate of the pixel resolution is overestimated for the same reason. Events below 30 ADC would have a very small energy spread outside of one pixel. The final potential limitation to the single event analysis is that an assumption is made that the largest pixel value is where the incident electron struck the detector. Simulations from other groups [20, 4] show that this is not always the case. This matter is discussed in much greater detail in Section 3.2.5, however, the basic characterization including the single electron studies confirmed the expected behavior of the large format DDD compared to the same studies performed with earlier prototypes. This allowed us to proceed forward with more careful measurements of performance and begin imaging experiments.

3.2 Thorough characterization of imaging properties

The basic characterization of the DDD provided a good deal of information about the performance of the sensor under dark conditions, x-ray detection, and single electron event sensing. However, while previous feasibility studies [54, 34, 33] have demonstrated the key advantages of this sensor, a complete quantitative characterization of the detector had not yet been performed. The two main quantitative measurements of imaging systems are the modulation transfer function (MTF) and the detective quantum efficiency (DQE) [5]. This section of the thesis provides a detailed description of the qualitative meaning of the MTF and DQE as well as

the theory underlying the algorithms used for this analysis. Analysis of the noise power spectrum (NPS) is also presented.

Guidelines set out in a European International Standard on measuring x-ray devices [1] were used to calculate the MTF, NPS and DQE. These measurement techniques do not depend upon detector design and thus allow for easier comparisons with any other TEM imaging devices.

This analysis was carried out in collaboration with Dr. Grigore Moldovan, a post doctoral researcher of Professor Angus Kirkland from the Department of Materials at Oxford University. Dr. Moldovan wrote the analysis scripts that were executed using imageJ, a software tool for image processing, to calculate the MTF, NPS and DQE [67].

3.2.1 Experimental setup and methods

As described in Chapter 2 Section 2.3.1, the DDD was mounted in a modified film drawer of a JEOL JEM 2000EX TEM for the measurements using a 200keV electron beam. The 120keV beam measurements were carried out on an FEI Spirit TEM with the DDD mounted in a custom housing beneath the viewing chamber. In both cases the sensor was cooled to -15°C to minimize radiation damage and decrease dark current noise. Incident electron beam dose was measured using a Faraday plate adjacent to the sensor.

Three data sets were recorded to measure the MTF and DQE at 120keV and 200keV. In order to calculate the MTF, images of a projected shadow of an object with a straight edge were captured with the DDD. For the 200keV measurement, the TEM beam stop, a thin wire above the TEM scintillation screen, was used as the edge. A thin steel cylinder was affixed to the metal housing of the detector assembly above the mechanical shutter for the 120keV measurement.

The DDD was flood illuminated with a uniform electron flux to provide suitable bright field data required for detector DQE and pixel gain values. The beam density for the edge and bright field data sets was ≈2 electrons/pixel/frame. A third data set without an electron beam was also recorded to obtain pixel dark noise values. For each data set, 1005 frames were recorded and a total integration

time of 153ms per frame was used. The first 5 frames were not included in the data analysis to allow the DDD to equilibrate. The remaining 1000 frames were divided into 20 images that were formed by summing 50 sequential frames. Thus the total dose was just under 100 electrons/pixel in each image. This low number of incident electrons was chosen because imaging of radiation sensitive specimens was a projected application of the large format DDD. The edge shadow images were corrected for variations in pixel gain by using the average of the bright field images. The data set without any beam was used to correct for dark noise levels in the images of the edge shadow.

3.2.2 Modulation transfer function

A qualitative description of the MTF is that it measures the sharpness of an image. A detailed description of the analysis methods and results for the MTF is described below.

Analysis

The edge image (shown in Figure 3.13) is corrected for pixel gain variation using the bright field data set and for dark noise using the data set without an electron beam. The average profile of the edge shadow in one dimension was found by oversampling the data with a factor of 8 points/pixel. Figure 3.14(a) shows the sharp transition in a one dimensional plot of the average edge. The fixed step derivative of the edge profile yielded the point spread function shown in Figure 3.14(b). The MTF was calculated by taking the absolute Fourier transform of the point spread function.

Results

Figure 3.15 shows the MTF calculation for 120keV and 200keV electrons. At high spatial frequencies the MTF decreases suddenly due to strong scattering of incident electrons which is expected for imaging systems used in TEM [52]. The MTF dependence on incident electron energy is also shown in Figure 3.15. At low

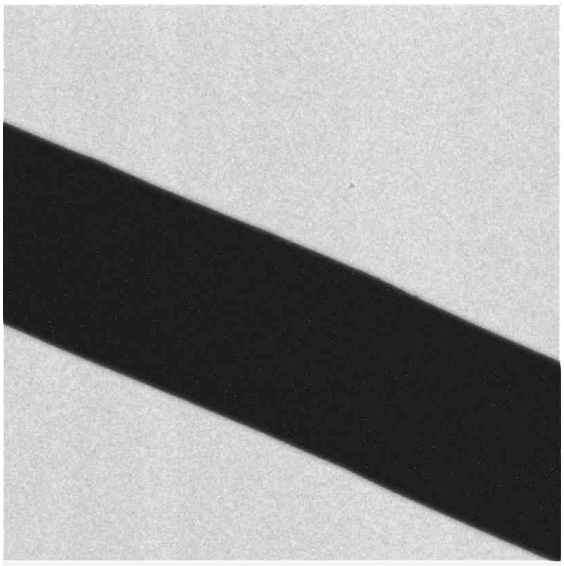

Figure 3.13: An edge image used in the MTF measurement.

spatial frequencies the MTF decreases at 200keV compared with 120keV. This can be explained by the inherent scattering interactions in the silicon.

Figure 3.15 also includes data points available from commercial vendors of TEM CCD cameras [31, 72]. The best MTF achievable with most commercial CCD camera systems is up to 50 lines/mm, whereas the MTF of the DDD can transfer modulation up to 100 lines/mm. This difference is due in large part to the smaller pixel size of the DDD (5μm) compared with commercial CCD systems (15 to 25μm pixel size). Furthermore, a CCD camera has a phosphorescent scintillation screen to convert the beam electrons to photons and the signal spread from the beam electron is close to 30μm, nullifying any benefit from the use of smaller pixels with the CCD. The design of the DDD, with a small sensitive epitaxial layer, causes the spread of the incident electron to be much less. Half the Nyquist limit, or 25 lines/mm, for CCD cameras shows an MTF of 10-20% whereas for the DDD, MTF with 200keV electrons is 30%. Moreover, modulation transfer is 5% beyond 65 lines/mm, dropping to 1% at the 100 lines/mm limit.

On the whole, these results show that the MTF is higher with the large format DDD than most commercial CCD cameras. From this measurement, images acquired with the DDD ought to have edges that appear more crisp and well defined

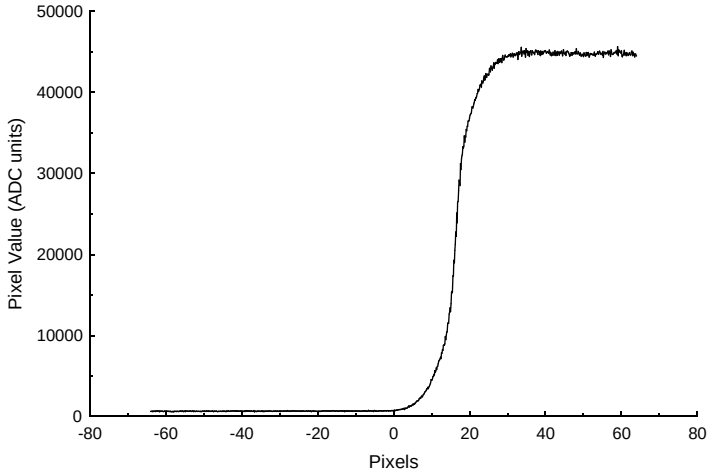

(a) Average edge profile plot

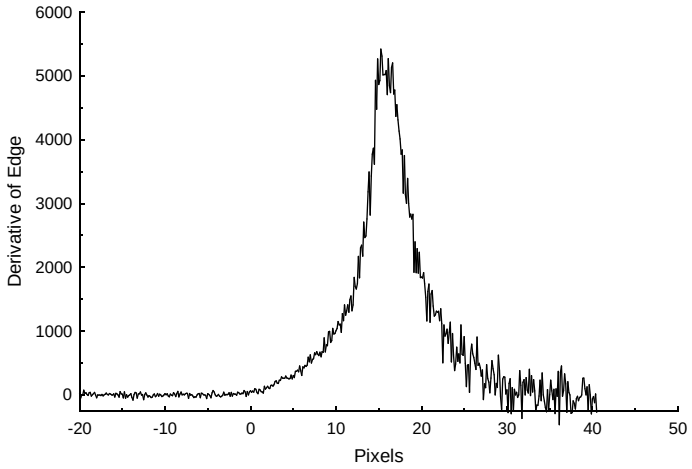

(b) Point spread function

Figure 3.14: Intermediate steps in the calculation of the MTF are shown. The average edge profile, oversampled by 8 points/pixel, is shown in Figure 3.14(a). A fixed step derivative of Figure 3.14(a) resulted in the point spread function shown in Figure 3.14(b).

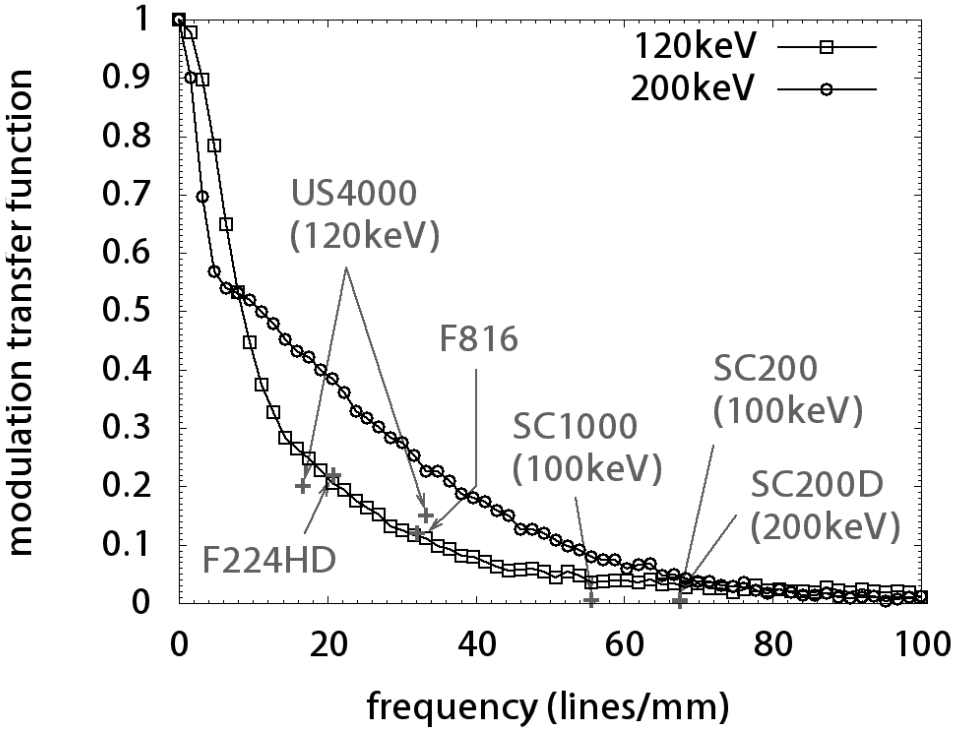

Figure 3.15: Modulation transfer functions for images recorded with 120keV and 200keV electrons, compared to those of commercial cameras. Scatter points represent data reported by manufacturers for conventional CCD cameras, with electron energy in brackets (when provided). Cameras US400, SC1000, SC200 and SC200D are manufactured by Gatan [31]; cameras F224HD and F816 are manufactured by TVIPS [72].

compared to most commercial CCD cameras.

3.2.3 Noise power spectrum

The NPS goes beyond the basic characterization of noise covered in Section 3.1.1 and takes into account the distribution of noise variations across the surface area of the DDD. The results presented have been normalized by dividing by the electron beam flux, allowing for better comparison between the 120keV and 200keV results that had slightly different average dose per image.

Analysis

The average NPS was obtained from the bright field images and the images with no beam. Dark noise correction was applied to the bright field images from the dark images. A pixel variation gain correction was applied to each bright field image from the average of the bright field images. The noise power spectra were calculated by taking the Fourier transforms of the bright field images. The final NPS was obtained by radially averaging the results from the individual bright field images. Finally, to get the normalized NPS, the results were divided by the average dose in the images. The average dose was computed from the slope of the linear detector response to electrons. For 120keV this value was 476 ADC/average electron and for 200keV this value was 292 ADC/average electron. The average of all the pixel values in each image was divided by the appropriate slope value to obtain an estimate for the average electron flux. These values were used to normalize the noise power spectrum at 120keV and 200keV. Unlike MTF and DQE, the results of the NPS measurement are not normalized to 1, making the interpretation of the results somewhat less intuitive. Overall behavior of the curves is the most straightforward way of understanding these results.

Results

The normalized NPS for 120keV and 200keV electrons are presented in Figure 3.16. The noise is higher for 200keV electrons than for 120keV electrons,

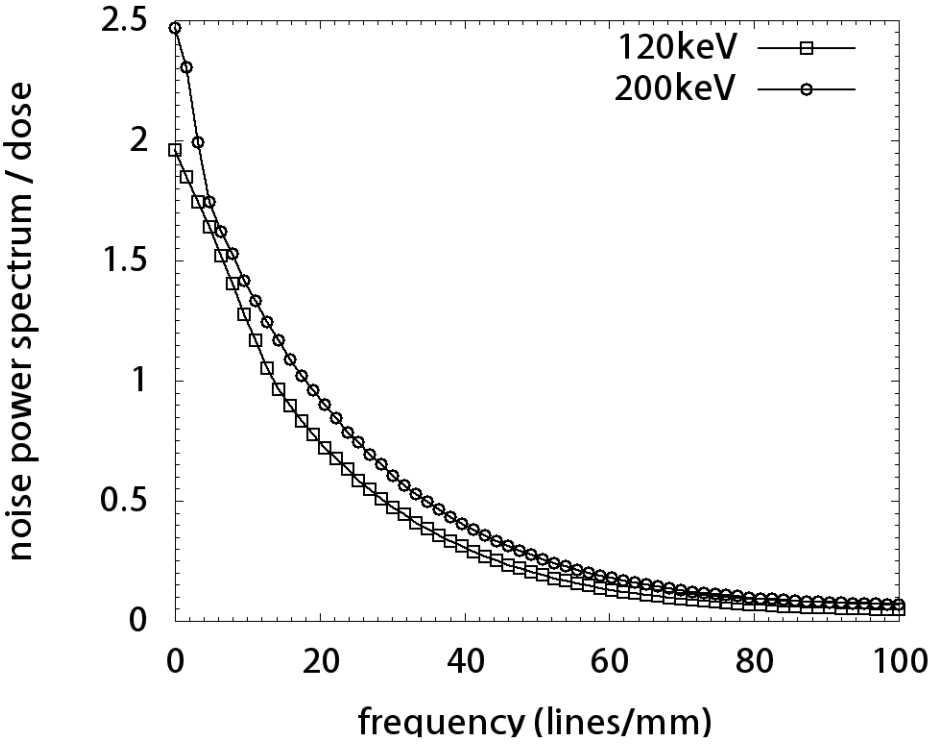

Figure 3.16: Normalized noise power spectrum plot shows the slightly higher noise values for 200keV electrons. This can be explained by the strong probabilistic Landau distribution at both energies that accounts for large variation in energy deposition in the DDD.

in particular at lower frequencies. Since these measurements were normalized for dose, there ought to not be different levels of noise due to counting statistics. These data sets were acquired on different microscopes with slightly different configurations. However, it is not clear whether these slightly different imaging conditions could affect the NPS to this degree. Possibly the best explanation for the differences in noise is the large variation of energy deposition in the DDD that follows the strong probabilistic Landau distribution for electrons at both energies. Since this measurement was performed with a low number of electrons, the fluctuations from the energy distribution and differences in scattering best explains the difference in the noise values. The other feature to point out from Figure 3.16 is higher noise for low frequencies while noise is lower at higher frequencies for 200keV compared to 120keV. The transition points for these curves are around 13 lines/mm for 120keV and 16 lines/mm for 200keV.

Normalized noise power spectrum as a function of integration time

For low dose imaging applications with radiation sensitive specimen, the duty cycle of the operation of the DDD is optimized by increasing the integration time between reads of the DDD. Any electrons striking the detector prior to the first read are not detected in the final data because of the CDS subtraction employed to reduce reset noise. Therefore it is beneficial to minimize the ratio of the number of electrons striking the detector before the first read of the chip with those striking after the first read. Thus for low dose applications, it was crucial to explore any effect changing the integration time had on the noise characteristics of the detector.

The following measurement was performed only with 120keV electrons. Eight data sets were collected for this measurement. 1005 frames were acquired for the integration times of 53, 101, 153 and 203ms with a uniform electron beam and with no beam to correct for the dark noise. The first 5 frames were excluded from the analysis. For the bright field images, the beam flux was adjusted for each different integration time so that the overall dose was similar. The normalized noise power spectrum was calculated for each data set from the average of power spectra of each image in the bright field data set and dividing by the average electron dose

per image. Figure 3.17 shows the results of the NNPS for each integration time plotted on a log scale to enhance the small differences in these curves. The overall conclusion from this plot is that integration time has a very marginal effect on the noise in the detector. Any slight effects favoring shorter integration times may be caused by the timescale with which the electrons are diffusing to neighboring pixels, but further simulation of the detector would be required to make a more definite assertion.

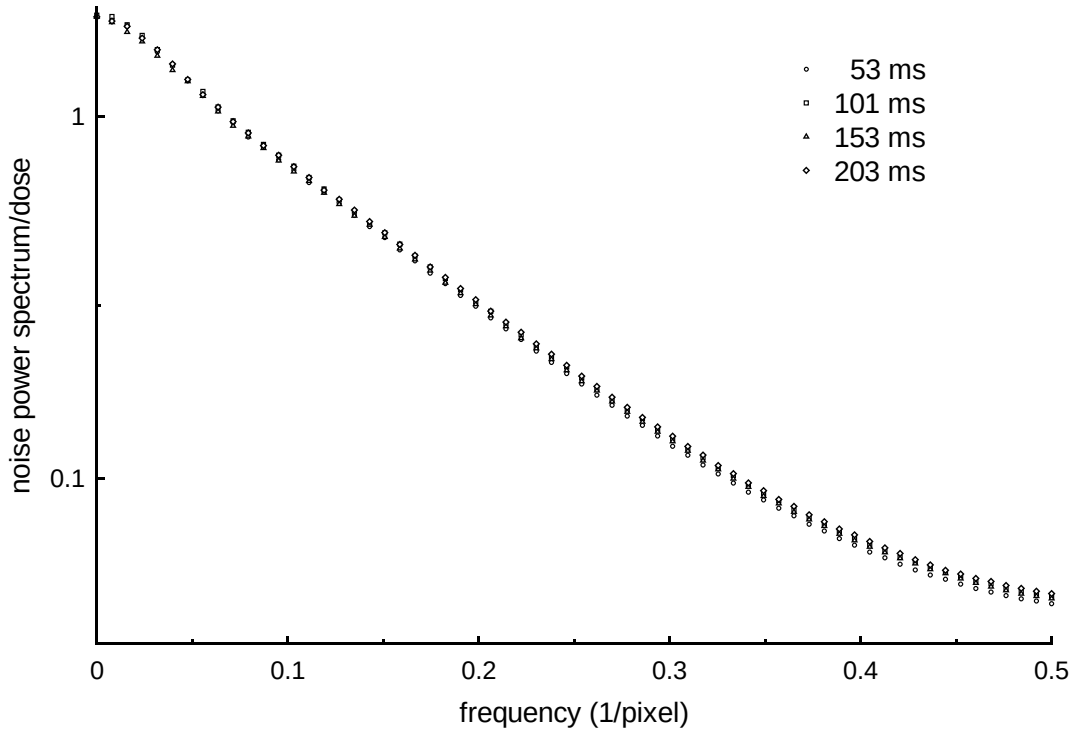

Figure 3.17: Normalized noise power spectrum as a function of integration time shows that little difference exists as the integration time is varied. Since a requirement for low dose imaging is an increase in integration time, this measurement confirmed that optimizing the duty cycle of the DDD for low dose imaging will not result in higher noise.

Although the effect of integration time on the normalized noise power spectrum is not large, the results of this measurement led to the continued practice of using 53ms integration time for imaging samples with higher radiation toler-

ance such the epoxy embedded specimen used for the imaging and tomography experiments in Chapter 4. However, the small effect on noise would not preclude using higher integration times for extremely radiation sensitive samples, such as specimen embedded in vitreous ice.

3.2.4 Detective quantum efficiency

The DQE measures the degradation of the signal to noise ratio by the imaging system at various spatial frequencies. Shown in Equation 3.3 is the precise definition of DQE. It is the ratio of the square of the measured signal-to-noise ratio of the output signal of the system to the square of the measured signal-to-noise ratio of the input signal.

$$\mathrm{DQE} = \frac{\mathrm{SNR}_{\mathrm{out}}^2}{\mathrm{SNR}_{\mathrm{in}}^2} \tag{3.3}$$

There is some controversy about the usefulness of the DQE since it is a measurement of the detector system and does not take into account the myriad post-processing techniques that can improve image quality. However, the argument can be made that it allows for comparison between disparate imaging systems provided the measurement conditions are the same. This paves the way to perform an accurate comparison between the DDD, photographic emulsion film, and CCD cameras. Although a careful comparison with photographic film and CCD cameras was not a component of this thesis research project, the measurement techniques and data analysis described in detail here could be used by other scientists to compare their detector systems with the DDD.

Analysis

The equation for determining the DQE is shown in Equation 3.4 and is derived from Equation 3.3 [1, 5]. The results from the modulation transfer function (Figure 3.15) and the noise power spectrum were used to determine the DQE. A correction for bandwidth limitations was applied by multiplying the MTF with a sinc function in the DQE calculation. Due to the MTF being so much smaller than

the bandwidth, the correction makes only a small difference, but was added for completeness [55, 52]. No aliasing correction was applied because the MTF and NPS were so poor at the Nyquist limit.

$$\mathrm{DQE} = \frac{\mathrm{MTF}^2 \times \mathrm{Dose}}{\mathrm{NPS}} \tag{3.4}$$

Results

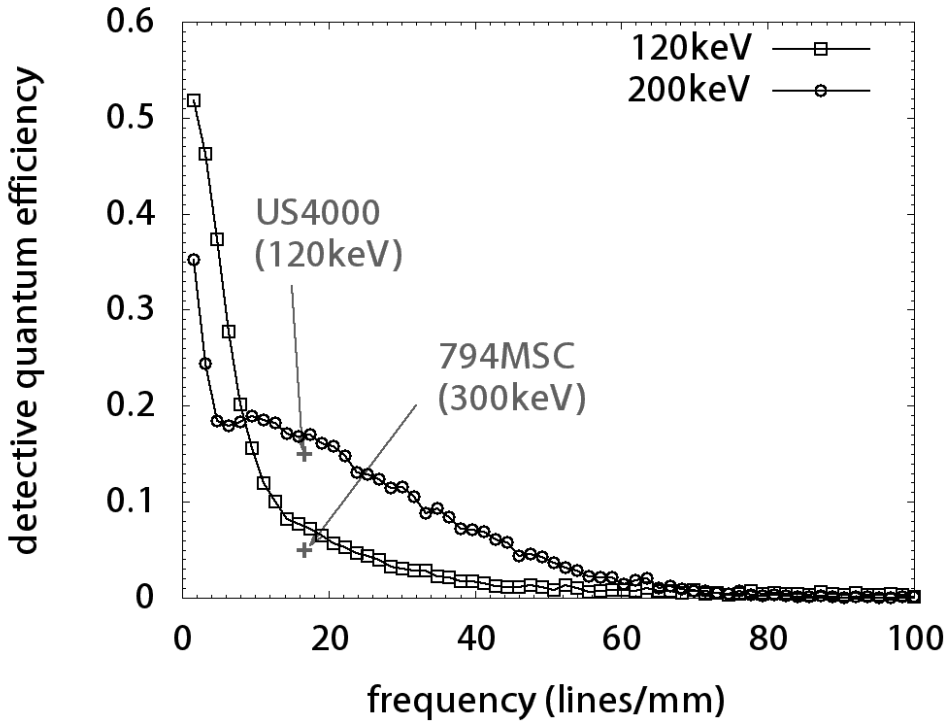

Figure 3.18: Detective quantum efficiency plot for images recorded with 120keV and 200keV electrons, compared with those of commercial cameras. Scatter points illustrate performance of commercial CCD cameras, with electron energy in brackets, Cameras US400 and 794MSC are manufactured by Gatan [31, 52].

The calculated DQE for the DDD is shown in Figure 3.18. Since the DQE depends upon the results from the MTF and NPS, features of those curves affect the resultant DQE. For example, the presence of low-frequency noise in the NPS

results causes a decrease in the DQE in the lowest frequencies to 52% at 120keV and 36% at 200keV. In addition, the strong attenuation of the MTF reduces this further to 4% for 120keV and 13% for 200keV at 25 lines/mm. The DQE drops below 5% at 22 lines/mm at 120keV and at 44 lines/mm at 200keV, to a limiting value of 0.1% at the maximum 100 lines/mm. By comparison with reported values of conventional CCDs, the DQE of DDD is much higher at high electron energies, reaching 17% at 200keV for 16.7 lines/mm compared with 5% at120keV at the same spatial frequency [52]. However, a higher DQE value has been reported for a Gatan US4000 CCD operating at a lower electron energy, i.e. 15% at 120keV and 16.7 lines/mm [31], compared with 8% obtained here for the same energy and spatial frequency. However, it is important to note that due to backscatter in the fiber optics, Gatan US4000U fiber-coupled 4k×4k camera has a much lower DQE at 200 and 300keV than at 100keV [3]. Unlike for CCD cameras, the DDD shows improved DQE with higher incident electron energies.

3.2.5 Characterization discussion

The spatial resolution estimate from Section 3.1.6 is about 5μm, the size of a DDD pixel. This is most likely an overestimate of the resolution since the point spread function based on single electron events depended upon the assumption that the highest pixel value of an event was where the incident electron entered the detector. In contrast, the more thorough analysis presented in this section with the MTF shows that the DDD has a far more limited resolution than the single electron studies suggest. The MTF indicates that much better resolution would be seen if the detector was binned by a factor of 3 or 4 for 120keV incident electrons or by a factor of 2 for 200keV incident electrons. Yet, the MTF measured with an edge often produces an underestimation of the resolution of an imaging system [52] so a cautious conclusion about the resolution estimate of the large format DDD is that it lies somewhere between the single electron estimate and the MTF measured with the edge method.

An improvement in MTF would result in an improvement in DQE. The effect of back scattered electrons was shown in the single electron studies. Thinning

the substrate down to 30μm has been suggested as a way to reduce back scattering [54]. However, previous unpublished results with the medium format DDD chip demonstrated that while back scattered electrons are significantly reduced, the MTF remains largely unchanged.

Given that the MTF and NPS of the DDD are constrained primarily by lateral scattering of high energy incident electrons, the DQE of the DDD is limited by electron scattering in silicon and is therefore representative of the ultimate performance that can be obtained with directly exposed imaging cameras. Other detection methods, such as electron counting schemes, are being pursued to obtain improved MTF and DQE with directly exposed imaging cameras [56]. However, for the large format DDD, the readout rate limits the use of the detector to a charge integration detection method.

Chapter 3, in part, has been submitted for publication of the material as it may appear in Physical Review Letters, 2009. Milazzo, Anna-Clare; Moldovan, Grigore; Lanman, Jason; Jin, Liang; Bouwer, James C.; Klienfelder, Stuart; Peltier, Steven T.; Ellisman, Mark H.; Kirkland, Angus I.; Xuong,Nguyen-Huu. American Physical Society Journals, 2009. The dissertation author was the primary investigator and author of this paper.

Chapter 4

Tomography studies with flock house virus

This chapter presents results of imaging biological specimen with the large format DDD. The relevance of the DDD as a new tool for performing detailed biological TEM imaging is clearly demonstrated. This work focused in particular on tomographic studies with epoxy embedded, thin sections of flock house virus in vivo at 120keV. In addition, the selected imaging studies show how the DDD might be used in novel ways due to the unique features of fast readout, high sensitivity and small pixel size.

This chapter has two main sections. The first section examines a multi-tilt tomogram acquired with the DDD. A full analysis of the multi-tilt tomogram is presented as it was the highest resolution tomogram of flock house virus in vivo at the time, thereby demonstrating the relevance of the DDD as a new tool for biological imaging. Also a novel application of the fast readout of the DDD for tomography data is presented. The second part of the chapter presents studies performed with stained and unstained samples using 2D imaging and tomography that provide further evidence that the large format DDD is well suited for obtaining meaningful biological information.

4.1 Background on specimen and methods

4.1.1 Flock house virus

Flock house virus, discovered in 1982, is a member of the Nodavirus family [65]. This is a well characterized virus with the structure from x-ray crystallography known to $3\mathring{A}$ and the cryo-EM structure determined to at least $8\mathring{A}$ [15]. The structure of this virus is very simple. It is composed of a protein capsid with an icosahedral structure (T=3 symmetry). Inside the capsid is a double strand of RNA that also exhibits organization into a dodecahedral cage [64]. Figure 4.1 highlights the organization of this virus through a cross sectional illustration. The diameter of the entire virus is about 30nm and the diameter of the internal RNA dodecahedral cage is 20nm.

The results presented in this chapter compare the tomography results from the DDD with cryo-EM reconstruction coordinates of flock house virus. The estimated resolution from the cryo-EM single particle reconstruction was $7.5\mathring{A}$.

Although the structure of flock house virus is well known, there is only a partial understanding of the lifecycle of the virus in a cell. Studies of flock house virus in the cell have been performed with standard cellular fixation techniques and, more recently, high pressure freezing/freeze substitution(HP/FS) methods [35, 40]. These in vivo studies have shown that the flock house virus arranges itself in paracrystalline arrays in the cytoplasm. The purpose of the viruses forming these arrays and the organization of the particles within these arrays are questions under investigation [40].

In addition, certain properties made these samples ideal for use with the DDD. First, the HPF/FS samples are of lower contrast than traditionally fixed specimen due to the high molecular preservation. Lower contrast samples are better imaged by a detector with high sensitivity, such as the DDD. Second, while somewhat more radiation sensitive than traditionally fixed specimen, the specimen used for the imaging studies with the DDD were less radiation sensitive than cryo-EM specimen. Specimen with high radiation sensitivity would require integration of the DDD with a fully automated low dose TEM data acquisition system, a

project still under development.

Therefore, due to the inherent lower contrast, radiation tolerance, and biological significance, HP/FS epoxy embedded thin sections of flock house virus in vivo, specifically the paracrystalline viral arrays formed in the cytoplasm, proved to be an ideal sample to conduct the experiments described in this chapter.

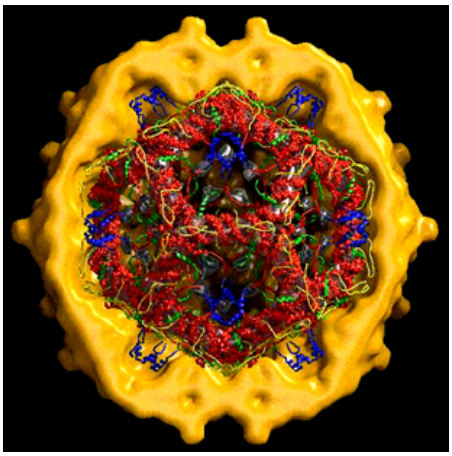

Figure 4.1: Rendering of the cross section of a flock house virus particle. The icosahedral coat protein is distinct from the dodecahedral RNA core. Image courtesy of Dr. John Johnson, The Scripps Research Institute.

4.1.2 Specimen preparation

All of the specimen preparation for these experiments was carried out by Dr. Jason Lanman of Scripps Research Institute, who specializes in flock house virus studies in infected cells. The following protocols are described in order to put the imaging results in context. In terms of evaluating the performance of the DDD for imaging biological samples, the quality of the final image depended as much on the specimen quality as on the camera system.

For samples prepared by cryofixation, Drosophila cells were infected with flock house virus at a multiplicity of infection of five. At 12 h post-infection the cells were gently removed from the plates and centrifuged at 500g for 5 min. A small sample from the resulting pellet was placed into a brass planchet (Ted Pella), 5% sucrose solution was added and centrifuged at 500g for 5min. A small sample

from the resulting pellet was rapidly frozen in a high pressure freezer (BAL-TEC HPM 010). The frozen planchets were placed into a freeze substitution device (Leica EM-AFS) at -90°C then treated with 20% of a stock resin mixture with 80% acetone. The sample was then warmed to 4°C and was infiltrated with 66% stock resin mixture for 4 h, 100% stock resin mixture for 24 h, then polymerized at 60°C for 48 h. The post embedding staining protocols are as follows. For the specimen used in Section 4.3, the specimen were stained with 5% uranyl acetate in 50% methanol and 50% double distilled water. The samples were then rinsed in double distilled water and stained with Sato's triple lead [62] for 2.5 minutes. For the specimen in Section 4.4.2, the specimen were stained with 2% uranyl acetate solution and 100% double distilled water followed by a rinse with double distilled water. For the high resolution tomogram the specimen were additionally stained with Sato's triple lead for 2.5 minutes.

4.2 Use of small gold

Finding novel ways of exploiting the small pixel size (5μm for the DDD vs 15-24μm for a CCD) is ongoing. Gold of 5 - 10nm, standard for use with CCD cameras at higher magnifications, appeared very large even at low magnifications of less than 10,000 during the earliest imaging experiments with the large format DDD. The single tilt tomography data sets presented in Section 4.4.2 were collected with 2nm gold at magnifications less than 22,000. Colloidal gold of 2nm diameter is rarely used for tomography with CCD cameras even at high magnifications (>30,000) because the gold is too difficult to see in the projections to use it for alignment of tilt series. The higher sensitivity of the DDD allows for the use of smaller gold fiducial markers for tilt series alignment.

4.3 Four tilt axis tomogram – exploiting the fast readout of the DDD

This section demonstrates that the DDD is useful for tomography of biological specimen by presenting the results of a four axis tomogram of a flock house viral array. A full analysis to extract and align the virus particles in the four tilt tomogram was performed. Also a dose fractionation study was completed as an example of how the DDD readout mechanism may be used for novel applications in tomography.

The four axis tomogram presented in this section is an extension of the work done with dual axis tomography. Dual axis tilt tomography is a widely used technique in the field of electron tomography [46]. This technique consists of taking a tilt series, rotating the specimen grid 90 degrees and then obtaining a second tilt series of images. Because it reduces the missing wedge to a missing pyramid of information in Fourier space, dual axis tomography yields more information in the final reconstruction than a single tilt series [46]. It is now an emerging technique to pursue multi-tilt tomography [51]. The main impediment for the wide spread adoption of multi-tilt tomography is the lack of reconstruction software designed specifically for handling the challenges of reconstructing 3D structure from multiple tilt series. Fortunately, UCSD has researchers developing software that processes this type of data. Some multi-tilt tomography at the NCMIR has been performed with CCD cameras. However, these experiments have had difficulties successfully collecting full data sets since specimen damage becomes an issue with the large number of images required for a multi axis tilt series. This problem is compounded by the lower sensitivity of CCD cameras. With the smaller pixel size and higher sensitivity of the DDD, multi axis tilt tomograms can be acquired with a lower chance of significant specimen damage, making the DDD an ideal choice for multi axis tilt tomography.

Finally, acquiring a multi axis tilt series data set with the DDD gave a unique opportunity to exploit the fast, multiple frame readout of the DDD and employ dose fractionation techniques. As an example of the DDD capabilities, the

difference in information from using a four axis tilt tomogram compared to using a dual axis tomogram is presented. This analysis was unique to the DDD because we can compare a dual axis tomogram with a four tilt tomogram by manipulating the data sets to contain the same amount of measured signal.

4.3.1 Experimental conditions

The specimen was prepared as described in Section 4.1.2 and was sectioned to 90nm. The staining conditions post sectioning with uranyl acetate and Sato's lead is covered in Section 4.1.2. Gold fiducial particles of approximately 5nm size were added to both top and bottom surface of the specimen grid. Hummingbird Scientific, Inc. loaned a prototype rotation holder to use for this measurement where the rotation of the grid was precisely controlled by an external stepper control box and piezo motors. A low magnification survey image of the specimen is shown in Figure 4.2 with a square annotating the approximate region used for the tilt series acquisition. This area was chosen because of the highly regular order of the viral array near an infected mitochondria and because of the presence of unidentified larger particles in the array lattice. It was unknown whether these larger particles were a contaminant or a different conformation of the flock house virus. Thus, this area was chosen to explore a non standard viral array in hopes of furthering the understanding of the flock house virus in the cell, in addition to pursuing the goal of demonstrating the practicality of the DDD as a TEM imaging system.

Four tilt series were acquired, rotating the specimen grid 45° after each data set. Each tilt series was taken in 2° increments from -58° to +58°. The recorded signal for each tilt angle image was approximately 60 electrons/pixel and the magnification was approximately 14,000. The signal collected for each tilt angle was specifically kept low for two reasons. First, due to the low dynamic range of the DDD with 120keV electrons, only around 2 electrons/pixel/frame could be collected while ensuring a linear response from the DDD. This makes it necessary to collect many frames. With a readout rate of 10 frames/second specimen, drift was likely with total recording times of more than a few seconds. Although drift

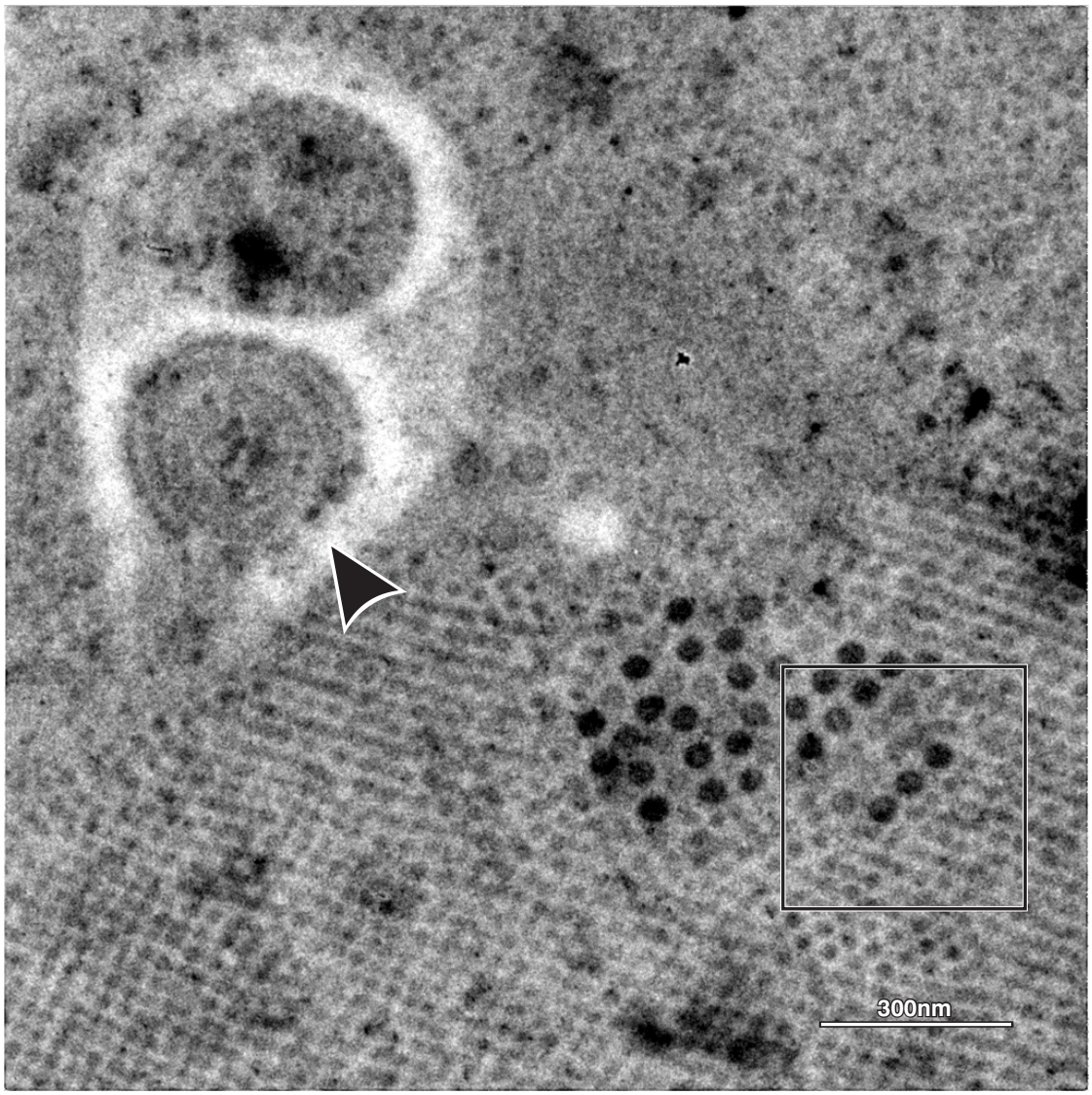

Figure 4.2: Low magnification image of the area where the tilt series was taken. Infected mitochondria is noted with an arrow. Area where tilt series was acquired is enclosed in a square. This indicated area contains part of the flock house virus paracrystalline array as well as unknown larger particles that seem to be aligned with the array.

correction of images is possible with the DDD, it works better at intermediate electron voltages (200keV and higher) since a certain amount of information has to be collected to successfully perform cross correlation alignment of the sub-images. The second reason for low signal collection was to test the detector performance for future cryo-tomography and cryo-EM single particle experiments that would require low dose.

4.3.2 Analysis of four tilt data set

Full tomographic reconstruction

The analysis of the four tilt tomogram was completed with TxBR [41, 59, 42, 58], a tomography reconstruction software suite developed at the NCMIR that is capable of processing multi axis tilt series into tomograms. Figure 4.3 shows a slice from the full volume reconstruction where the smaller flock house virus particles are lined up in the paracrystalline array with the unknown, larger particles in the center. The results show particles that have more detail and contrast than any previous tomography results with flock house virus arrays in vivo. This was also the first time a thin (90nm versus 250nm) section flock house virus array was examined through tomography at 120 keV. Since flock house virus particles are on average 30nm in diameter, at most 3 layers of particles were expected in the volume reconstruction. The diameter of the particles in the reconstruction is approximately 85 pixels. The magnification of about 14,000 sets the pixel size to about $3.5\mathring{A}$/pixel. This sets the diameter of the particles in the reconstruction to 30nm, which demonstrates that the UA/lead staining is primarily staining the viral capsid. However, some volume slices show flock house virus particles with a dark inner ring and a less dense inner core which is evidence that, in some cases, part of the RNA cage inside the virus particle is also being stained. Previous estimates given for the resolution possible from tomography of HP/FS, stained specimen was set at approximately 6nm due to the granularity of the stain after radiation exposure and by the spatial accuracy with which stain binds to the macromolecules [49]. Unlike other viruses which have distinct features to obtain spatial information estimates from, the protein coat of flock house virus does not

have any unusual features that are 6nm or larger with which to gauge whether the spatial information in the tomogram meets or exceeds this value.

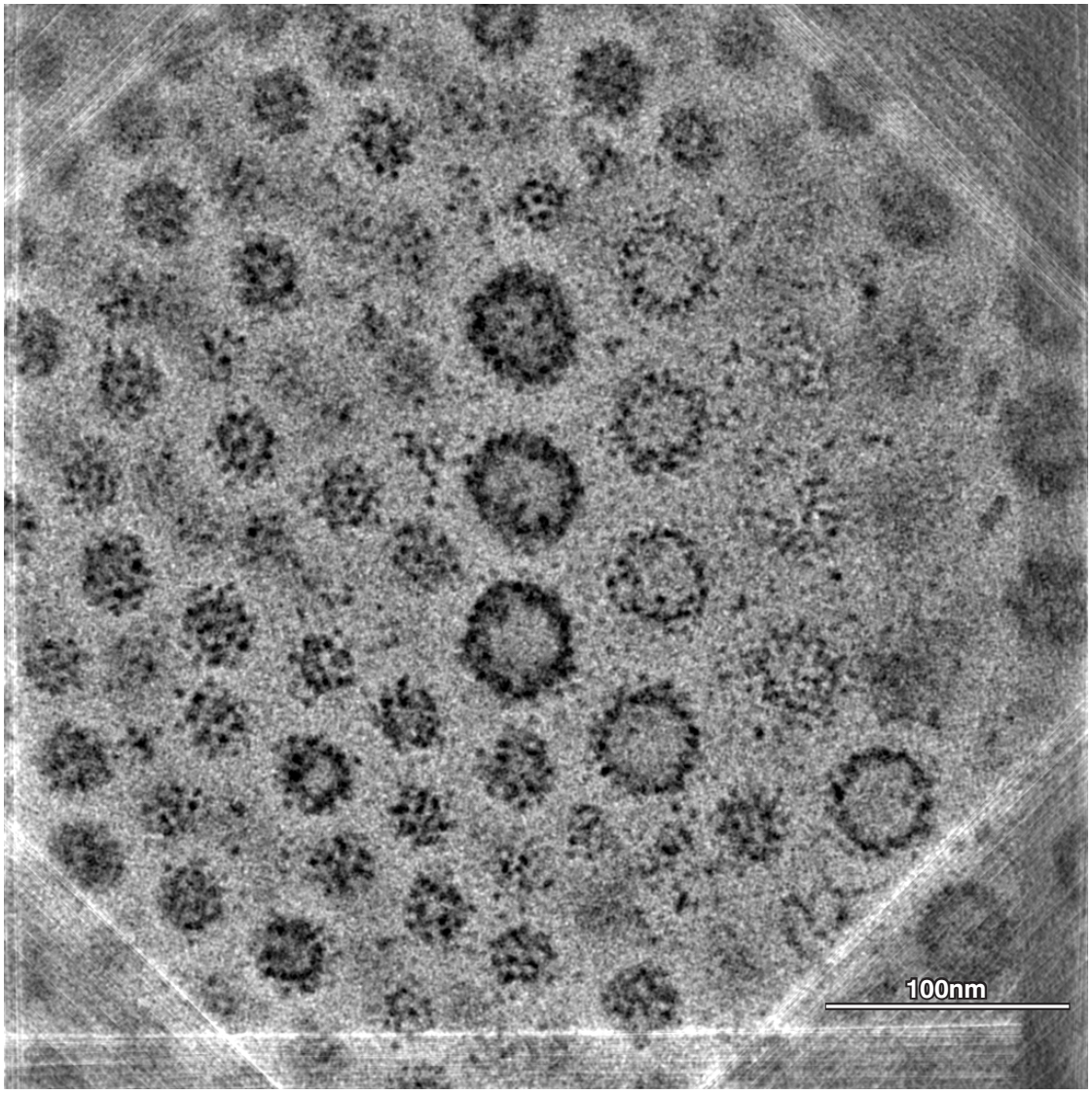

Figure 4.3: Shown is a slice from the four tilt tomographic reconstruction of a flock house virus array. Magnification was about 14,000 with a signal of approximately 60 electrons/pixel in each projection.

Extraction, alignment, and averaging of flock house virus particles

Following full volume reconstruction, further analysis of the particles in the volume reconstruction was performed. As stated above, the estimated best

resolution from a tomogram of this type of sample may be approximately 6nm due to staining conditions. Also, even with a four axis tilt tomogram to reduce the amount of missing information, there still exists missing information in Fourier space affecting the final results. One final problem is that a tomographic 3D reconstruction is somewhat noisy due to the fact that the signal to noise ratio in a tomogram is affected by the electron dose being spread out over the tilt series. However, the use of averaging sub regions in tomograms is a relatively new data processing technique that is a powerful tool in overcoming the limitations with tomography. The software for aligning and averaging sub regions is often cobbled together from single particle averaging routines, however, much research is ongoing to improve these algorithms to specifically address the features of tomography data sets, including accounting for the missing information in Fourier space [69].

The method used to average the flock house virus particles primarily uses software designed for single particle reconstruction. Fifty eight subtomograms of the flock house virus particles were extracted from the full reconstruction and normalized with the proc3d program from the EMAN software package [45]. The subtomograms were aligned relative to each other using the tomohunter program and then averaged together [63] using the EMAN avg3d program. By aligning and averaging the particles, the data available in the tomograms from the limited tilt angles and the low density of each individual particle was maximized. Figure 4.4 shows the average flock house virus particle compared with the cryo-EM single particle reconstruction that has a resolution of 7.5$\mathring{A}$. Averaging the particles does not result in a strong icosahedral shape that is known from high resolution reconstructions of the flock house virus coat protein. Instead, the averaged particle shows the expected less dense core with a protein coat with a mottled appearance. The comparison to the cryo-EM single particle reconstruction is made to illustrate how a very high resolution result would appear, but the lower resolution of the averaged particles from the tomogram is neither unexpected nor a poor result, since this was the highest resolution examination of flock house virus in vivo up to that date.

However, it is worth discussing the many reasons why a high resolution

structure was not obtainable from averaging these particles. From Figure 4.3 it is apparent that there is heterogeneity of the virus particles, in large part due to the heavy staining applied to these samples. The non uniformity of staining may produce artifacts that degrades the accuracy of the software that translationally and rotationally aligns the sub tomograms. Unlike in some specimen, where the particles are randomly oriented and not bound in place by external molecules, the fact that the flock house virus in the four tilt tomogram are in an infected cell could also add to the difficulty with resolving capsid structure on the averaged particle. Alignment and averaging of particles works best in tomography with a variety of orientations to make up for the missing Fourier space information [63]. This may not be the case in these paracrystalline arrays where the virus particles could be oriented in preferred directions.

Analysis of averaging 10 larger unknown particles did not show a known viral structure. Although these larger particles may be a different conformational state of flock house virus, subsequent examination of the flock house virus in vivo specimen shows similar looking particles in the nucleus and other locations besides the flock house viral arrays. It is well known that endogenous viruses may be triggered by trauma to a cell such as infection. Tetracystine labeling has been successfully applied to this virus and florescence microscopy studies may be useful in trying to determine how and if these larger particles are related to flock house virus [40].

4.3.3 Comparison of dual axis and four axis tomograms with the same amount of signal

Motivation behind this measurement

The fast, multiple frame readout of the DDD allows for the first time a quantitative study between the results obtained with a dual axis tilt tomogram and a four axis tilt tomogram using the same data set. A dual axis tomogram can be processed from the data set with the maximum original signal collected and a four tilt axis tomogram can be created from the same data set with half the

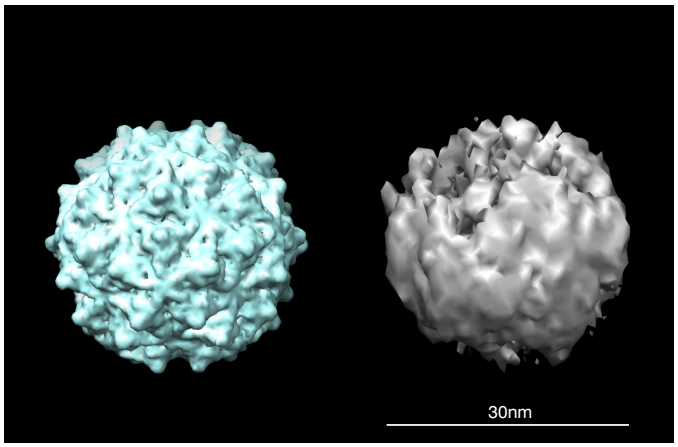

(a) Cryo-EM coordinates of flock house virus protein coat shown on left with flock house virus tomogram results on right

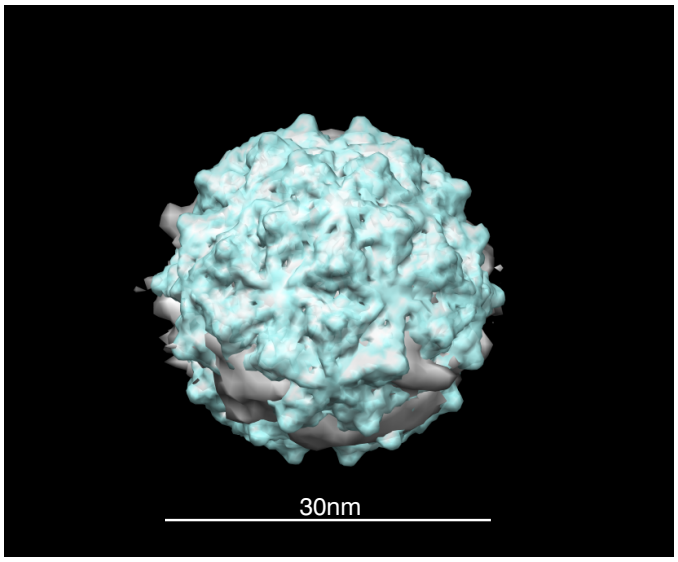

(b) Averaged flock house virus particle mapped to protein coat coordinates

Figure 4.4: Volume rendering of an average of 58 rotationally aligned flock house virus particles from four tilt tomogram is shown on right in Figure 4.4(a). Volume rendering from the coordinates from a cryo-EM, 7.5$\mathring{A}$ resolution reconstruction of the flock house virus protein coat is shown on left. Figure 4.4(b) shows the results of mapping the averaged particle into the coat protein coordinates.

original signal. The resulting tomograms have the same amount of signal in terms of electrons per pixel but may differ in the spatial information since different sets of projections were used. 3D reconstruction fidelity gains with multi-tilt tomography have been demonstrated previously [51], however that study was more qualitative and did not compare a double tilt tomogram with the same signal as in a multi-tilt tomogram due to the use of a CCD camera as the recording device.

Using the fast, multiple readout of the DDD to perform this data analysis is an example of a novel use of the DDD to quantify the spatial information gains from multi-tilt tomography. However, many other cases exist where the DDD could be used to optimize the minimum signal required for specific projections. For example, cellular membranes are not easily apparent in projections if they are perpendicular to the plane defined by the tilt axis and beam, though they are easily resolved when in other orientations [44]. The DDD could be used to optimize the minimum signal required for specific projections by selectively summing fewer frames than the total number acquired and comparing the final tomographic reconstructions. It has been demonstrated that certain resolutions can be achieved in a tomogram as the dose is fractionated amongst any number of projections [48]. Yet much remains to be understood about what sort of dose fractionation protocols would yield the highest resolution and least radiation damage for a specimen. The DDD could be used to explore these questions.

Methods and results of tomogram comparison

Every other frame was summed together for each tilt series image for the four axis tilt reconstruction data set to get a reconstruction with half the signal used in the full reconstruction. For the two axis tilt data set, every originally acquired frame was summed together for each projection. This resulted in data sets with the same amount of total measured signal, in terms of electrons per pixel. Figure 4.5 shows a side by side comparison of volume slices from these reconstructions. They have lower contrast than Figure 4.3 because they have half the signal of the full tomographic reconstruction. Examination of these two images does not result in any obvious differences between level of detail observed.

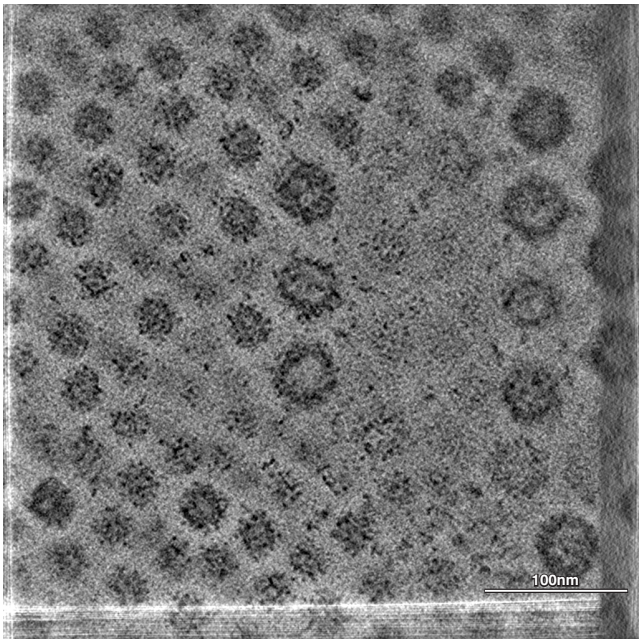

(a) Two tilt tomogram

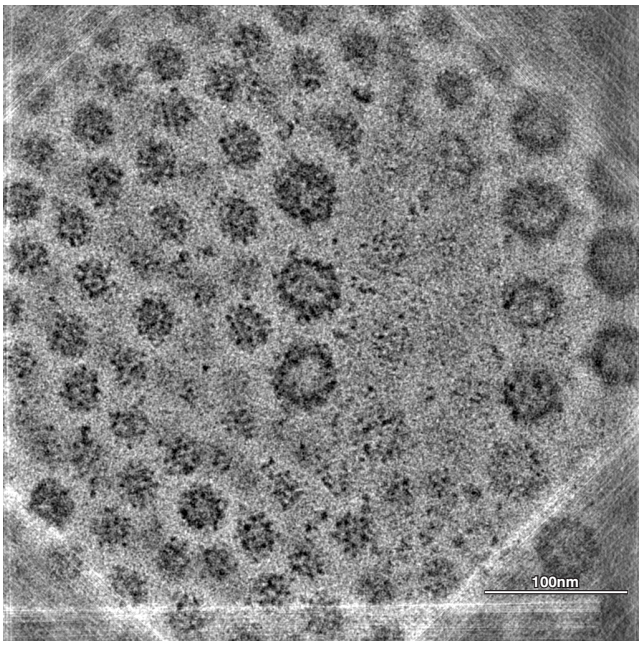

(b) Four tilt tomogram

Figure 4.5: Side by side comparison of the double tilt and four tilt tomogram volumetric slices. The same amount of total signal was used to create each reconstruction and roughly the same amount of detail is observed in each image of a volumetric slice.

The comparison between the same particle extracted from the two tomograms was a more direct measurement of the differences between a full signal dual axis tomogram and a half signal 4 tilt tomogram than attempting to use an average of a large number of particles because of the unknown errors associated with the alignment software. A particle was chosen that showed strong contrast and many features. The subtomograms extracted from the two and four tilt tomograms were 128×128 pixels in the X and Y direction and included 75 volume slices in the Z direction, centered at the same location. A 3D difference map between densities of the two subtomograms was performed and the results showed some differences between the spatial information in the two tomograms, though no features were identifiable as specific regions of the virus. To better illustrate the differences between subtomograms, they were then averaged in the Z direction resulting in 2D images shown in Figure 4.6(a) and Figure 4.6(b). Subtle differences are seen between the two images though no particular features stand out. The four tilt flock house virus particle image was subtracted from the two tilt flock house virus particle image resulting in Figure 4.6(c) which confirms the minor differences between the averaged images of the same particle.

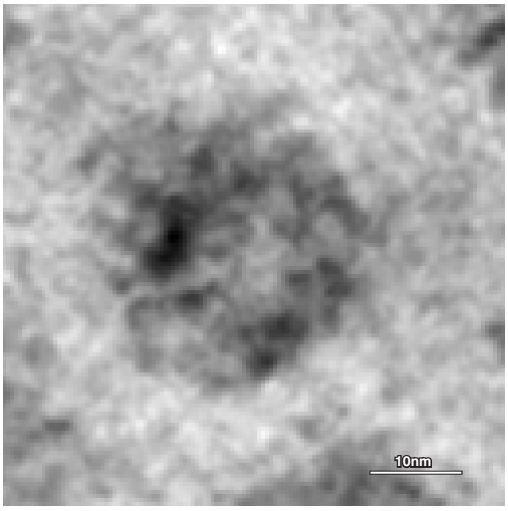

(a) Virus particle from two tilt tomogram

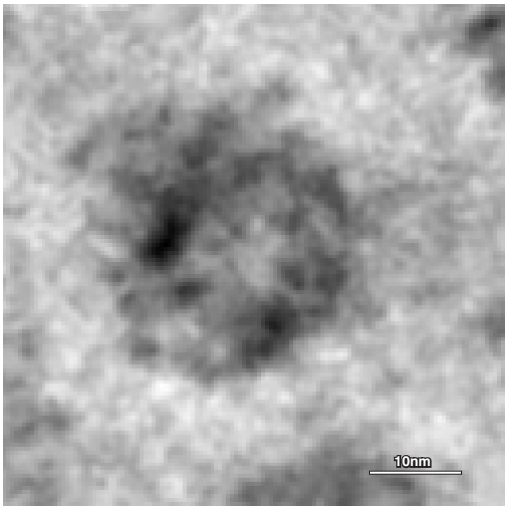

(b) Virus particle from four tilt tomogram

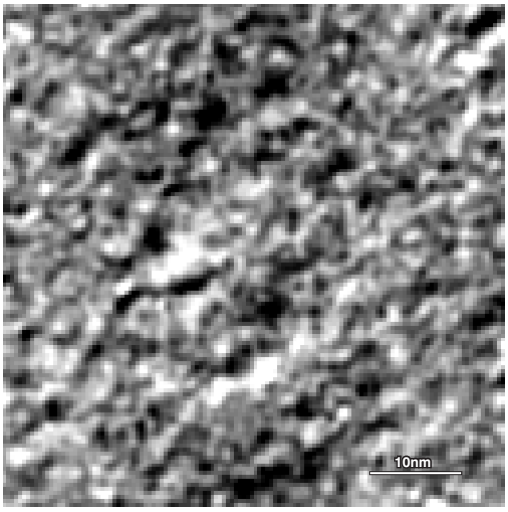

(c) Difference between four tilt and two tilt images

Figure 4.6: Same particle shown from two tilt and four tilt tomograms, averaged in the Z direction as well as the results of subtracting the two images. Subtle differences are apparent. However, these differences are not enough to confirm substantial improvement from a four tilt tomogram from this particular data set.

Discussion

The results of this measurement do not confirm that a four tilt tomogram gives substantial improvement in spatial information over a two tilt tomogram. However, irrespectively of the results, the measurement serves as a good demon-

stration of how the DDD may be used to test dose fractionation schemes. While the results are not conclusive, the experiment will be attempted in the future with a different specimen, with higher signal per tilt angle so that a comparison of identical structures in the final reconstruction can be performed with more precision. This first attempt proved to be a valuable experience for refining experimental protocol. The ability to optimize experimental conditions for tomography by examining selected subsets of the individually recorded frames is a feature of the DDD that will surely be exploited in the future.

4.4 Staining studies – exploration of the high sensitivity of the DDD

While performing conventional TEM studies on biological samples in plastic, usually some sort of contrast enhancement is needed to resolve structures due to the low density differences between the fixative and biological macromolecules of interest [9]. The results of the single electron studies in Section 3.1.6 showed the high sensitivity of the DDD. The practical limits of the sensitivity of the DDD with biological specimen were explored by imaging samples that had no stain at all, as well as performing tomography using different staining conditions.

This section describes the early exploration of imaging unstained specimen with the DDD and a measurement to qualitatively compare the results of imaging a specimen under the same conditions with a CCD camera as the large format DDD. The results of three single tilt tomography studies of flock house virus arrays are also presented with different staining conditions, demonstrating the usefulness of the large format DDD for obtaining information about biological macromolecules.

4.4.1 Unstained flock house virus specimen

Early unstained images

Due to the difficulty of finding viral arrays without the presence of stain, viral arrays were labeled with 2nm gold attached to antibodies to the virus to help

us locate the region of interest. Figure 4.7 shows two images at 8.3k magnification of the same region at the edge of a viral array at different defocus values. These images represent the best obtained after multiple attempts showing that the antibody labeled samples proved to be difficult to image, apparent by the blurriness and little detail in Figure 4.7. All the factors that could impact the image quality were carefully checked and it was shown that image quality was not degraded for other standard samples. The scattering of the electrons off the proteins associated with the gold antibody complex was the most reasonable explanation for the image quality degradation. Thus gold antibody labeling was abandoned in favor of putting 2nm gold randomly on the surface of the specimen for imaging of specimen with little or no stain. Gold antibody labeling may be attempted again in the future by changing the specimen preparation protocol to include a different washing procedure to remove the extraneous protein from the surface of the samples.

Though technically difficult to find areas of interest in the cell without the presence of stain, some areas with flock house viral arrays were finally found. The results of imaging this area were quite striking as shown in Figure 4.8 that shows a flock house virus array taken at 8.3k magnification with a dose of 600 electrons/pixel and slightly under focused. The images from the unstained samples had fairly high contrast with a low dose to the sample of $\approx$34 electrons/$\mathring{A}^2$. By way of comparison, the maximum dose for cryo-EM is usually about 25 electrons/$\mathring{A}^2$. The degree of contrast in this unstained specimen was high enough to motivate us to attempt tomography of unstained samples. Though a standard practice in cryo-tomography, unstained tomography results are rarely reported for epoxy embedded specimen in the literature.

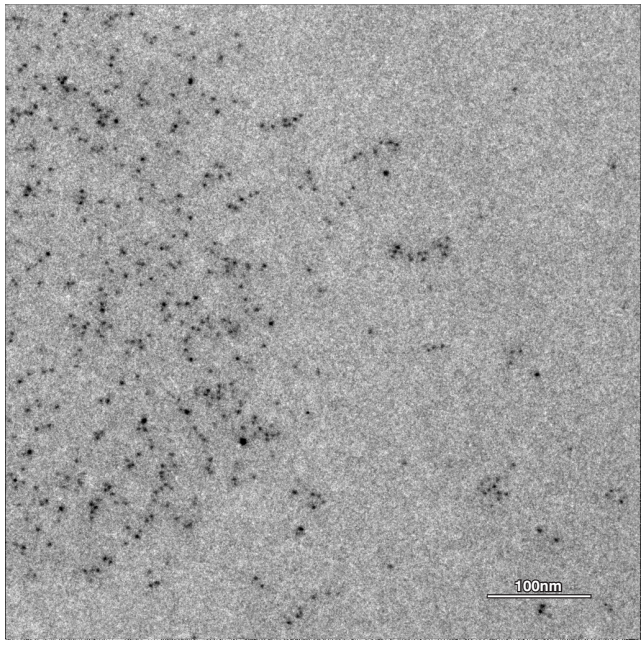

(a) 0 micron defocus

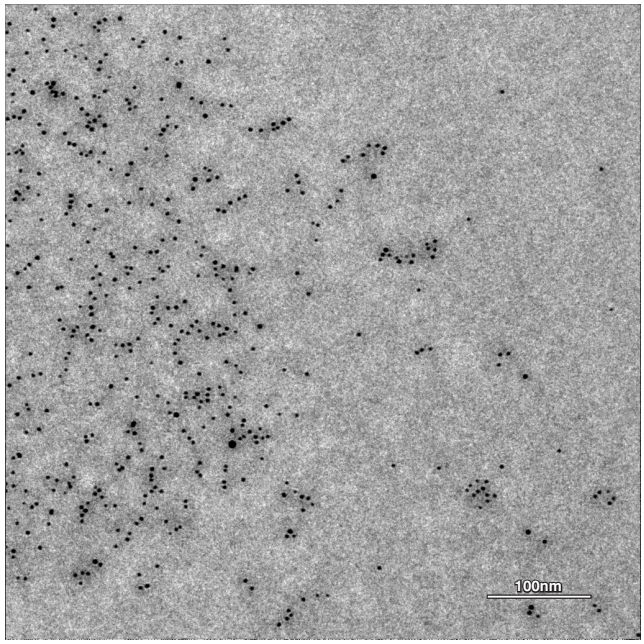

(b) 6 micron defocus

Figure 4.7: 2nm gold antibody labeled unstained flock house viral arrays

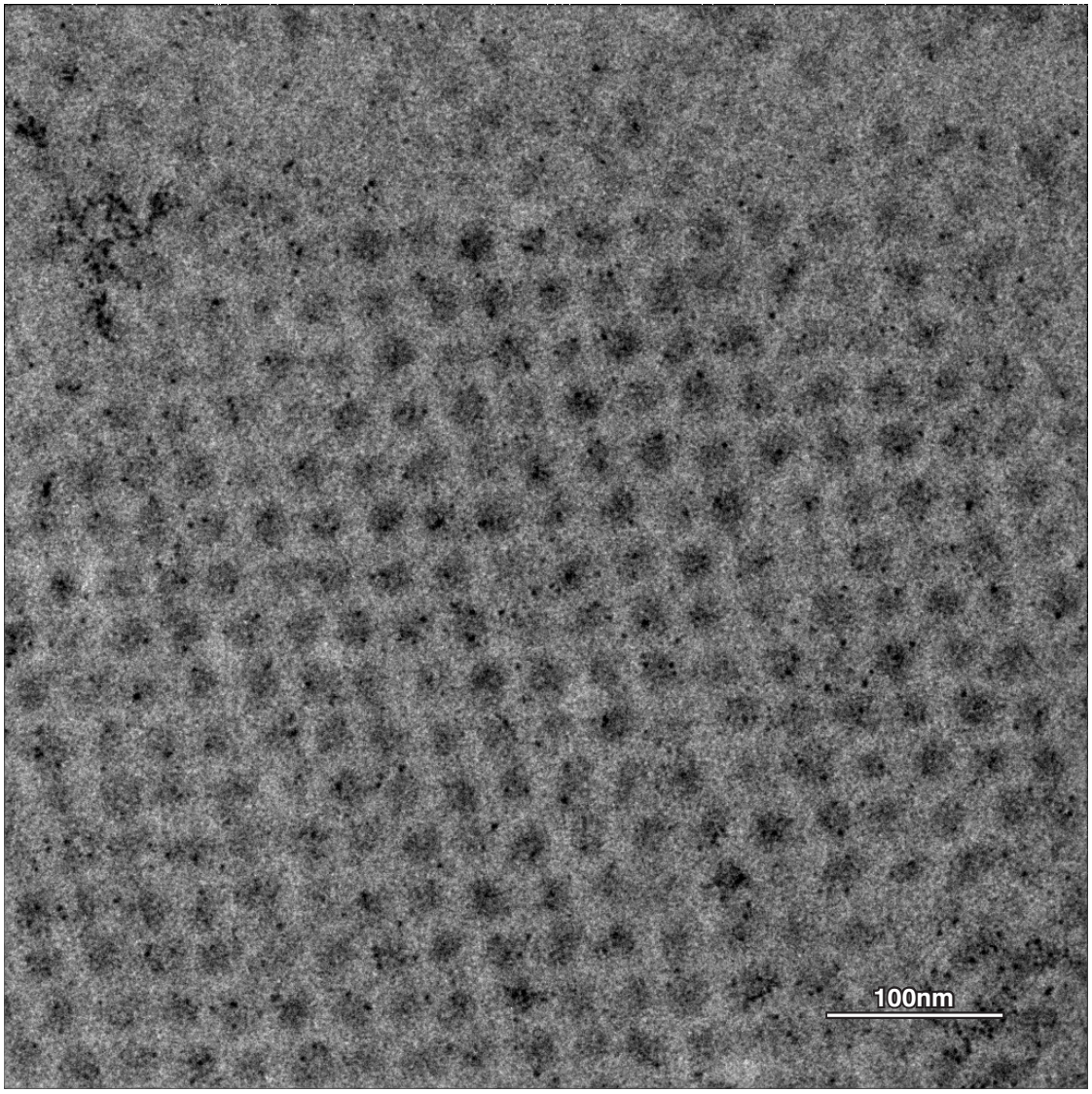

Figure 4.8: Image of unstained flock house viral array taken at 8.3k magnification with approximately 600 electrons/pixel total measured signal. 2nm gold fiducial particles can be seen scattered about the sample

DDD and CCD camera comparison

After the initial success of imaging unstained samples with the DDD, an attempt was made to produce a direct comparison between an image of an unstained sample taken with a very high quality commercial CCD camera and an image from the DDD. This experiment was devised to image the same area of a sample with the same electron flux per pixel and at the same relative magnification.

The specimen of flock house virus in vivo was prepared as described in Section 4.1.2 and no stain was applied. The experiment was performed on an FEI Spirit using a 120keV electron beam. A Tietz model F415SP CCD camera with a 4k×4k pixel array was chosen for the measurement as it is considered one of the best commercial CCD cameras at the NCMIR. The Tietz CCD camera was operated at the highest gain setting to ensure the best response with low signal.

The CCD camera was mounted below the DDD with an adapter flange. Since the DDD was not retractable, it had to be physically removed from the microscope to allow for imaging with the CCD. A small post magnification difference was present with the CCD camera since it was on a lower imaging plane than the DDD. This resulted in a minor higher magnification of the specimen in the CCD images than those acquired with the DDD. With the design of the adapter flange, the CCD imaging surface was parallel to but also slightly rotated with respect to the DDD chip.

Accurately measuring electron dose was necessary to ensure the same signal in the images taken with the DDD and the CCD camera. Since the DDD and corresponding Faraday plate had to be removed to image with the CCD camera, a calibration was performed to find the linear relationship between the Faraday plate beam flux readings and the FEI Spirit dose detection system. This calibration required focusing an electron beam of a certain diameter on the phosphorescent scintillation screen and noting the microscope flux reading. Lifting the screen, the corresponding Faraday plate value was recorded.

With the Tietz CCD camera, a series of images were acquired with different beam intensities in order to obtain images at a variety of doses while the exposure length of 2s was held constant. The magnification at the film plane of the Spirit was 30k, translating to approximately 45k magnification at the imaging plane of the CCD camera. The beam flux was varied instead of the exposure time to mitigate the effect of specimen drift on the images because the chance of specimen drift increases with exposure time. Several flock house virus arrays were imaged using this procedure since finding the exact same area to image with the DDD was challenging.

Following the image acquisitions with the CCD camera, the DDD was re-installed on the TEM. After a search, a particular area that was imaged with the CCD camera was found. At a magnification at the film plane of the Spirit of 10k (approximately 15k at the imaging plane of the DDD), 300 frames were acquired at an integration time of 53ms with a dose of approximately 2 electrons/pixel/frame. Subsets of these 300 frames were summed to obtain images representing the same doses taken with the CCD camera. Both the images from the CCD camera and DDD were corrected for dark noise and pixel gain variation with no further correction.

The CCD and DDD camera images both had to be processed further to enhance contrast because the specimen was unstained and the measured average number of electrons was fairly low. The histograms of the images were close to a normal distribution so that truncating the signal on either side of the mean of each image to 3.3σ and binning to an 8-bit image was decided as a way to enhance contrast enough to visually compare the images while retaining 99.9% of the signal. Since the CCD camera had 4k×4k pixels, an area of similar pixel dimensions to the DDD was cropped out for the comparison. A difference map between the images yielded limited information after scaling and correcting for alignment suitable for confirming qualitative differences. Full quantitative conclusions could not be drawn from the difference map due to the slightly greater magnification of the CCD camera and that the CCD camera was slightly rotated with respect to the DDD.

Figure 4.9 shows the side by side comparison of imaging for about 66 electrons/pixel. As mentioned before, counting statistics give an error of approximately 8 electrons/pixel or 12% to this signal estimate. This variation in signal contributed in large part to the noisiness of these images. Due to the low contrast of the specimen and the low number of electrons measured, the images do not differ greatly except in the fact that the gold fiducial particles stand out much more clearly in the CCD camera image. The difference in appearance of gold particles is explained by the fact that the DDD image is slightly closer to true focus than the CCD camera image. Contrast is enhanced when the image is farther from true focus because Fresnel fringes enhance contrast on either side of true focus, where

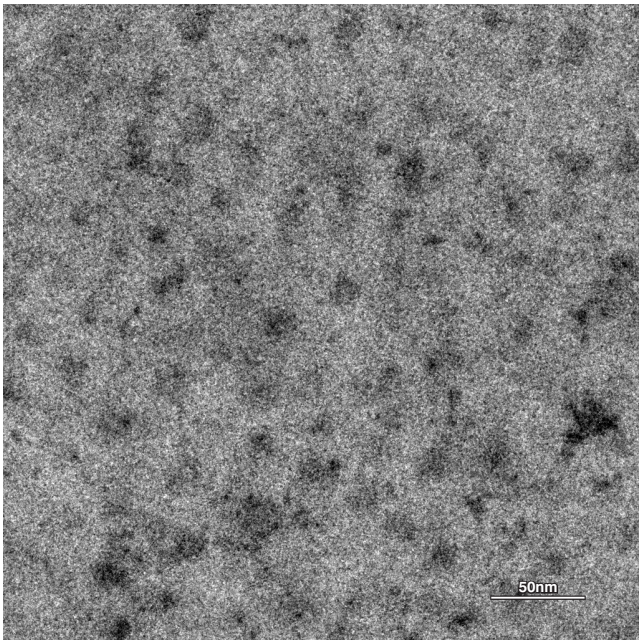

(a) DDD 15k magnification

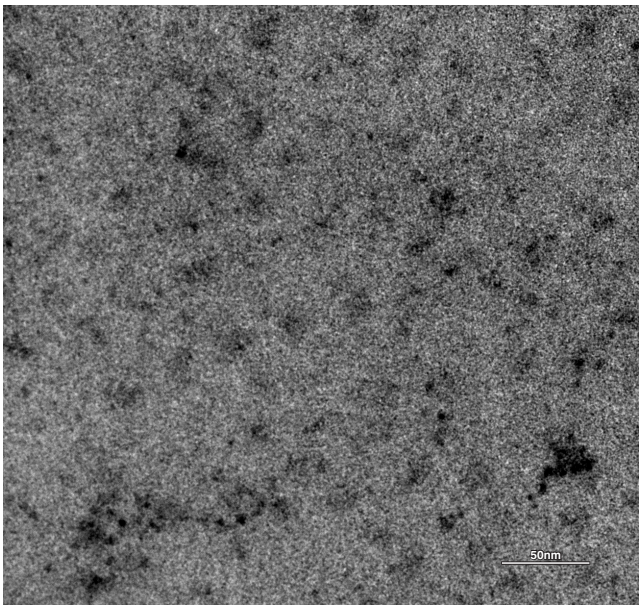

(b) CCD 45k magnification

Figure 4.9: Unstained flock house virus array 2D images with approximately 66 electrons/pixel signal for both the CCD and DDD images that are at approximately the same relative magnification. Little difference is seen between the two images due to the high statistical fluctuation of signal associated with the low number of electrons. The 2nm gold particles stand out much better in the CCD image because the image was acquired at a slightly greater defocus.

maximum contrast occurs in an under focus condition. This is confirmed in Figure 4.10 where the Fourier transforms of the two images are compared and the smaller brighter circle for the CCD image indicates greater defocus that is likely close to the maximum contrast condition.

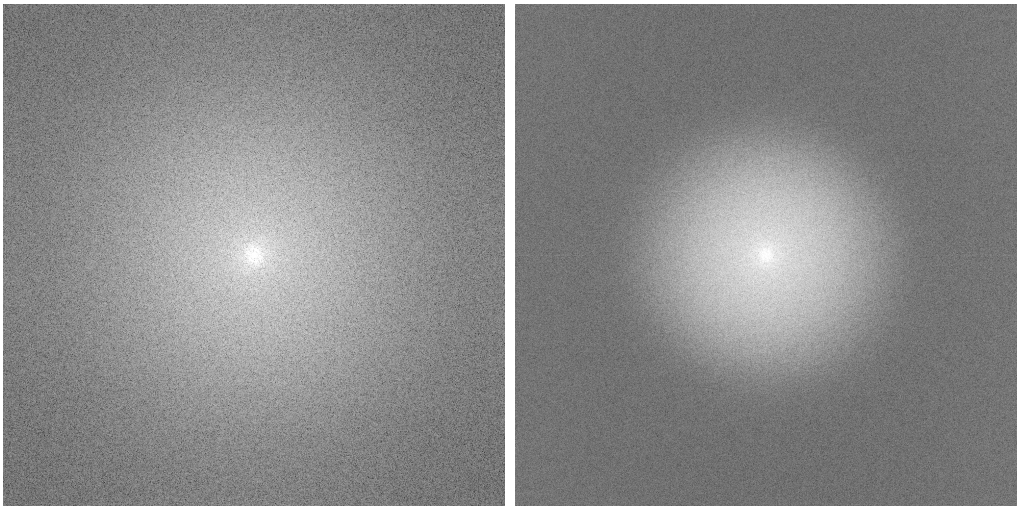

(a) Fourier transform of the DDD image shown in Figure 4.9(a)

(b) Fourier transform of the CCD image shown in Figure 4.9(b)

Figure 4.10: Fourier transforms of the images shown in Figure 4.9 with a measured beam flux of 66 electrons/pixel. These Fourier transforms show that the CCD image was slightly more defocused compared to the DDD image. The greater defocus enhanced contrast and made the 2nm gold fiducial particles appear more prominent.

The results with a higher number of electrons used to generate the images were more informative. The DDD image with 316 electrons/pixel in Figure 4.11 shows more detail than the CCD image and annotation indicates particular areas where more information is seen. A rough alignment and image subtraction confirmed that the DDD image had more information, demonstrating the higher sensitivity of the DDD. This is especially striking given that the DDD image was closer to true focus than the CCD image, resulting in lower contrast in the DDD image.

Comparison of the sets of images acquired at two different signal collection levels (66 and 316 electrons/pixel) showed that the number of electrons detected

in the images effects the amount of observed detail. Since the statistical fluctuation of measured signal was ±12% with 66 electrons/pixel and ±6% with 316 electrons/pixel signal, this experiment revealed an estimate for a threshold signal level where the higher sensitivity of the DDD became evident.

The improved detail observed in the image with the DDD compared to the CCD camera image at the higher electron flux must be qualified by a discussion of the shortcomings to this measurement. The first limitation was that the DDD had to be inserted after the CCD image was taken, requiring a complete venting of the lower portion of the microscope vacuum chamber and removal of the specimen rod with the specimen. During this process, the specimen could have been disturbed in some way. For example, some grid deformation was possible or dust could have landed on the specimen grid when out of vacuum. Furthermore, some specimen damage resulting in resin shrinkage or deformation could have occurred during the time it took to find the exact same area to image. An ideal comparison measurement would require a retractable DDD so that the comparison imaging could be done with limited variability of experimental conditions. This would also facilitate taking the images at closer to the same defocus value. Although any change in the outcome of these results would likely be a minor difference.

The other point to address is that the DDD and CCD cameras are very different imaging systems and comparisons are of limited use although this comparison may be of interest as direct detection cameras become commercially available. They are tools that have a set of different limitations and strengths and the purpose of this thesis is not to promote one over the other. However this comparison may aid researchers in deciding which system is most appropriate for an imaging study. The final conclusion from these comparison images is that certainly the DDD is no worse in providing information about biological specimen than a high quality CCD camera and may even provide more information. This is strong evidence that the DDD is useful for performing experiments with biological specimen. This measurement also complemented the single electron studies in Section 3.1.6 by using a biological specimen to test the expected higher sensitivity of the DDD and provided an example of how the 17:1 signal to noise ratio at 120keV translates

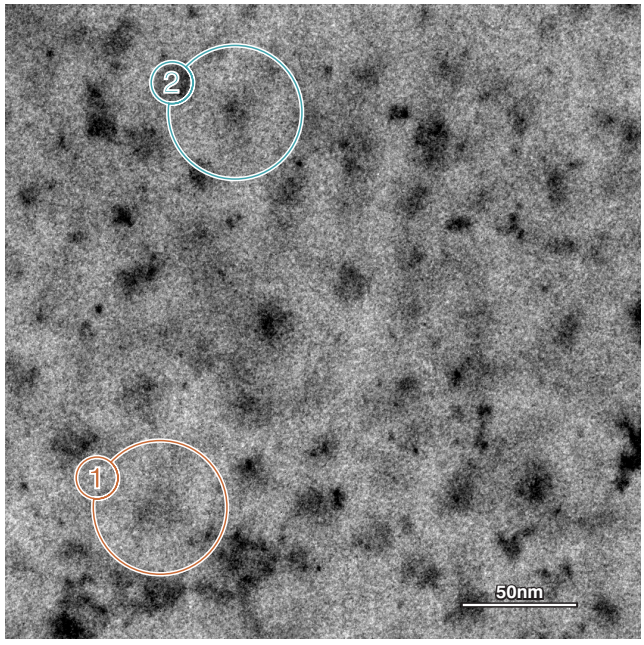

(a) DDD 15k magnification

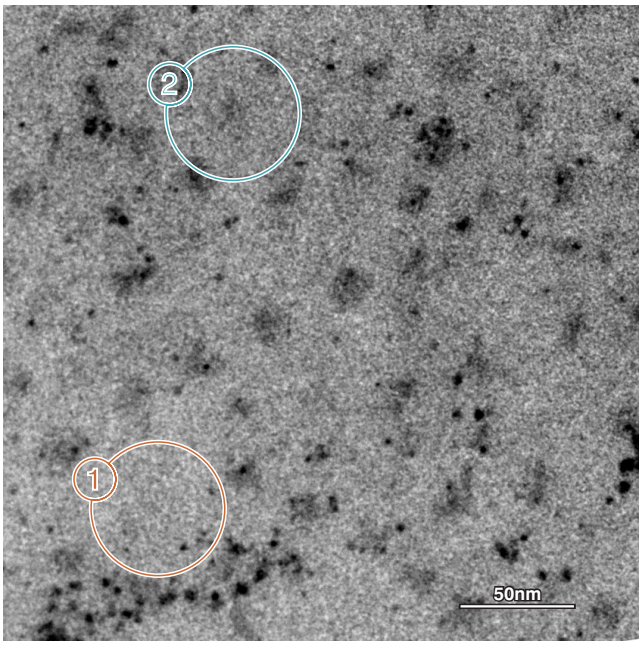

(b) CCD 45k magnification

Figure 4.11: Unstained specimen DDD and CCD comparison with 316 electrons/pixel. Areas with more detail in the DDD image, possibly virus particles, are annotated. Other areas in the DDD image seem to have enhanced detail as well.

to imaging results.

4.4.2 Tomography of flock house virus arrays under different staining conditions

This section describes three single tilt series acquired with the DDD of flock house viral arrays using different staining conditions. We hypothesized that certain staining conditions might preferentially bind to the more feature rich dodecahedral RNA cage. This was a structural component of the virus that was not clearly seen in other tomography studies of this specimen. Thus observing the RNA cage would provide further evidence that the large format DDD is useful for gathering meaningful information about biological specimen. Also, tomography of an unstained specimen was attempted because of the success with the unstained 2D imaging presented in Section 4.4.1.

Staining has been an invaluable technique for the use of TEM to determine features in biological specimen. However, staining artifacts remain an issue for high resolution work. As mentioned previously, the flock house virus specimen thin sections have fairly low contrast and the staining conditions chosen also had relatively low contrast. Extracting information about the flock house viral arrays under these conditions with the DDD gave more evidence that the DDD is a useful tool for TEM imaging.

Uranyl acetate (UA) and lead stains are considered general stains because of their broad affinity to stain many different biological macromolecules and cellular components. These heavy metal salts (UA molecular weight = 422 and lead citrate molecular weight = 1054) attach to the macromolecules, increasing their density. Beam electrons passing through the specimen are then elastically scattered through a wide angle and an increased amplitude contrast in the image results. Bozzola points out that the exact mechanism behind staining affinities remains somewhat of a mystery, although it is known that there exists high reactivity between uranyl ions and phosphate and amino groups enhancing the staining of nucleic acids and certain proteins. Lead ions have an affinity to hydroxyl groups and osmium affected areas since lead ions tend to bind to negatively charged groups [9].

The specimen for these different studies were only stained or not stained once, though they were cut from adjacent slices of a block in order to ensure that the quality of the specimen would be similar. Staining only once was chosen to limit the radiation exposure to the specimen. Although an iterative staining method would be useful for other studies. One way to go about testing different stains would be to image a specimen after a staining. This would involve treating the specimen with different staining protocols and imaging the same area after application of a new stain to compare the difference.

Tomography of uranyl acetate stained specimen

The purpose of performing tomography on a section stained only with uranyl acetate was to image the dodecahedral RNA core since uranyl acetate enhances the stain of nucleic acids. This staining protocol resulted in specimen with very low contrast, making it ideal for a high sensitivity camera. Furthermore, the featured structure of the RNA cage made it of interest since the protein coat of flock house virus is fairly uniform and does not have the features such as spikes or protrusions that other viruses contain.

This single axis tilt series was acquired with a measured signal of about 100 electrons/pixel per projection and taken from $\pm 70^\circ$ in 1° increments, though the projections at -70° and -69° were not used in the final reconstruction due to difficulty with alignment. The exposure time for each tilt angle image was approximately 5 seconds and the magnification at the detector imaging plane was approximately 14500 times ($3.44\mathring{A}$/pixel).

Figure 4.12 shows a slice from the volume reconstruction. The particles on average have a diameter of 20nm. The four axis tilt tomogram in Section 4.3 showed virus particles with a 30nm diameter. This is consistent with primarily staining the RNA cage of the flock house virus particles. A lot of rich features are present in the images of the virus particles including dark rings, mostly light cores, and dark lines criss-crossing the virus which would match the pattern of the dodecahedral cage.

Because of the large amount of information apparent in the volume re-

construction, subtomograms were selected, aligned, and averaged as described in Section 4.3.2. Figure 4.13 shows the RNA cage from a 7.5$\mathring{A}$ cryo-EM 3D reconstruction compared to the average of 25 particles from this single tilt tomogram. Although the information from this tomogram was not at a high enough resolution to fully resolve the cage structure to the same degree as the cryo-EM reconstruction, the averaged flock house virus particle shows much more of a cage like structure than the averaged particle in the four tilt tomogram in Section 4.3.2. Figure 4.4 revealed the structure of the protein coat as a more uniform, spherical density. This was not due to the larger number of particles used in the four tilt tomography analysis since an average of 25 of them showed roughly the same general features as averaging 58. Some elongation of the uranyl acetate only stained particles in Figure 4.13 is due to the missing wedge of information that results from a single tilt tomogram.

An even more tantalizing preliminary result is shown in Figure 4.14. Here the same subtomograms were averaged with no rotational alignment, only center of mass alignment. If the particles were randomly oriented in the paracrystalline arrays a uniform density would be observed. Figure 4.14 shows that the averaged particle without rotational alignment has a cage like structure suggesting that the high degree of organization of the virus particles into these paracrystalline arrays may extend to the orientation of the particles themselves. These exciting preliminary data adds to the evidence that the DDD is useful for performing tomography. This system has been successfully utilized for adding important information to the understanding of flock house virus infection in vivo.

Tomography of unstained specimen

A single axis tilt series was acquired with an unstained specimen from $\pm 70^\circ$ in 2° increments. The average signal for each image in the tilt series was approximately 100 electrons/pixel. The magnification was approximately 14500 times (3.44$\mathring{A}$/pixel). The tomogram was processed both with projections from $\pm 70^\circ$ and $\pm 60^\circ$ without any visible difference in results. A volumetric slice through this tomogram in Figure 4.15 shows very little contrast and detail, though a slice was

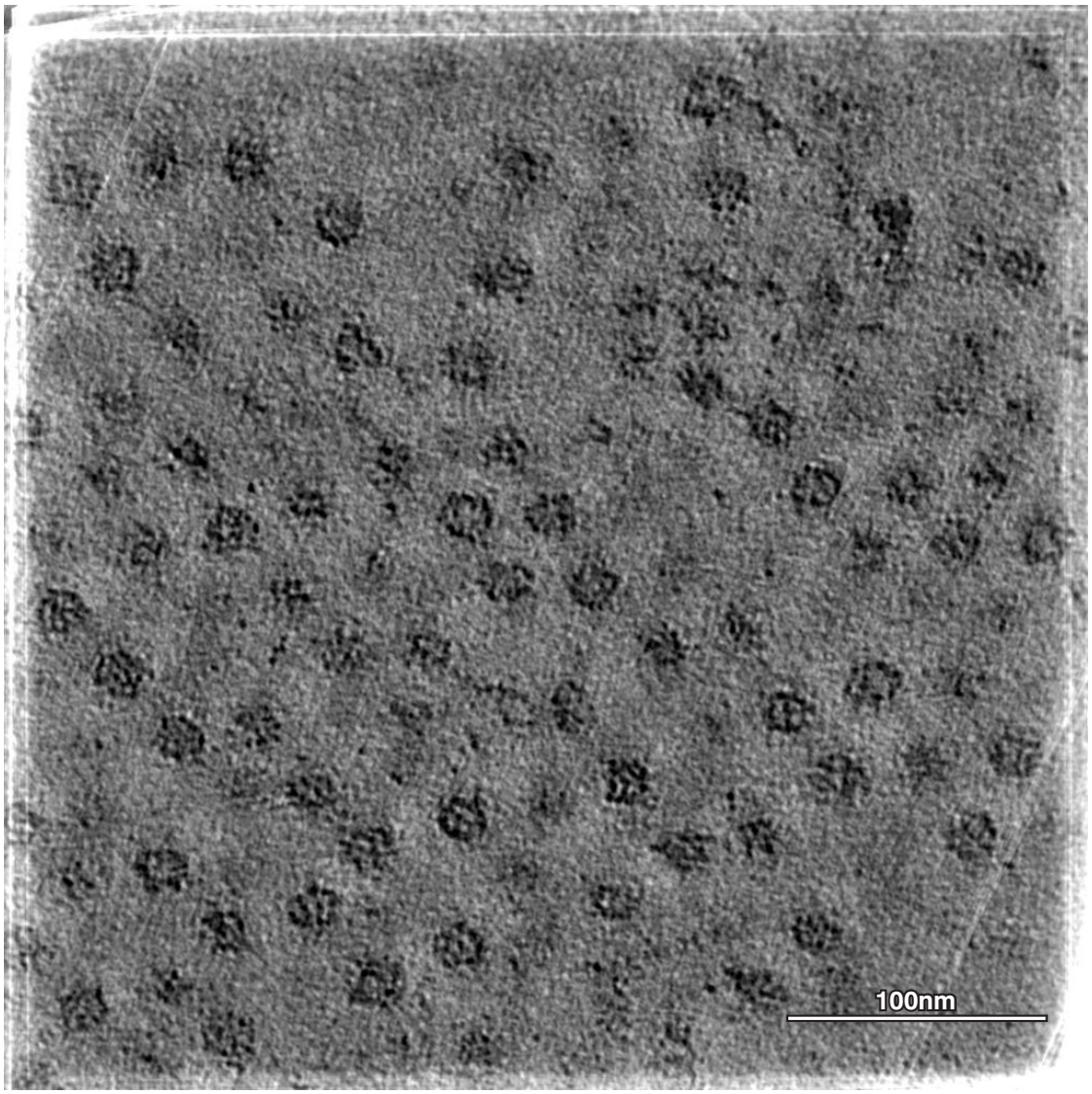

Figure 4.12: Slice from tomographic reconstruction of flock house viral array stained only with uranyl acetate. Particles are about 20nm in diameter and the features of dark rings with some criss-crossing structure suggest stain is primarily binding to RNA dodecahedral cage.

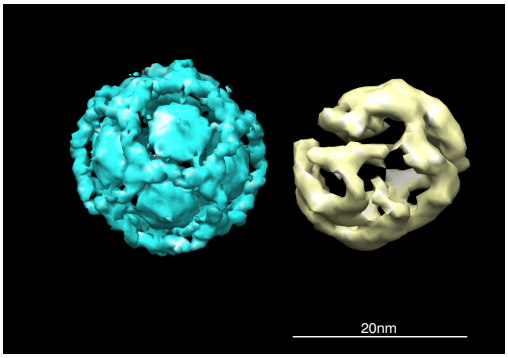

(a)

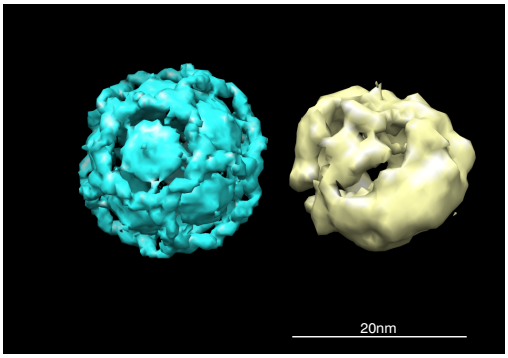

(b)

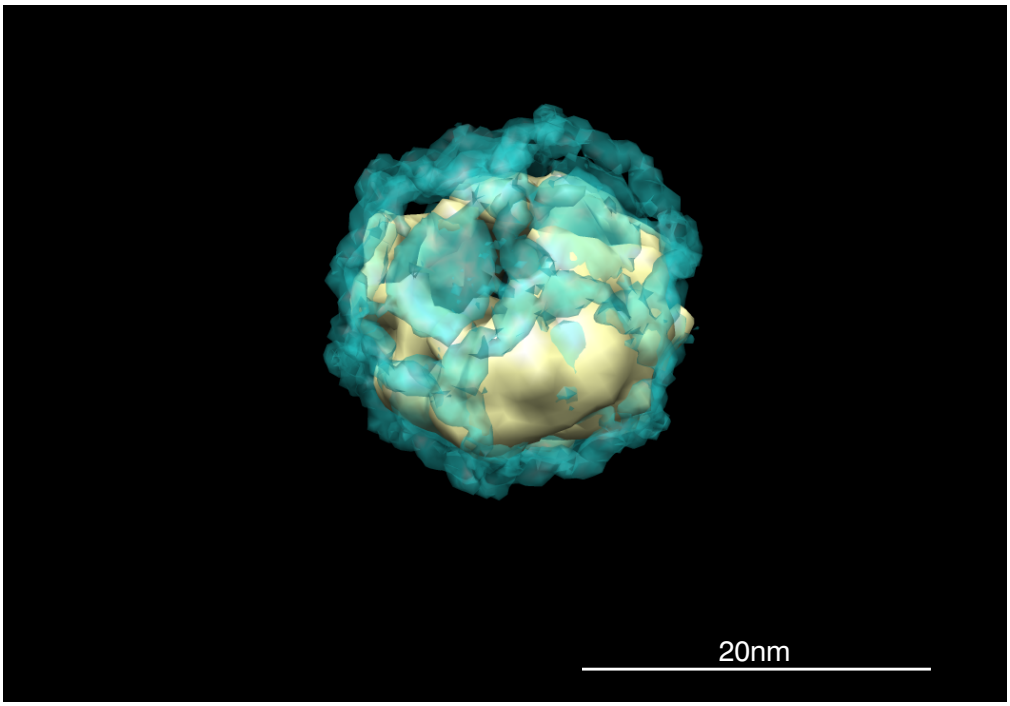

(c) Average particle fit inside a translucent RNA cage

Figure 4.13: Cryo-EM RNA cage structure with uranyl acetate stained averaged particle. Figure 4.13(a) and Figure 4.13(b) both show the cryo-EM (7.5$\mathring{A}$ resolution) coordinates of the RNA cage on the left and the averaged particle with rotational alignment on the right from different viewing angles. Figure 4.13(c) shows the best fit of mapping the average particle into the cryo-EM reconstruction.

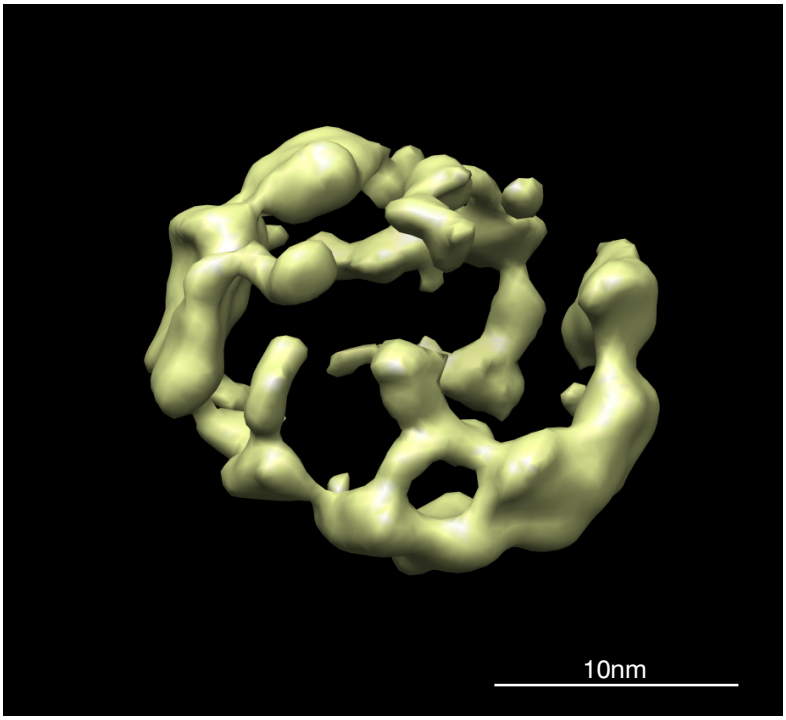

Figure 4.14: This image shows the result of averaging 25 virus particles with only a center of mass alignment and no rotational alignment. The lack of smoothing of features in this average particle suggests that the virus particles have preferred orientations in the paracrystalline array.

chosen that had the most visible information. The virus particles had so little contrast in most volume slices that extraction of particle densities and averaging did not yield any meaningful results. The 2D unstained image, Figure 4.8, in Section 4.4.1 showed that a signal of 600 electrons/pixel was enough to resolve details fairly well in an unstained sample. Using 1/6 of this dose per tilt angle was clearly not enough signal as the reconstruction software does not process low contrast images well and had difficulty with alignment so that the 7000 electrons/pixel signal for the entire volumetric reconstruction did not yield a tomogram with higher information.

This experiment is worth repeating using 600 electrons/pixel signal per tilt angle with drift correction applied since the imaging time would be 60 seconds per image. Conversely, using higher energy incident electrons, such as 300keV, would allow for much higher electron collection per frame allowing for shorter total imaging time and less need for drift correction. Thus this experiment is worth repeating on an intermediate energy TEM, equal or greater to 200keV, where the DQE would be much improved. Such an experiment may result in successful unstained tomographic reconstructions where staining artifacts will not limit the resolution. This first attempt, however, was a necessary step in determining the correct conditions to perform unstained tomography with the large format DDD.

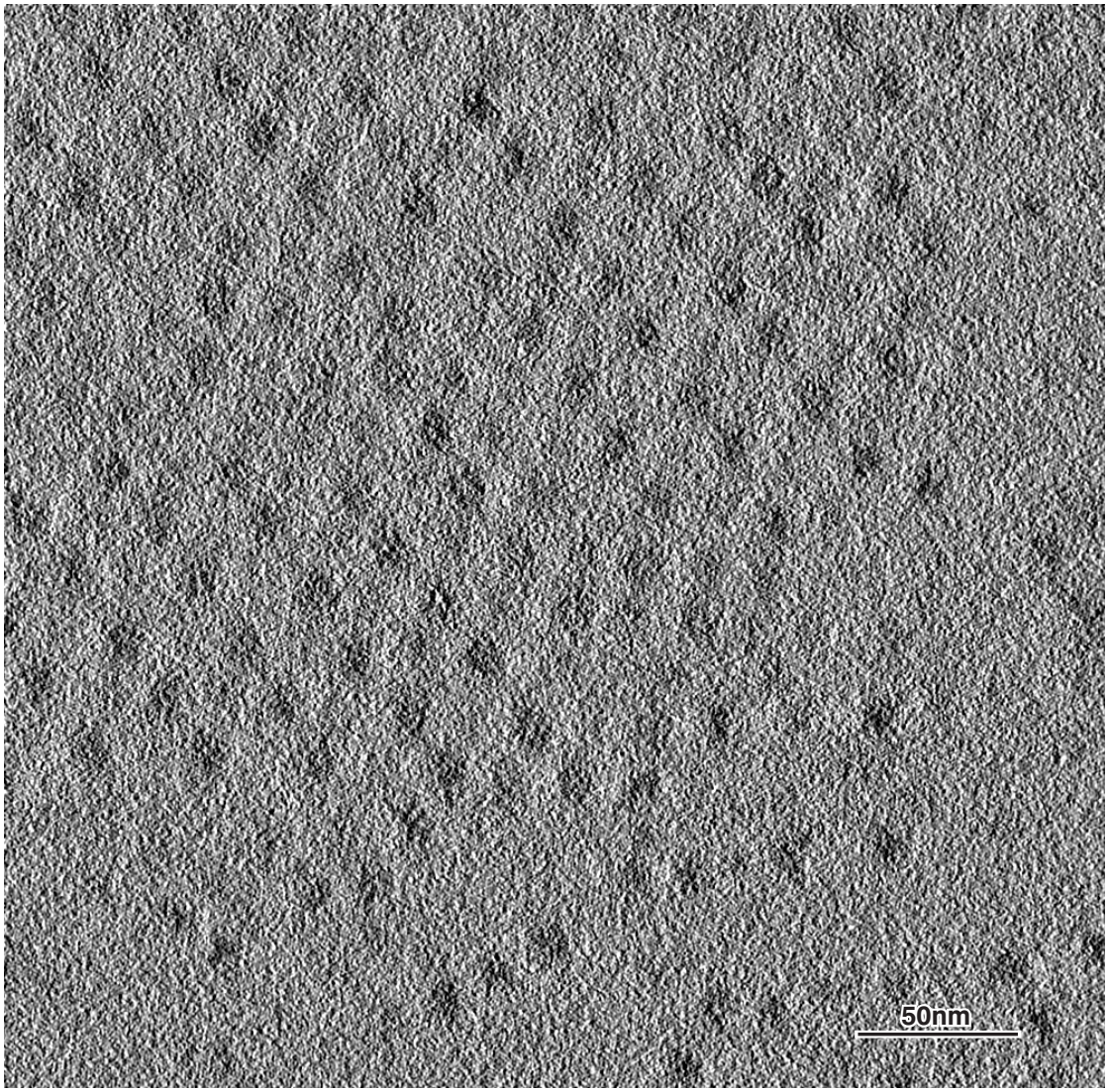

Figure 4.15: Volume reconstruction slice from unstained flock house virus array tomogram. Signal per tilt was approximately 100 electrons/pixel at a magnification of 14.5k. Greater signal per projection in the tilt series necessary for a quality reconstruction.

High resolution tomography with uranyl acetate and lead stain

The following tomography experiment was performed with a specimen that was lightly stained with uranyl acetate and Sato's lead. Prior to this point, high magnification imaging with the DDD was performed with limited success mainly because the small imaging area (5mm×5mm) of the detector that made focusing,

image alignment and correction for microscope stigmation difficult. However, after much practice manually using the DDD to acquire images, the imaging protocol was refined to allow for high quality imaging at a magnification of around 2.3$\mathring{A}$/ pixel. This single axis tilt series was acquired with a measured signal of about 100 electrons/pixel per projection and taken from $\pm 60^{\circ}$ in 2° increments. The exposure time for each tilt angle image was approximately 5 seconds and the magnification at the detector imaging plane was approximately 21750 (2.3$\mathring{A}$/pixel). A volume slice from the tomogram is shown in Figure 4.16. The size of the particles are on average 22nm. This would indicate that the uranyl acetate stained primarily the RNA cage while the Sato's lead stained some of the protein coat immediately surrounding the core. As was mentioned before, both uranyl acetate and lead are general stains and the light staining of a portion of the protein coat was an unexpected result. This illustrates how staining protocols are empirically driven as it is usually unknown how particular staining conditions will interact with the biological macromolecules to result in enhanced contrast of certain features.

This tomogram demonstrates the feasibility of successful high magnification imaging with the DDD. Because of the current physical location and setup of the FEI Spirit microscope, it is only certified to have good imaging quality around 2.5$\mathring{A}$/pixel due to external vibrations affecting the specimen and microscope. Attempting to demonstrate the ability to image at even higher resolutions with the large format DDD will require transfer to a TEM rated for higher resolution and is expected to happen in the near future.

4.4.3 Discussion of results

From the three single tilt tomograms presented in this section, there is compelling evidence that the large format DDD is useful for gathering meaningful information about biological specimen. The high sensitivity of the DDD made it possible to image the RNA cage of flock house virus in detail not observed previously. Furthermore, these tomograms present the current state of the development with the DDD for tomography. Of particular scientific significance is the highest resolution tilt series ever acquired with a DDD sensor that demonstrates the

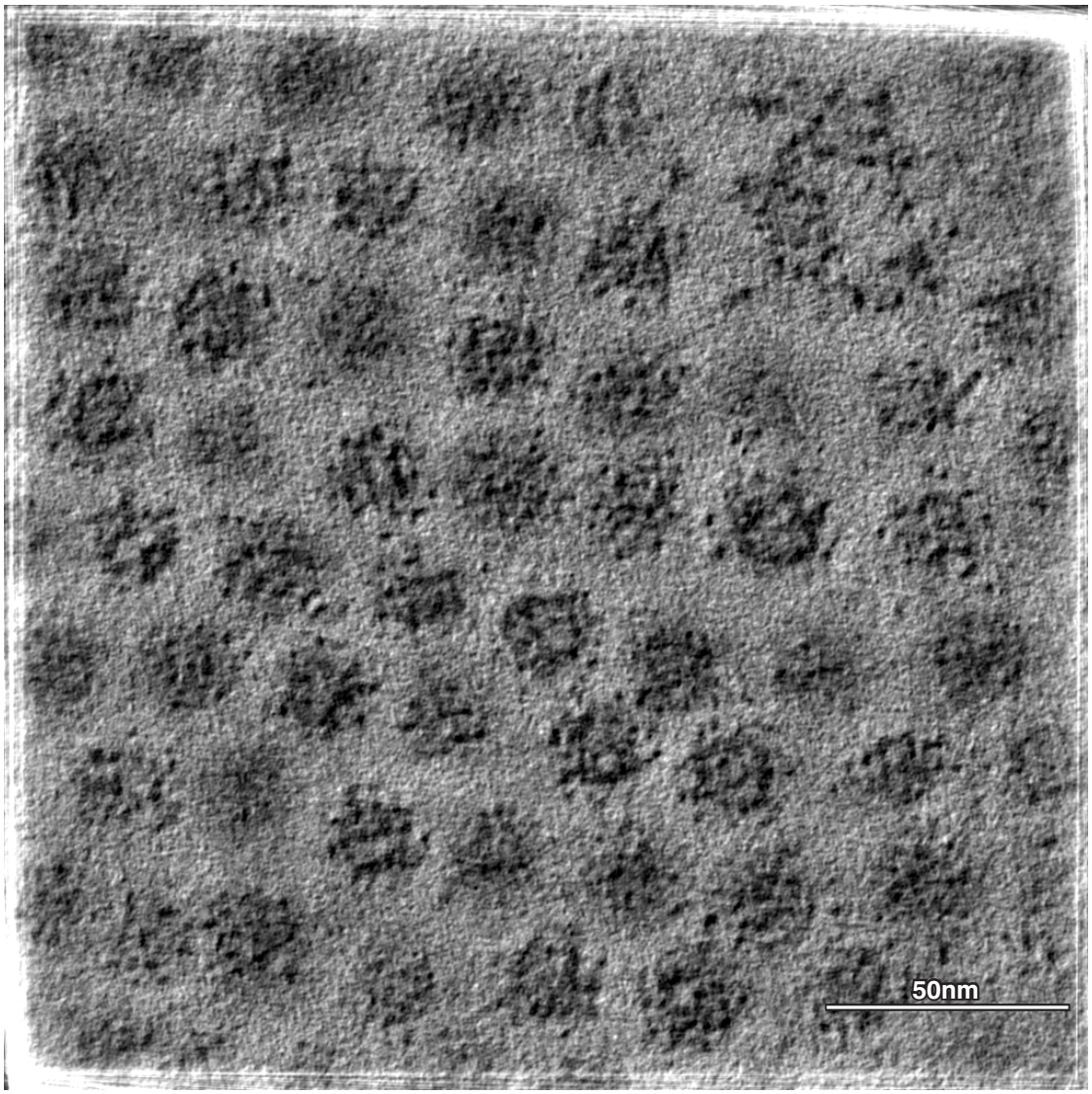

Figure 4.16: Slice from a tomogram taken with flock house virus stained with uranyl acetate and lead. Highest magnification study with DDD to date at approximately 22k magnification. Particles with this staining protocol are approximately 22nm, which is evidence for staining of RNA cage with some coat protein immediately adjacent.

feasibility of using the DDD for high magnification work.

Chapter 5

Conclusion and future directions

The large format DDD offers many advantages over current imaging systems and in this thesis we have only just begun to explore the many applications of this powerful detector. This thesis has presented a thorough characterization of the properties of the large format DDD that showed that this sensor has spatial resolution capabilities that outperform most commercial TEM CCD camera systems. The results presented in Chapter 4 conclusively show the usefulness of the large format DDD by exploring flock house virus in vivo at resolutions never achieved before. The performance of the large format DDD is even more impressive when considering that these experiments were performed on a 120keV TEM, a standard instrument in many facilities. Since the MTF and DQE measurements show that the DDD will achieve better resolution capabilities at higher energies, these studies at 120keV show a lower estimate for the image quality from this sensor. Installation of the large format DDD on intermediate electron voltage microscopes (200keV and above) is planned in the near future and there is much excitement over the even better image collection possible with higher energy electrons.

As development continues with the large format DDD, we expect to use even smaller gold fiducial markers than the 2nm colloidal gold used for the tomograms in this thesis. This could lead to pioneering new techniques for labeling biological macromolecules in the cell with nanogold (1.4nm) or undecagold (0.8nm) and imaging them with the DDD. Understanding biological processes requires defining the position of molecules in the cell. These molecules are too small to detect alone,

but labeling them with small gold and being able to detect them with the DDD may offer a tool as powerful as florescence labeling has been for light microscopy. For example, one could label flock house virus particles directly with small gold prior to high pressure freezing and then track viral entry into the cell.

Full automation with serialEM, a tomography acquisition software package, is close to completion. This will allow for high throughput tomography acquisition with the DDD. It will also enable acquisition of montage images, extending the imaging capabilities of the DDD to allow for large field of view images. One could envision using the high sensitivity of the DDD and the automation in many ways. Low resolution tomograms could be collected using a small portion of the total dose and tomographic reconstruction could be performed immediately. This lower resolution tomogram could help identify regions of interest to collect higher resolution tomography data with greater signal.

Planned future data collection with the large format DDD includes explorations of new biological systems and macromolecules as well as finishing up high resolution studies of flock house virus in vivo. Two flock house virus studies to be completed will be close examination of viral assembly in the mitochondria and the determination of the structure of the fibril bundles that extend from the infected mitochondria to the flock house paracrystalline arrays.

As new prototype DDD detectors become available, our ability to explore biological processes will only be limited by our imagination. As exciting as the results as the results of this thesis are, more potential still lies ahead with future detector design. Faster readout is already available in the next generation prototype which will allow for better utilization of the features of the unique features of the DDD. This thesis has described the use of the DDD sensor as an integrating detector. Faster readout will improve post processing image drift correction and will help with low dose image acquisition as the time it takes to read out the first frame decreases. Yet, even more fundamentally important to improvement in MTF, faster readout will enable the use of the DDD as an electron counting device [56]. This would allow for improvement in spatial resolution to sub pixel (less than 5μm) accuracy.

Bibliography

[1] European Standard EN 62220-1-2:2007. Medical electrical equipment Characteristics of digital X-ray imaging devices, 2007.

[2] RS Aikens, DA Agard, and JW Sedat. Solid-state imagers for microscopy. *Methods Cell Biol*, 29:291–313, 1989.

[3] B. Bailey, DA Agard, JW Sedat, M. Barfels, H. Chao, and PE Mooney. Performance Evaluation of a Transmission Scintillator-Based Lens-Coupled 4K CCD Camera for Use in Low-Dose Electron Cryo-Tomography. *Microscopy and Microanalysis*, 10(S02):1204–1205, 2004.

[4] M. Battaglia, D. Contarato, P. Denes, D. Doering, P. Giubilato, T.S. Kim, S. Mattiazzo, V. Radmilovic, and S. Zalusky. A rad-hard CMOS active pixel sensor for electron microscopy. *Nuclear Inst. and Methods in Physics Research, A*, 598(2):642–649, 2009.

[5] J. Beutel, H.L. Kundel, and R.L. Van Matter. *Handbook of medical imaging. Vol. 1, Physics and psychophysics*. SPIE Press, 2000.

[6] H. Bichsel. Inelastic Electronic Collision Cross Sections for Monte Carlo Calculations. *Nuclear Instruments & Methods in Physics Research Section B, Beam Interactions with Materials and Atoms*, 52:136–139, 1990.

[7] JC Bouwer, ST Peltier, L. Jin, K. Khodjasaryan, S. Geist, NH Xuong, and MH Ellisman. Analysis of the Performance of an 8k x 8k Lens Coupled Detector for Wide-field, High-resolution Transmission Electron Microscopy (TEM). *Microscopy and Microanalysis*, 11(S02):62–63, 2005.

[8] W. S. Boyle and G. E. Smith. Charge-Coupled Semiconductor Devices. *Bell System Tech. J.*, 49:587–593, 1970.

[9] J.J. Bozzola and L.D. Russell. *Electron Microscopy: Principles and Techniques for Biologists*. Jones & Bartlett Publishers, 1999.

[10] S. Brandt, J. Heikkonen, and P. Engelhardt. Automatic Alignment of Transmission Electron Microscope Tilt Series without Fiducial Markers. *Journal of Structural Biology*, 136(3):201–213, 2001.

[11] R. Brun, F. Rademakers, et al. ROOT-An Object Oriented Data Analysis Framework. In *Proceedings AIHENP*, volume 96, pages 81–86, 1997.

[12] D. Castańo-Díez, A. Al-Amoudi, A.M. Glynn, A. Seybert, and A.S. Frangakis. Fiducial-less alignment of cryo-sections. *Journal of Structural Biology*, 159(3):413–423, 2007.

[13] United Technologies Microelectronics Center. Semicustom/Military Standard Radiation-Hardened CMOS Technical Description, 1992.

[14] JN Chapman, AJ Craven, and CP Scott. Electron detection in the analytical electron microscope. *Ultramicroscopy*, 28:108–117, 1989.

[15] R Holland Cheng, Vijay S Reddy, Norman H Olson, Andrew J Fisher, Timothy S Baker, and John E Johnson. Functional implications of quasi-equivalence in a t=3 icosahedral animal virus established by cryo-electron microscopy and x-ray crystallography. *Structure*, 2(4):271 – 282, 1994.

[16] Conduant Corporation. `http://www.conduant.com`.

[17] RA Crowther, DJ DeRosier, and A. Klug. The Reconstruction of a Three-Dimensional Structure from Projections and its Application to Electron Microscopy. *Proceedings of the Royal Society of London. Series A, Mathematical and Physical Sciences (1934-1990)*, 317(1530):319–340, 1970.

[18] Z. Czyżewski, D.O.N. MacCallum, A. Romig, and D.C. Joy. Calculations of Mott scattering cross section. *Journal of Applied Physics*, 68:3066, 1990.

[19] I. Daberkow, K.H. Herrmann, L. Liu, and Rau WD. Performance of electron image converters with YAG single-crystal screen and CCD sensor. *Ultramicroscopy*, 38(3-4):215–223, 1991.

[20] P. Denes, J.M. Bussat, Z. Lee, and V. Radmillovic. Active Pixel Sensors for electron microscopy. *Nuclear Inst. and Methods in Physics Research, A*, 579(2):891–894, 2007.

[21] G. Deptuch, A. Besson, P. Rehak, M. Szelezniak, J. Wall, M. Winter, and Y. Zhu. Direct electron imaging in electron microscopy with monolithic active pixel sensors. *Ultramicroscopy*, 107(8):674–684, 2007.

[22] B. Dierickx, G. Meynants, and D. Scheffer. Near-100% fill factor standard CMOS active pixel. In *Proc. 1997 IEEE Workshop on Charge-Coupled Devices and Advanced Image Sensors*, 1997.

[23] KH Downing and FM Hendrickson. Performance of a 2 k CCD camera designed for electron crystallography at 400 kV. *Ultramicroscopy*, 75(4):215–233, 1999.

[24] GY Fan and MH Ellisman. Digital imaging in transmission electron microscopy. *Journal of Microscopy*, 200(1):1–13, 2000.

[25] GY Fan, S. Peltier, S. Lamont, DG Dunkelberger, BE Burke, and MH Ellisman. Multiport-readout frame-transfer 5 megapixel CCD imaging system for TEM applications. *Ultramicroscopy*, 84(1-2):75–84, 2000.

[26] AR Faruqi and HN Andrews. Cooled CCD camera with tapered fibre optics for electron microscopy. *Nuclear Instruments and Methods in Physics Research Section A*, 392(1-3), 1997.

[27] AR Faruqi and R. Henderson. Electronic detectors for electron microscopy. *Current Opinion in Structural Biology*, 17(5):549–555, 2007.

[28] J. Frank. *Electron Tomography: Three-Dimensional Imaging With the Transmission Electron Microscope*. Springer, 1992.

[29] R. Henderson, D. Cattermole, G. McMullan, S. Scotcher, M. Fordham, W.B. Amos, and A.R. Faruqi. Digitisation of electron microscope films: Six useful tests applied to three film scanners. *Ultramicroscopy*, 107(2-3):73 – 80, 2007.

[30] Imaging Products Operations Hewlett-Packard Components Group. Noise Sources in CMOS Image Sensors, 1998.

[31] Gatan Inc. `http://www.gatan.com`.

[32] S. Isoda, K. Saitoh, S. Moriguchi, and T. Kobayashi. Utility test of imaging plate as a high-resolution image-recording material for radiation-sensitive specimens. *Ultramicroscopy*, 35(3-4):329 – 338, 1991.

[33] L. Jin, A.C. Milazzo, S. Kleinfelder, S. Li, P. Leblanc, F. Duttweiler, J.C. Bouwer, S.T. Peltier, M. Ellisman, and N.H. Xuong. The intermediate size direct detection detector for electron microscopy. In *Proceedings of SPIE*, volume 6501, page 65010A. SPIE, 2007.

[34] L. Jin, A.C. Milazzo, S. Kleinfelder, S. Li, P. Leblanc, F. Duttweiler, J.C. Bouwer, S.T. Peltier, M.H. Ellisman, and N.H. Xuong. Applications of direct detection device in transmission electron microscopy. *Journal of Structural Biology*, 161(3):352–358, 2008.

[35] J.E. Johnson. Multi-disciplinary studies of viruses: The role of structure in shaping the questions and answers. *Journal of Structural Biology*, 2008.

[36] S. Kleinfelder, H. Bichsel, F. Bieser, H.S. Matis, G. Rai, F. Retiere, H. Wieman, and E. Yamamoto. Integrated X-ray and charged particle active pixel CMOS sensor arrays using an epitaxial silicon-sensitive region. In *Proceedings of SPIE*, volume 4784, pages 208–217, 2002.

[37] S. Kleinfelder, F. Bieser, Yandong Chen, R. Gareus, H.S. Matis, M. Oldenburg, F. Retierc, H.G. Ritter, H.H. Wieman, and E. Yamamoto. Novel integrated cmos pixel structures for vertex detectors. *Nuclear Science Symposium Conference Record, 2003 IEEE*, 1:335–339 Vol.1, Oct. 2003.

[38] S. Kleinfelder, S. Li, and Y. Chen. Optimization of monolithic charged-particle sensor arrays. *Nuclear Inst. and Methods in Physics Research, A*, 579(2):695–700, 2007.

[39] L. Landau. On the energy loss of fast particles by ionization. *J. Phys. U.S.S.R*, 8:201, 1944.

[40] J. Lanman, J. Crum, T.J. Deerinck, G.M. Gaietta, A. Schneemann, G.E. Sosinsky, M.H. Ellisman, and J.E. Johnson. Visualizing flock house virus infection in Drosophila cells with correlated fluorescence and electron microscopy. *Journal of Structural Biology*, 161(3):439–446, 2008.

[41] A. Lawrence, J.C. Bouwer, G. Perkins, and M.H. Ellisman. Transform-based backprojection for volume reconstruction of large format electron microscope tilt series. *Journal of Structural Biology*, 154(2):144–167, 2006.

[42] Albert Lawrence, Sébastien Phan, and Rajvikram Singh. Parallel Processing and Large-Field Electron Microscope Tomography. In *Proceedings of CSIE09*. CSIE, 2009 (in press).

[43] Shengdong Li. Modeling, Design, and Analysis of Monolithic Charged particle Image Sensors. Ph.D thesis, Univ. of California, Irvine, 2007.

[44] Vladan Lučić, Friedrich Förster, and Wolfgang Baumeister. Structural studies by electron tomography: From cells to molecules. *Annual Review of Biochemistry*, 74(1):833–865, 2005. PMID: 15952904.

[45] Steven J. Ludtke, Philip R. Baldwin, and Wah Chiu. Eman: Semiautomated software for high-resolution single-particle reconstructions. *Journal of Structural Biology*, 128(1):82 – 97, 1999.

[46] D.N. Mastronarde. Dual-Axis Tomography: An Approach with Alignment Methods That Preserve Resolution. *Journal of Structural Biology*, 120(3):343–352, 1997.

[47] D.N. Mastronarde. Fiducial Marker and Hybrid Alignment Methods for Single-and Double-axis Tomography. *Electron Tomography: Methods for Three-Dimensional Visualization of Structures in the Cell*, pages 163–85, 2006.

[48] BF McEwen, KH Downing, and RM Glaeser. The relevance of dose-fractionation in tomography of radiation-sensitive specimens. *Ultramicroscopy*, 60(3):357–373, 1995.

[49] J.R. McIntosh. Electron Microscopy of Cells A New Beginning for a New Century. *The Journal of Cell Biology*, 153(6):25–32, 2001.

[50] G. McMullan and AR Faruqi. Electron microscope imaging of single particles using the Medipix2 detector. *Nuclear Inst. and Methods in Physics Research, A*, 591(1):129–133, 2008.

[51] C. Messaoudi, N.G. de Loubresse, T. Boudier, P. Dupuis-Williams, and S. Marco. Multiple-axis tomography: applications to basal bodies from Paramecium tetraurelia. *Biology of the Cell*, 98:415–425, 2006.

[52] R.R. Meyer and A.I. Kirkland. Characterisation of the signal and noise transfer of CCD cameras for electron detection. *Microscopy Research and Technique*, 49(3):269–280, 2000.

[53] G. Meynants, B. Dierickx, and D. Scheffer. CMOS active pixel image sensor with CCD performance. In *Proceedings of SPIE*, volume 3410, page 68. SPIE, 1998.

[54] A.C. Milazzo, P. Leblanc, F. Duttweiler, L. Jin, J.C. Bouwer, S. Peltier, M. Ellisman, F. Bieser, H.S. Matis, H. Wieman, et al. Active pixel sensor array as a detector for electron microscopy. *Ultramicroscopy*, 104(2):152–159, 2005.

[55] G Moldovan, X Li, and A Kirkland. Can direct electron detectors outperform phosphor-CCD systems for TEM? *Journal of Physics: Conference Series*, 126:012089 (4pp), 2008.

[56] G. Moldovan, X. Li, P. Wilshaw, and AI Kirkland. Counting Electrons in Transmission Electron Microscopes. *Microscopy and Microanalysis*, 14(S2):912–913, 2008.

[57] D.R. Musser, G.J. Derge, and A. Saini. *STL tutorial and reference guide: C++ programming with the standard template library*. Addison-Wesley Longman Publishing Co., Inc. Boston, MA, USA, 2001.

[58] Sébastien Phan, James Bouwer, Jason Lanman, Masako Terada, and Albert Lawrence. Non-Linear Bundle Adjustment for Electron Tomography. In *Proceedings of CSIE09*. CSIE, 2009 (in press).

[59] Sébastien Phan and Albert Lawrence. Tomography of Large Format Electron Microscope Tilt Series: Image Alignment and Volume Reconstruction. *Image and Signal Processing, 2008. CISP '08. Congress on*, 2:176–182, May 2008.

[60] PTE Roberts, JN Chapman, and AM MacLeod. A CCD-based image recording system for the CTEM. *Ultramicroscopy*, 8:385–396, 1982.

[61] H H Rose. Optics of high-performance electron microscopes. *Science and Technology of Advanced Materials*, 9(1):014107 (30pp), 2008.

[62] T. SATO. A Modified Method for Lead Staining of Thin Sections, 1968.

[63] Michael F. Schmid and Christopher R. Booth. Methods for aligning and for averaging 3d volumes with missing data. *Journal of Structural Biology*, 161(3):243 – 248, 2008. The 4th International Conference on Electron Tomography, The 4th International Conference on Electron Tomography.

[64] Anette Schneemann. The structural and functional role of RNA in icosahedral virus assembly. *Annual Review of Microbiology*, 60(1):51–67, 2006. PMID: 16704342.

[65] PD Scotti, S. Dearing, and DW Mossop. Flock house virus: A Nodavirus isolated from Costelytra zealandica (White)(Coleoptera: Scarabaeida). *Archives of Virology*, 75(3):181–189, 1983.

[66] The MOSIS Service. `http://www.mosis.com`.

[67] JB Sheffield. ImageJ, A useful tool for biological image processing and analysis. *Microscopy and Microanalysis*, 13(SO2):200–201, 2007.

[68] B. Stroustrup. *The design and evolution of C++*. ACM Press/Addison-Wesley Publishing Co. New York, NY, USA, 1995.

[69] S. Subramaniam, A. Bartesaghi, J. Liu, A.E. Bennett, and R. Sougrat. Electron tomography of viruses. *Current Opinion in Structural Biology*, 17(5):596–602, 2007.

[70] A. Todd-Pokropek. Theory of tomographic reconstruction. *Tomographic Methods in Nuclear Medicine: Physical Principles, Instruments, and Clinical Applications*, page 2, 1989.

[71] R. Turchetta, JD Berst, B. Casadei, G. Claus, C. Colledani, W. Dulinski, Y. Hu, D. Husson, JP Le Normand, JL Riester, et al. A monolithic active pixel sensor for charged particle tracking and imaging using standard VLSI CMOS technology. *Nuclear Inst. and Methods in Physics Research, A*, 458(3):677–689, 2001.

[72] Tietz Video and Image Processing System GmbH. `http://www.tvips.com`.

[73] N.H. Xuong, L. Jin, S. Kleinfelder, S. Li, P. Leblanc, F. Duttweiler, J.C. Bouwer, S.T. Peltier, A.C. Milazzo, and M. Ellisman. Future Directions for Camera Systems in Electron Microscopy. *Cellular Electron Microscopy*, page 721, 2007.

[74] N.H. Xuong, A.C. Milazzo, P. LeBlanc, F. Duttweiler, J. Bouwer, S. Peltier, M. Ellisman, P. Denes, F. Bieser, H.S. Matis, et al. First use of a high-sensitivity active pixel sensor array as a detector for electron microscopy. In *Proceedings of SPIE*, volume 5301, page 242. SPIE, 2004.

[75] JM Zuo. Electron detection characteristics of a slow-scan CCD camera, imaging plates and film, and electron image restoration. *Microscopy Research and Technique*, 49(3):245–268, 2000.

[76] JM Zuo, MR McCartney, and JCH Spence. Performance of imaging plates for electron recording. *Ultramicroscopy*, 66(1-2):35–47, 1996.